Andrea Kraxner

Optimization of the parameters of CMOS-integrated photodiodes

MASTER THESIS

For obtaining the academic degree
Diplom-Ingenieurin

Master Programme of
Advanced Materials Science

Graz University of Technology

Supervisor:

Ao.Univ.-Prof. Dipl.-Ing. Dr.techn. Egbert Zojer

Institute of Solid State Physics

Graz, January 2013

ACKNOWLEDGEMENTS

I want to thank my supervisor from TU Graz Egbert Zojer for his support and including me in his group. Our group meetings gave me the possibility to learn about other very interesting fields of physics.

Many thanks also to Ewald Wachmann my supervisor from ams AG who gave me the possibility to do my master thesis in cooperation with this great company. I also want to thank Rainer Minixhofer who answered every upcoming question and gave me the possibility to achieve also a more theoretical point of view of my work. Special thanks also to all my colleagues at ams, especially Ingrid Jonak-Auer and Jordi Teva, who always supported me and who were a big help during my time at ams.

I want to say special thanks to my parents and my whole family, who made my studies possible. They always supported me emotional as well as financial and for that I am very thankful. I also want to thank Christoph for his endless patience and continuous encouragement. He remained calm when I needed it and always pushed me in the right moments.

ABSTRACT

Because of high noise and low fill factors, CMOS (Complementary Metal Oxide Semiconductor) photodetector technology was not competitive to CCDs (Charge Coupled Devices) in the early 60ies. This situation has changed since the early 90ies due to a lot of improvements, especially the possibility of monolithically integration. Nowadays CMOS photodetectors are not only competitive to CCD sensors but also offer the possibility for new fields of application. [1] In order to further enhance the performance of CMOS sensors, it is crucial to improve the light sensing element, the photodiode, optimizing its parameters achieving e.g. wavelength sensitivity in a specific region, minimizing dark currents, or reducing crosstalk. [2] These aspects are the topic of this thesis.

Its first part focuses on the optimization of the responsivity and the dark current behavior by design variations. This is done by comparing different photodiode structures which are provided in a standard high voltage CMOS process. It is shown how the wavelength sensitivity can be tuned efficiently by varying well combinations regarding doping concentration, junction depth and through the use of multiple junctions that are differently shorted. Additionally, the various structures were also characterized with respect to their dark currents. To gain an even better understanding of the investigated structures, photodiode parameters as well as spectral responsivities are calculated with an analytical model that are benchmarked against measured data.

Furthermore, strategies for reducing crosstalk are presented, where the focus lies on guard-ring structures that are introduced in the photodiode design. The goal of these studies is to fully understand the characteristics of various guard-ring structures and to find a guard-ring design that minimizes crosstalk and at the same time is characterized by a low dark current.

KURZFASSUNG

Aufgrund zu hohen Rauschens und zu kleiner Füllfaktoren waren CMOS (Complementary Metal Oxide Semiconductor) Sensoren Anfang der 60iger im Vergleich zu CCDs (Charge Coupled Devices) nicht konkurrenzfähig. Seit den frühen 90igern wurden bei der Entwicklung von CMOS Sensoren allerdings enorme Fortschritte erzielt. Dies betrifft insbesondere die Möglichkeit monolithischer Integration, was das Potential von CMOS Sensoren enorm steigerte Heute sind CMOS Sensoren nicht nur im Vergleich zu CCDs konkurrenzfähig, sie eröffnen auch viele neue Anwendungsgebiete. [1]

Um die Leistungsfähigkeit von CMOS Sensoren weiter zu verbessern, ist es wichtig insbesondere die Licht detektierenden Elemente weiterzuentwickeln. In der vorliegenden Arbeit sind das Photodioden. Dementsprechend liegt der Fokus der vorgestellten Untersuchungen auf Designstrategien um Empfindlichkeit bei bestimmten Wellenlängen zu erreichen, sowie Dunkelstrom und Crosstalk (i.e., ein „Übersprechen zwischen Benachbarten Photodioden) zu minimieren. [2]

Im ersten Teil der vorliegenden Masterarbeit wird präsentiert, wie Strukturen, die in einem Standard Hochvolt-Prozesse vorkommen, als Photodioden verwendet werden können. Es wird gezeigt, wie die spektrale Empfindlichkeit durch Variationen im Photodiodendesign für verschiedene Wellenlängenbereiche optimiert werden kann. Letzteres wird durch unterschiedliche Dotierkoknzentrationen, unterschiedlichen Übergangspositionen zwischen den p- und n-halbleitenden Bereichen und durch Kurzschließen bestimmter Struktrubereiche erreicht. Um den Einfluss der Strukturvariationen auf den Dunkelstrom zu evaluieren wurde auch dieser gemessen und ausgewertet. Um ein noch tieferes Verständnis über die relevanten Prozesse zu erzielen wurden ergänzend Simulationen mit analytischen Modellen durchgeführt.

Im zweiten Teil der Arbeit wird auf die Notwendigkeit der Minimierung von Crosstalk in Sensorarrays eingegangen. Um dies zu erreichen, werden so-genannte Guard-Ring Strukturen in das Bauelementedesign integriert. Das Ziel dieser Untersuchung ist die Funktionsweise dieser Guard Ring Strukturen besser zu verstehen und das Crosstalk verhalten zu verbessern. Um gleichzeitig auch einen niedrigen Dunkelstrom zu

gewährleisten, werden verschiedene Guard-Ring Strukturen in Bezug auf Crosstalk und Dunkelstrom miteinander verglichen.

CONTENTS

1 Introduction **1**

2 Photodiode theory **3**

2.1 P-n junctions 3

2.1.1 Electrostatic analysis of a p-n diode 3

2.1.2 Current-Voltage characteristic of a p-n diode 10

2.2 Photodiodes 14

2.2.1 Optical absorption and carrier generation through photons 14

2.2.2 Types of photodiodes 20

2.2.3 Photodiode parameters 24

3 CMOS Sensors **28**

3.1 Historical background 28

3.2 Advantages and disadvantages 28

3.3 Basic principles and operation of CMOS sensors 29

3.3.1 Passive Pixel Sensor (PPS) 30

3.3.2 Active Pixel Sensor (APS) 31

3.3.3 Active Pixel Sensor using a pinned photodiode 31

3.4 CMOS sensor structure 33

3.5 Sources of noise 34

4 Measurement setup **35**

4.1 Dark current measurement 35

4.2 Responsivity measurement 36

4.3 Crosstalk measurement 38

5 Evaluation of different well combinations cccurring in a high voltage process **39**

5.1 Structures 39

5.1.1 n-well in p-substrate/p-well structures 40

5.1.2 p-well in n-well in p-substrate structures 42

5.2 Spectral responsivity 46

5.2.1 n-well in p-substrate structures 46

5.2.2 p-well in n-well in p-substrate structures 53

5.3 Analytical calculations 62

5.3.1 Fit of doping profile 62

5.3.2 Calculation of parameters 69

5.3.3 Calculated responsivty behavior...73

5.4 Dark current 76

5.4.1 n-well in p-substrate/p-well Structures 76

5.4.2 p-well in n-well in p-substrate structures 80

6 Dark current and crosstalk performance 88

6.1 Photodiode structure 88

6.2 Crosstalk theory 89

6.3 Working principle of a guard ring 90

6.4 Dark current 91

6.5 Area-perimeter model 93

6.5.1 Conclusion of area to perimeter model..99

6.6 Temperature dependence of the dark current...99

6.7 Evaluation of different guard ring designs 101

6.7.1 Dark current 102

6.7.2 Crosstalk 104

6.8 Guard-less design 108

6.9 Conclusion to guard ring..114

7 Conclusion 115

8 List of Figures 117

9 List of Tables..124

10 Bibliography..125

1 INTRODUCTION

Optoelectronic devices are used by almost everyone in the industrialized world in daily life. Especially the introduction of cameras in every cell phone and other electronic devices makes cheap production of imagers and detectors necessary. The use of CMOS (Complementary Metal Oxide Semiconductor) sensors provides a cheap alternative to CCD (Charge Coupled Device) image sensors. [1] In addition to the low cost imaging market, the possibility of monolithic integration and their low power consumption makes CMOS sensors very attractive for a big range of applications also in the high performance application region. [2] For this and many more reasons the interest to further improve CMOS sensors is high.

One of the key elements, defining the performance of a CMOS sensor, is the light sensing element. This thesis concentrates on the optimization of photodiodes. In order to increase the performance and tune the sensors for certain applications the device properties have to be optimized. The parameters most critical for the performance are the spectral responsivity, the dark current and the crosstalk. Both parameters depend on the used semiconductor material but also on the design of the photodiode. [3] The goal of this thesis is to better understand the behavior of different design variations of photodiodes to be able to optimize them for different applications.

In this context it should be mentioned that the impact of the read-out circuit on the overall performance is not evaluated here.

In the first part of this thesis, in section 2 and section 3, a short introduction to the theory of photodiodes and CMOS sensors is given. This section should help to better understand the effects investigated in the experimental part. After this a short description of the measurement setup is included in section 4.

In the main part of the thesis the experimental investigations are discussed. They are separated into two sections dealing with different important aspects of a sensor array.

Section 5, focuses on the design of the photodiode itself. P-n junctions occurring in standard CMOS processes can be used as photodiodes when directly illuminated. Possibilities of how to use some of these standard structures were already shown in [4] and [5]. In this thesis a large number of different well combinations occurring in a high voltage process are shown. These wells can also be used as photodiodes allowing the realization of a lot of different photodiode structures suitable for different applications. The difference of the designs lies in different doping and different depths of the wells. To characterize the different structures optical and electrical measurements were performed. The main parameters of interest are the spectral responsivity and the dark current. It is shown that by varying the well combinations forming the photodiode the spectral responsivity can be changed significantly when suppressing the diffusion component to the photocurrent. In addition to the measurements, also analytical calculations are done to provide further insight into the behavior of the different structures.

While in the first part of the experimental section the photodiode design itself is in the focus of interest, in section 6 the “interaction” between neighboring pixels in an array is of interest. To ensure high quality of the final product, electrical isolation between single pixels is important. [6] To achieve that so called guard ring structures are introduced to the pixel design in analogy to the discussion in [7]. The operating principle of such guard rings is investigated and different design possibilities are compared with each other. In general, one can see that by introducing a guard ring structure the crosstalk behavior is improved at the expense of the dark current behavior. The goal is to find a guard ring structure minimizing crosstalk and at the same time producing a low dark current.

This thesis is done in cooperation with ams AG and the production and evaluation of the used devices were done at the company.

2 PHOTODIODE THEORY

To have a better understanding of the experimental part of the thesis it is important to know about the theory behind the work. Thus, in the following the function of a photodiode and its most important parameters will be summarized. Furthermore, different types of photodiodes for different applications will be briefly discussed. The contents of this section are based on the work from Sze [8], Zeghbrock [9] and Thuselt [10].

2.1 P-n junctions

2.1.1 Electrostatic analysis of a p-n diode

For a photodiode it is not enough to have a homogenous semiconductor. The formation of a p-n junction is necessary. In general a p-n junction consists of a combination of p-doped and n-doped semiconductors. This work concentrates on n- and p-doped silicon, thus all the discussions will focus on this semiconductor material.

When combining a p- and an n-doped semiconductor a diffusion current of holes to the n-side and electrons to the p-side occurs, this is driven by the differences in concentration in these charge regions. A so-called space charge region is formed that is depleted of mobile carriers. As shown in Figure 1, on the n-side a positively charged region and on the p-side a negatively charged region is formed. Outside the depletion region, the n- and p-regions are charge neutral. [9] The width of the depletion region is a very important parameter in this work. Because of this the theory of the p-n junction is discussed more detailed.

In the following discussions the "full-depletion approximation" is used. This approximation states that on the one hand there are well defined edges for the depletion region around the metallurgical junction and on the other hand an abrupt p-n junction is given. [9] Furthermore, uniformly doping is assumed. In the practical part of this work it will be shown that analogous analytical expressions can be achieved using the real doping profiles.

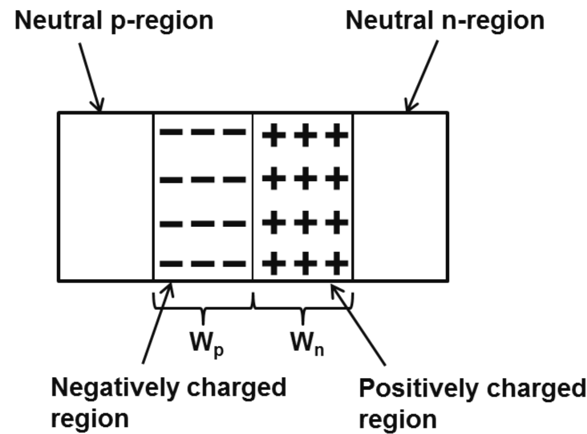

Figure 1: Formation of depletion region with a negative region on p-side and a positive region on n-side [11]

The net charge in the depletion region, results in an electric field causing a drift current, which opposes the diffusion current. At thermodynamic equilibrium, with no applied voltage the drift current and the diffusion current are the same and no net current is flowing. The different chemical potentials of the two semiconductor types result in an internal potential, called the built-in potential. In thermodynamic equilibrium the built-in potential is the potential across the depletion layer. The built-in potential equals the difference of the energies of the Fermi level on the p- and n-side, relative to the band edges, divided by the elementary charge, which for the above described situation leads to the following expression: [9]

$$V_{bi} = V_{th} ln \frac{N_d * N_a}{n_i^2} \tag{2.1}$$

In Figure 2 the space charge distribution, the electric field distribution and the potential across the depletion layer are shown.

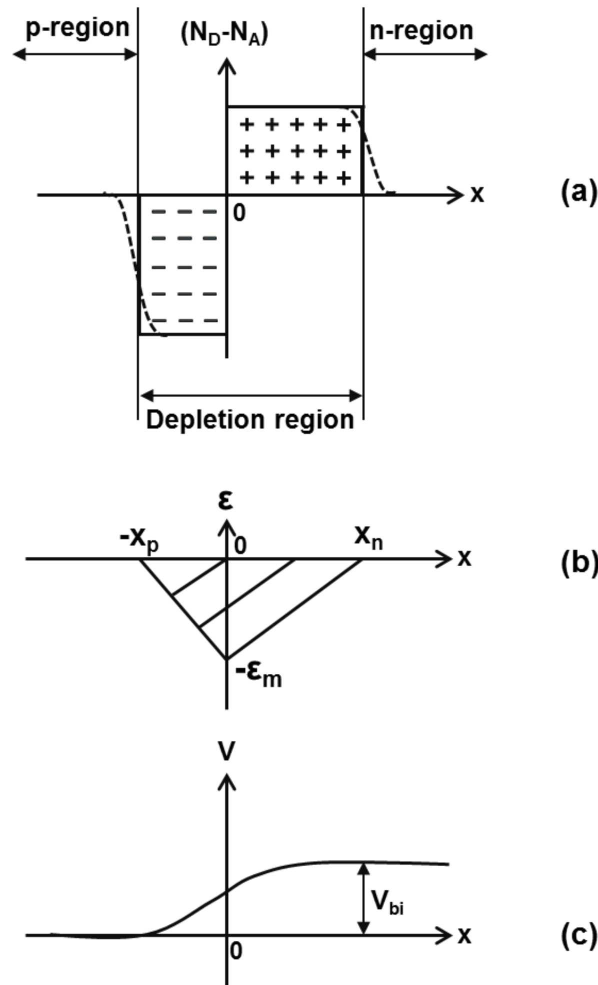

Figure 2: Abrupt p-n junction in thermal equilibrium: (a) space charge distribution, (b) electric field distribution, (c) potential variation with distance (V_{bi} is the built-in potential) [8]

To describe the properties of a p-n junction, like shown in Figure 2, it is useful to first describe its electrostatic properties. Here the Poisson equation is used as a starting point. (The following steps follow the discussion in [9])

$$\frac{d^2\Phi}{dx^2} = -\frac{\partial \mathcal{E}}{\partial x} = -\frac{\rho}{\varepsilon_r \varepsilon_0} = -\frac{q}{\varepsilon_r \varepsilon_0}(p - n + N_D^+ - N_A^-) \tag{2.2}$$

In (2.2) the charge density ρ is expressed through the electron and hole density and the densities of ionized dopants. The Poisson equation gives the relation between the potential, the electric field and the charge density. From these parameters the depletion layer width W, can be calculated. It is given, by the sum of the depletion layer width in the p-region w_p and the depletion layer width in the n-region w_n.

$$W = w_p + w_n \tag{2.3}$$

Using the full depletion approximation it is easy to find the charge density profile.

$$\begin{aligned}
&\rho(x) = 0 && -x_p \leq x \\
&\rho(x) = -qN_A && -x_p \leq x < 0 \\
&\rho(x) = qN_D && 0 < x \leq x_n \\
&\rho(x) = 0 && x \geq x_n
\end{aligned} \tag{2.4}$$

Now N_A and N_D are the dopant densities because all dopants are ionized.

As already shown in (2.2) the electric field is calculated from the charge density.

$$\frac{\partial \mathcal{E}(x)}{\partial x} = \frac{\rho(x)}{\varepsilon_r \varepsilon_0} \tag{2.5}$$

Outside the depletion region the electric field has to be zero because the free carriers would be forced to move, thus eliminating any electric field. This fact is used as boundary condition to solve equation (2.5).

Using (2.4) and (2.5) and the boundary condition mentioned above the electric field can be calculated.

$$\mathcal{E}(x) = 0 \qquad -x_p \leq x \qquad \text{(a)}$$

$$\mathcal{E}(x) = \frac{-qN_A(x + x_p)}{\varepsilon_r \varepsilon_0} \qquad -x_p \leq x < 0 \qquad \text{(b)}$$

$$\mathcal{E}(x) = \frac{qN_D(x + x_n)}{\varepsilon_r \varepsilon_0} \qquad 0 < x \leq x_n \qquad \text{(c)} \qquad (2.6)$$

$$\mathcal{E}(x) = 0 \qquad x \geq x_n \qquad \text{(d)}$$

As it can be seen in Figure 2 as well as from (2.6) the electric field reaches its maximum at x=0; i.e., at the interface between the p- and n-doped materials.

The value of $\mathcal{E}(0)$ can be calculated either using (2.6) (b) or (c), which yields

$$\mathcal{E}(0) = \frac{-qN_D x_n}{\varepsilon_r \varepsilon_0} = \frac{-qN_A x_p}{\varepsilon_r \varepsilon_0} \qquad (2.7)$$

From that a relationship between x_n and x_p can be determined.

$$N_A x_p = N_D x_n \qquad (2.8)$$

This expression shows that the total positive charge is the same as the total negative charge, which also follows from charge conservation.

By integrating the electric field, the potential across the depletion region can be calculated.

$$\frac{\mathrm{d}\Phi(\mathrm{x})}{\mathrm{dx}} = -\mathcal{E}(\mathrm{x}) \qquad (2.9)$$

The total potential that drops across the junction is called the built-in potential and was already mentioned earlier in this section. Another way to write it is, as the sum of the potential that drops between $-x_p$ and 0 and between 0 and x_n. This amounts to

$$V_{bi} = \frac{qN_D x_n^2}{2\varepsilon_r\varepsilon_0} + \frac{qN_A x_p^2}{2\varepsilon_r\varepsilon_0} \tag{2.10}$$

Based on the above considerations, the depletion layer width can be calculated. From combining (2.3) and (2.8) one gets

$$\begin{aligned} x_n &= W\frac{N_A}{N_A + N_D} \\ x_p &= W\frac{N_D}{N_A + N_D} \end{aligned} \tag{2.11}$$

Combining this with (2.10) an expression for the depletion layer width is obtained

$$W = \sqrt{\frac{2\varepsilon_r\varepsilon_0}{q}\left(\frac{N_A + N_D}{N_A N_D}\right)V_{bi}} \tag{2.12}$$

In the case of $N_A >> N_D$ one talks about a one-sided junction and the equation for the depletion layer width reduces to

$$W = \sqrt{\frac{2\varepsilon_r\varepsilon_0}{qN_D}V_{bi}} \tag{2.13}$$

For $N_D >> N_A$ an equivalent expression can be given.

Forward and reverse bias

When a bias voltage is applied to the p-n junction, one has to distinguish between two biasing modes. A forward bias corresponds to a positive voltage applied to the anode relative to the cathode. A reverse bias means applying a negative voltage.

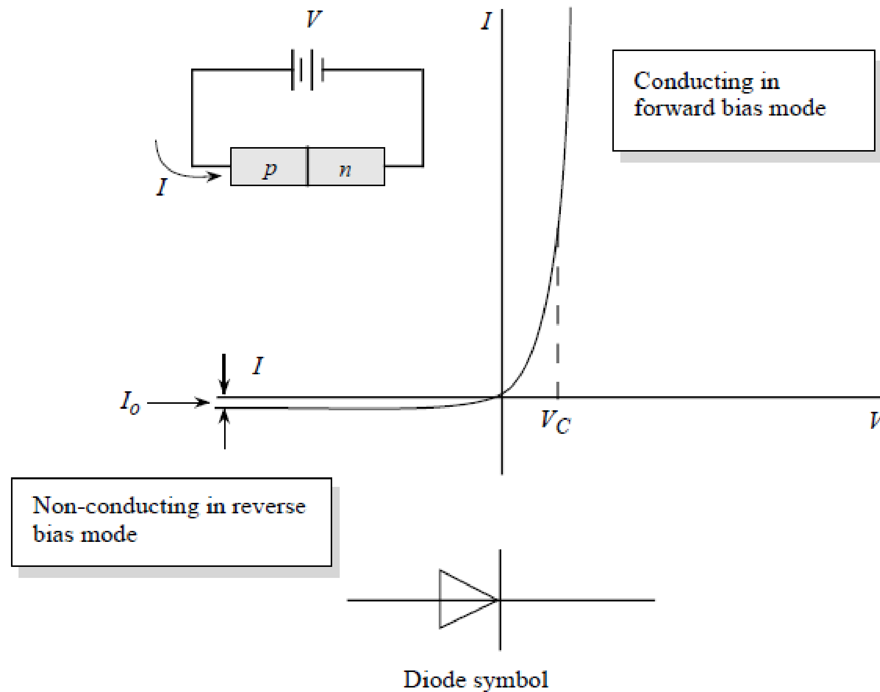

Figure 3: Ideal diode IV-characteristic [11]

By using a bias voltage the total potential across the device is the built-in potential minus the applied voltage. When a voltage is applied to a p-n diode, the exact balance between diffusion and drift current is destroyed. In the forward bias regime, the minority carrier current over the junction increases exponentially. This is because of a decrease of the junction voltage by applying a forward voltage. Then the drift current does not completely compensate the diffusion current anymore and current flows across the junction. The leading effect for the current here is the minority carrier injection. In reverse direction, on the other hand, the current saturates like one can see in Figure 3. Almost no current flows since by applying a reverse voltage the junction voltage is increased. Now the junction voltage is larger than the built-in voltage and carriers are not able to cross the junction anymore. Just a very small negative current flows in the reverse bias region resulting from the flow of minority carriers being attracted by the electric field. [12]

The applied voltage is proportional to the difference of the quasi Fermi levels of the n- and p-type quasi-neutral regions. As said before by applying a bias in reverse direction the potential increases and so the depletion layer width increases too. By applying a voltage in

forward direction the potential decreases and so does the depletion layer width. Figure 4 shows the influence of biasing on the depletion layer width as well as on the potential of the p-n junction. [12]

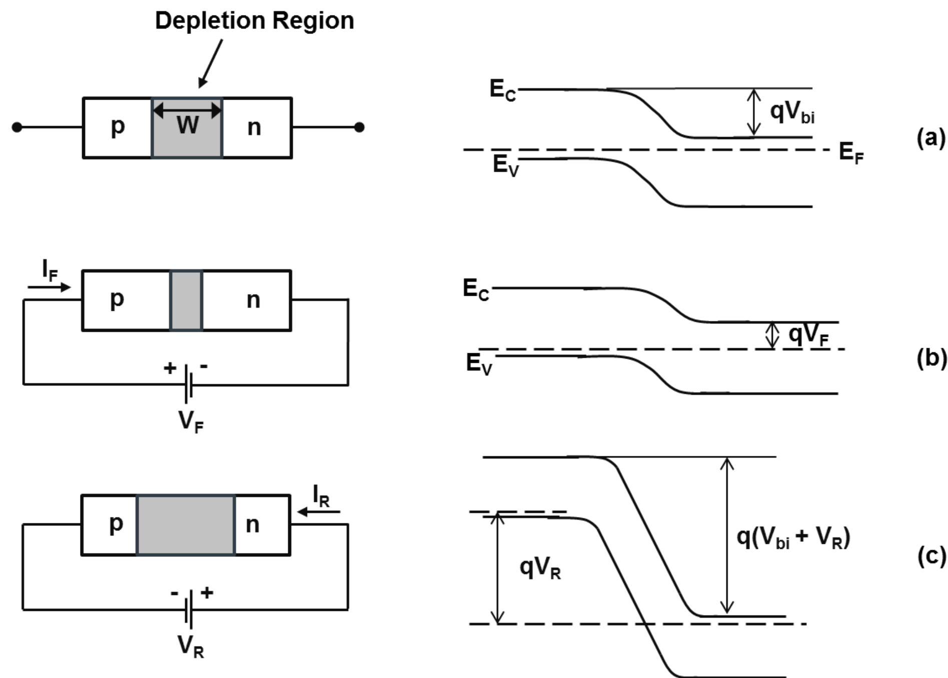

Figure 4: Biasing modes – depletion layer width and energy bands: (a) 0V bias, (b) forward bias, (c) reverse bias [8]

To account for that, equation (2.12) has to be modified to

$$W = \sqrt{\frac{2\varepsilon_r \varepsilon_0}{q}\left(\frac{N_A + N_D}{N_A N_D}\right)(V_{bi} - V)}. \qquad (2.14)$$

2.1.2 Current-Voltage characteristic of a p-n diode

The following section follows the book by Sze [8].

The ideal diode characteristic assumes again the abrupt depletion layer approximation, the Boltzmann approximation, the low injection assumption and that no generation current exists in the depletion layer. More details about these assumptions can be found in [8]. Because a photodiode operates in reverse bias region, this direction is the one of interest for further discussions.

$$n \equiv n_i exp\left[\frac{q(\mathrm{E}_F - \mathrm{E}_i)}{kT}\right]$$
$$p \equiv n_i exp\left[\frac{q(\mathrm{E}_i - E_F)}{kT}\right] \qquad (2.15)$$

In (2.15) the Boltzmann relations for electrons and holes are shown where E_F is the Fermi level and E_i the intrinsic level. At thermal equilibrium the product of p times n is equal to n_i^2. When a voltage is now applied the latter does not apply anymore because the minority-carrier densities on both sites change. Let us define Φ_p and Φ_n as the quasi Fermi Levels for holes and electrons. Then the product of p and n is given by

$$pn = n_i^2 exp\left[\frac{q(\Phi_p - \Phi_n)}{kT}\right] \qquad (2.16)$$

When $\Phi_p = \Phi_n$ thermal equilibrium is reached and as stated above, $pn = n_i^2$ applies again.

For forward bias $(\Phi_p - \Phi_n) > 0$ and $pn > n_i^2$; for reverse bias, on the other hand, $(\Phi_p - \Phi_n) < 0$ and $pn < n_i^2$.

This leads to an expression for the current density of holes or electrons that looks as follows

$$J_p = -q\mu_p p \nabla\Phi_p$$
$$J_n = -q\mu_n n \nabla\Phi_n \qquad (2.17)$$

i.e., that the current densities are proportional to the gradient of the electron and hole quasi Fermi levels.

The difference of the electrostatic potential across the junction is then given by

$$V = \Phi_p - \Phi_n \qquad (2.18)$$

From a combination of Equation (2.16) and (2.18) the electron density n at the position x=-x_p (at the boundary of the space charge region on the p-side), can be written as

$$n_p = \frac{n_i^2}{p_p} exp\left(\frac{qV}{kT}\right) = n_{p0} exp\left(\frac{qV}{kT}\right) \tag{2.19}$$

and an equivalent expression can be found for the hole density at the position x=x_n. In (2.19) n_{p0} is the equilibrium electron density on the p-side. Equation (2.19) and the equivalent one for p_n are the most important boundary conditions to get the ideal current-voltage equation.

Using the continuity equations for steady state and in combination with the Einstein relations linking diffusion constants D_p and D_n with the electron and hole mobility respectively an expression for the hole current on the n-side and for the electron current on the p-side can be found.

$$J_p = qD_p \frac{\partial p_n}{\partial x}\bigg|_{x_n} = \frac{qD_p p_{n0}}{L_p}(e^{qV/kT} - 1) \tag{2.20}$$

$$J_n = qD_n \frac{\partial n_p}{\partial x}\bigg|_{-x_p} = \frac{qD_n n_{p0}}{L_n}(e^{qV/kT} - 1) \tag{2.21}$$

The total current is then the sum of the two terms.

$$\begin{gathered} J = J_p + J_n = J_s\left(e^{qV/kT} - 1\right) \\ J_s \equiv \frac{qD_p p_{n0}}{L_p} + \frac{qD_n n_{p0}}{L_n} \end{gathered} \tag{2.22}$$

L_p is known as the hole diffusion length and is defined as $L_p = \sqrt{D_p \tau_p}$ with τ_p being the hole lifetime. The hole lifetime is defined as the time between generating the hole and recombination. This equation is known as Shockley equation and is also referred to as the "ideal diode law". The resulting current-voltage relation was already shown in Figure 3.

Using the ideal diode law the current in reverse direction is given by:

$$|J_R| \sim J_s \tag{2.23}$$

Having a one sided junction the expression for J_S is reduced to either $J_s \approx \frac{qD_p p_{n0}}{L_p}$ or $J_s \approx \frac{qD_n n_{p0}}{L_n}$. With the assumption of a one sided junction, the reverse current can be expressed either as a function of the hole or electron lifetimes or the hole or electron diffusion lengths.

$$|J_R| \sim J_s \approx \frac{qD_p p_{n0}}{L_p} \approx q\sqrt{\frac{D_p}{\tau_p}}\frac{n_i^2}{N_D} \tag{2.24}$$

Using the ideal diode equation one neglects several effects:

The differences to the ideal behavior occur mainly because of the surface effect, generation and recombination of carriers in the depletion layer, tunneling of carriers through the band gap at very high voltages or the series resistance of the leads. Also the low injection condition is not valid anymore. As the latter does not influence the reverse bias region, thus it will not be further discussed here. The surface effect results from ionic charges at the semiconductor surface. Image charges are induced in the semiconductor and surface depletion layer regions are formed. In reverse bias direction there will also occur a junction breakdown at sufficiently high voltages. More details about the surface effect and the junction breakdown can be found in the book by Sze [8].

In silicon p-n diodes the generation current is much bigger than the current resulting from the surface effect. The current resulting from generation in the depletion region is given by

$$J_{gen} = \frac{qn_i W}{\tau_e} \tag{2.25}$$

As one can see the generation current is dependent on the depletion layer width W and, thus, also on the applied voltage. τ_e is the effective lifetime and is a function of temperature.

Taking the generation effect into account, the total reverse current is given by the sum of diffusion components in the neutral regions and the generation current in the depletion region.

$$J_R = q\sqrt{\frac{D_p}{\tau_p}}\frac{n_i^2}{N_D} + \frac{qn_iW}{\tau_e} \tag{2.26}$$

At room temperature the generation current (second term) will be dominant but at sufficiently high temperatures the effect of the diffusion current (first term) will take over. [8]

2.2 Photodiodes

Until now the discussion was about ordinary p-n junctions, which find implementation in many optoelectronic applications. This work deals with photodiodes where a p-n junction is used to convert optical signals into electrical signals. The following section describes how a p-n junction is used as a photodiode and also the most important parameters of photodiodes will be presented. Since this work deals with monolithic integration of photodiodes into CMOS processes, the following part will concentrate on silicon photodiodes.

2.2.1 Optical absorption and carrier generation through photons

When a semiconductor is illuminated with light and a photon hits a valence electron, this electron can reach the conduction band under the condition that the photon energy is large enough and an electron-hole pair is generated. When neglecting exitonic effects, this minimum energy, can be associated with the bandgap energy defining a critical wavelength λ_c. [13]

$$\lambda_c = \frac{hc_0}{E_g} \tag{2.27}$$

The critical wavelength for silicon is 1.12µm corresponding to a bandgap energy of 1.1eV.

For wavelengths larger than λ_c the semiconductor is transparent. In the case where an electron-hole pair is generated, it needs to be separated and collected by electrodes to contribute to an additional current, called photocurrent. This conversion of optical into electrical energy is the absorption of photons in semiconductor materials. [1], [14]

The most important parameter for absorption is the absorption coefficient α. The absorption coefficient is specific for a material and strongly wavelength dependent. It describes how fast the intensity of the light decreases while propagating through a semiconductor. This process can be expressed through the Lambert-Beer's law shown in (2.28)

$$I(y) = I_0 e^{-\alpha y} \tag{2.28}$$

with I(y) as the intensity as a function of the distance from the surface and I_0 as the intensity at the surface, just inside the semiconductor. I_0 is expressed by $I_0 = I_{opt}(1 - R)$, where I_{opt} is the intensity of the incident light before interacting with the material. I_{opt} times R represents the part of light, which is reflected at the surface. α is the absorption coefficient and y the distance from surface. This intensity of light is called irradiance. The Lambert-Beer's law can also be recast in an expression for the optical power by using:

$$P = I \cdot A \tag{2.29}$$

with A being the cross-section for the light incidence. [14]

The absorption coefficient is inverse proportional to the wavelength and proportional to the imaging part of the complex refractive index.

$$\alpha = \frac{4\pi\kappa}{\lambda} \tag{2.30}$$

The penetration depth of light is the inverse of the absorption coefficient and gives the depth where the intensity has decreased to a value of 1/e of the initial intensity. [14]

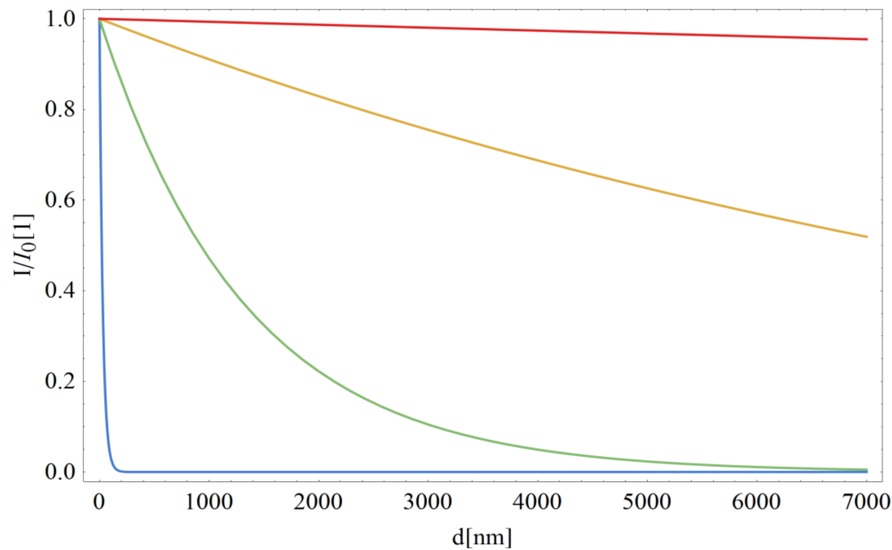

Figure 5: Irradiance of light at different wavelengths as a function of the distance from surface, blue line: λ=400nm, green line: λ=600nm, yellow line: λ=800nm and red line: λ=1000nm

Figure 5 shows how the irradiance decays with increasing propagation through silicon at four different wavelengths. One can clearly see that light with a small wavelength (blue line in Figure 5), is already very low in intensity close to the surface. Light with long wavelengths (red line), penetrates very deeply into the material still having a quite high intensity.

Because of the strong wavelength dependence of the absorption coefficient (shown in Figure 6), the wavelength range in which a photodiode generates an appreciable photocurrent is restricted. For wavelengths beyond λ_c, no light is absorbed and, consequently, no current is generated. For wavelengths shorter than λ_c the absorption coefficient starts to increase. How fast the absorption coefficient increases with decreasing wavelength depends on the type of semiconductor. For direct bandgap semiconductors this increase is very steep while for indirect bandgaps like silicon the slope is smaller. [14] For really short wavelengths in the blue and UV region, α is very large and the light is absorbed in surface near regions where the recombination rate is high and where a significant fraction of the excitation processes occur outside the depletion region. Because of this, the photocurrent corresponding to light with very low wavelength is smaller. [8] This behavior can also be seen in the practical part of this work, where I did responsivity measurements.

Table 1 gives the absorption coefficients for silicon for the different wavelengths used in Figure 5 and Figure 7.

Table 1: Absorption coefficient in cm^{-1} for the wavelengths used in Figure 5 and Figure 7

Wavelength λ [nm]	Absorption coefficient α [cm^{-1}]
400	12.15×10^4
600	5.22×10^3
800	936.51
1000	67.32

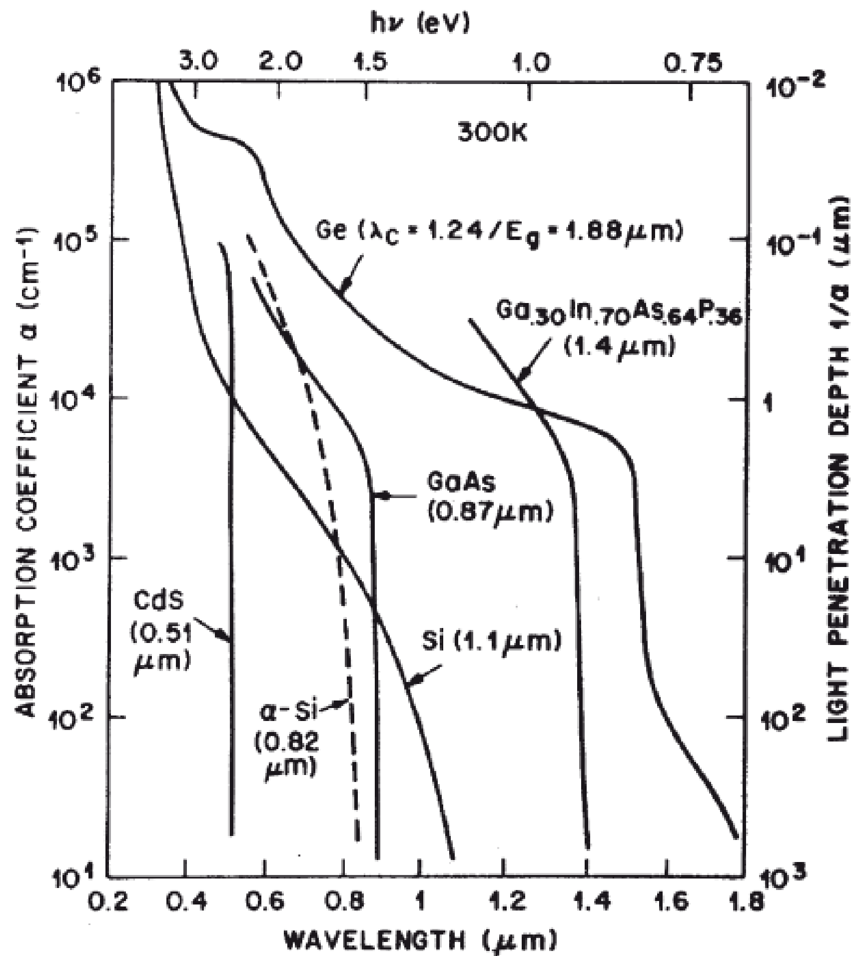

Figure 6: Absorption coefficient and penetration depth as a function of wavelength and energy [15]

The Lambert-Beer's law can also be recast into an expression for the generation rate of electron hole-pairs in the semiconductor:

$$G(y) = \frac{\alpha I_0}{h\nu} e^{-\alpha y} = \frac{\alpha P_0}{Ah\nu} e^{-\alpha y} \tag{2.31}$$

Where α is the absorption coefficient, P_0 the optical power at the surface right inside the semiconductor, A is the cross-section for the light incidence and hν the energy of the incident light. [14]

In the following plot, the ratio between generation rate and I_0 for different wavelengths as a function of propagation depth is shown.

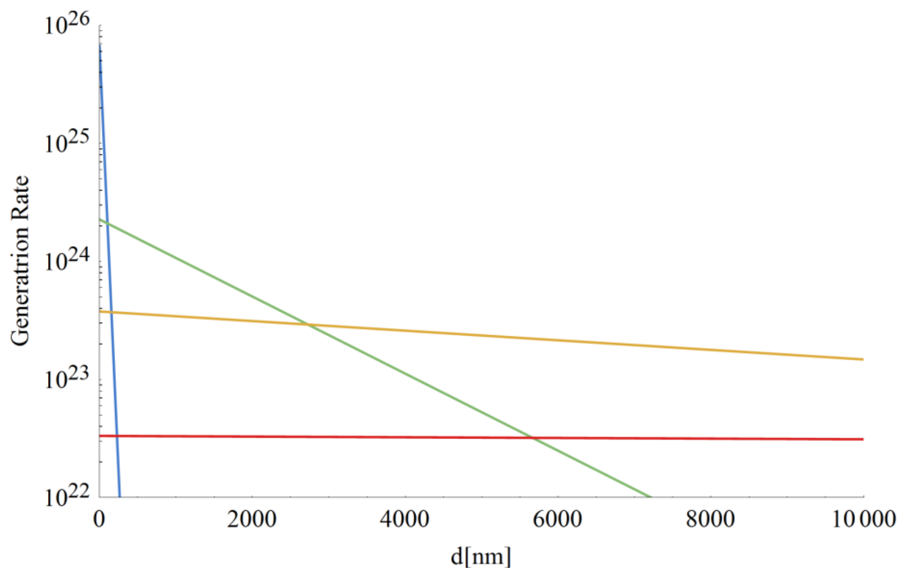

Figure 7: Generation rate divided by I_0 as a function of propagation depth for different wavelengths, blue line: λ=400nm, green line: λ=600nm, yellow line: λ=800nm and red line: λ=1000nm

In Figure 7 one can see very clearly that the generation rate is dependent on the absorption coefficient α. At short wavelengths α is very big as one can see in Table 1, resulting in a very high generation rate at the surface. This can be seen comparing the blue line in Figure 7 to the other lines. Minding the logarithmic scale in the plot, a really big difference of the generation rate can be seen. Even tough, the generation rate is very high at regions very close to the surface; it decays very fast with increasing distance from the surface, because of reasons discussed earlier regarding the Lambert-Beer's law.

The photocurrent resulting from the dissociation of electron-hole pairs and collection from carriers at electrodes can be seen as an additional current flowing in reverse direction.
This photocurrent can be seen as an increase of the current in reverse direction, which is larger the higher the intensity of light is. [12]

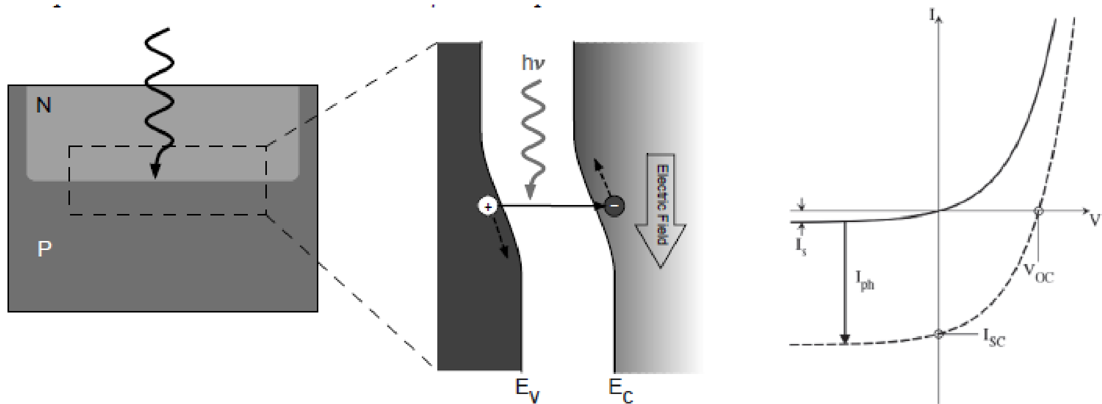

Figure 8: Effect of electron-hole pair generation through light resulting in photocurrent [1]

The ideal diode voltage-current equation shown in (2.22) extends now to

$$J = J_s\left(e^{qV/kT} - 1\right) - I_{Ph} \tag{2.32}$$

with an extra term accounting for the photocurrent I_{Ph}.

To analyze the photocurrent one has to distinguish between two different parts, which are contributing to the photocurrent. First, a fast part resulting from carriers generated inside the space charge region. These carriers are directly separated by the electric field and are called the drift contribution. Second, a slow contribution, resulting from carriers produced outside the space charge region. These electrons and holes have to diffuse to the space charge region to be collected at the electrodes and contribute to the photocurrent.
How big the diffusion contribution to the photocurrent is depends on the lifetime of the carriers in the semiconductor material. As mentioned in section 2.1.2 the lifetime is defined as the time between the generation of a carrier and its recombination. If the lifetime is at least as long as the time the carrier needs to diffuse to the space charge region, it will contribute to the photocurrent.

To get a better idea of the regions in the device were the two different contributions to the photocurrent are generated, the three regions one has to distinguish are shown in Figure 9.

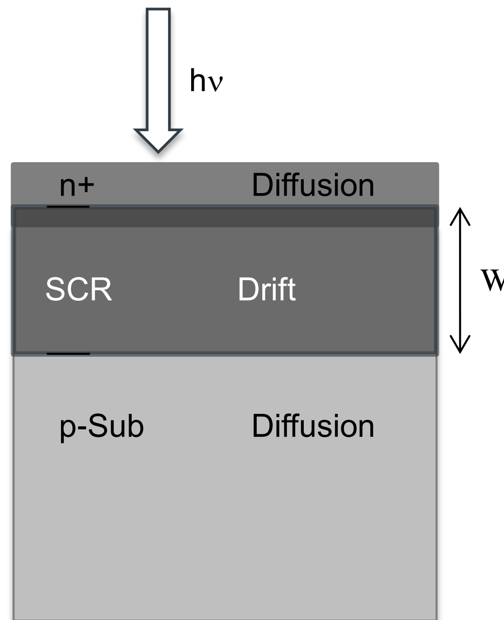

Figure 9: Drift and diffusion current regions contributing to the photocurrent

In Figure 9 one can see a p-n diode where a junction is formed between a very shallow but highly doped n-region and a lower p-doped substrate. The dark grey shading indicates where the space charge region is formed. As shown in section 2.1.1 the depletion layer width is strongly dependent on doping concentration, thus leading to just a very narrow space charge region in the very highly doped n-region. In the vey lowly-doped p-substrate on the other hand the space charge region is big. Looking at Figure 9 one can see that there are two diffusion regions. A small one in the n-region, above the space charge region and a large one in the p-substrate underneath the space charge region. The one in the p-substrate has a bigger effect because of the very low doping of the p-substrate, which results in a longer lifetime and thus to less recombination. [14] As will be shown in the practical part the diffusion component from the substrate is playing a very big role in our devices.

2.2.2 Types of photodiodes

One possibility to tune the performance of photodiodes, for certain applications, was already explained in 2.1, is on the one hand, to vary the doping concentration to increase the space charge region width and on the other hand to vary the junction depth to reach

wavelength sensitivity in the desired wavelength range. Another possibility would be using semiconductor materials with different band gap energies. Doing so, monolithic integration is not possible anymore, what is the goal of this work, and thus, not a topic in this work.

Another way to optimize certain parameters can be reached through design variations. Until now we were talking about photodiodes out of ordinary p-n junctions. Now further types of silicon photodiodes will be presented.

PIN photodiodes

To be as efficient as possible the region where photo-generated carriers are generated has to be as large as possible. To increase the speed at the same time the diffusion contribution has to be minimized and the drift contribution has to be maximized. In order to do so the space charge region has to be increased. One possibility is to use high reverse voltages, but there is also a geometry related way to further increase the width of the depletion region, without being dependent on a certain reverse bias. [1] This is achieved by inserting an intrinsic region between a highly doped p- and n-type region, like shown in Figure 10, resulting in a p-i-n junction.

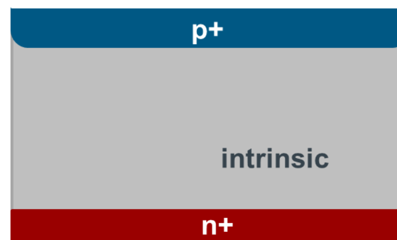

Figure 10: Schematic build-up of a PIN photodiode

This, results in an essentially charge free intrinsic region and just a very narrow space charge regions in the highly doped p- and n-type semiconductors. Therefor the space charge region width corresponds to the width of the intrinsic region and, thus, can be tuned in the fabrication process. To have a perfect efficiency the intrinsic layer width should be larger than the absorption length. Figure 11 shows how the carrier distribution, the charge distribution, the electric field and the band diagram of a pin photodiode look like.

To increase the speed of a pin photodiode the reverse bias has to be increased because the way carriers have to move before they are collected is now longer due to the wider space charge region. But on the other hand the undesired diffusion term is eliminated. The only regions where carriers could diffuse from are the highly p^+- and n^+-doped semiconductors. As mentioned already before, the diffusion from regions with high doping is small because of the high recombination rate.

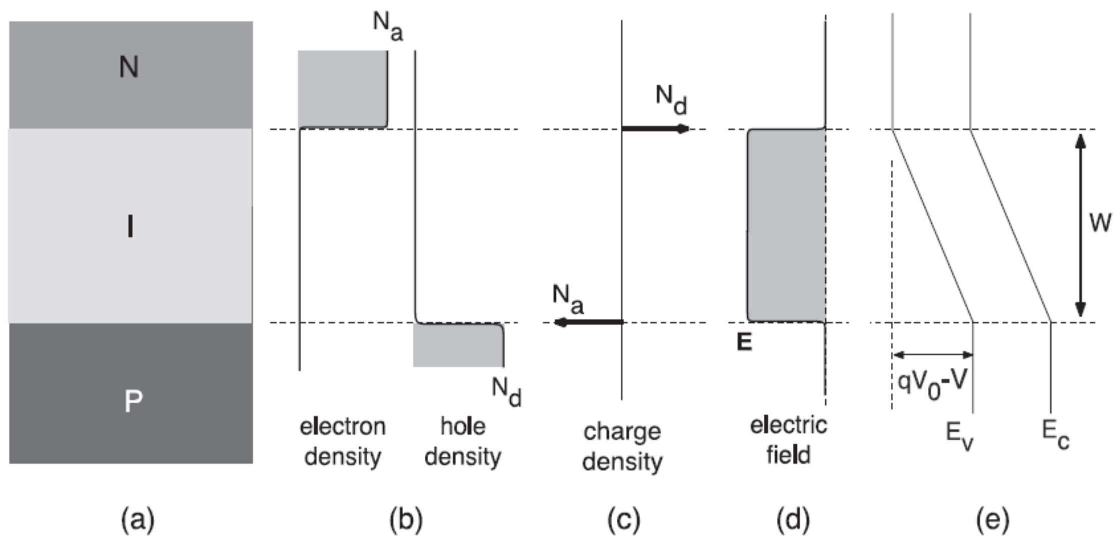

Figure 11: PIN photodiode: (a) PIN photodiode schematic structure, (b) carrier distribution, (c) charge distribution, (d) electric field distribution and (e) band diagram of a pin junction under reverse bias [1]

Out of Figure 11 one can see that the range where the electric field has its maximum is not a point anymore. The field remains at its maximum value over the whole intrinsic layer. [1]

Avalanche photodiodes

To be able to detect very weak optical signals like single photon events, an avalanche photodiode can be used. The design, shown in Figure 12, is very similar to pin photodiodes but the photodiode is operated with very high reverse bias voltages where impact ionization occurs. Carriers leading to impact ionization as well as carriers generated by impact ionization are causing more and more impact ionization events resulting in the avalanche effect, which amplifies the photo-generated current. [1]

The current gain, resulting from the avalanche effect is known as the multiplication factor. This factor is dependent on the depletion layer width and the electron and hole ionization rates. The maximum multiplication is limited through the effective series resistance and also through the breakdown voltage. [8]
Another possibility to use an avalanche photodiode is to operate it in Geiger mode, which means operation under a reverse bias beyond the breakdown voltage. In that case only one electron-hole pair, generated by a single photon, causes the avalanche effect and a large current signal is generated. Photodiodes, which are able to operate in Geiger mode, are able to count single photons and are, thus, also called single photon avalanche diodes. [1]

Because of operation near breakdown, a guard ring is used to avoid surface breakdown in avalanche photodiodes. By adding a guard ring next to the active region, as shown in Figure 12, one prevents forming a lateral depletion region as well as a depletion region at the surface. [1]

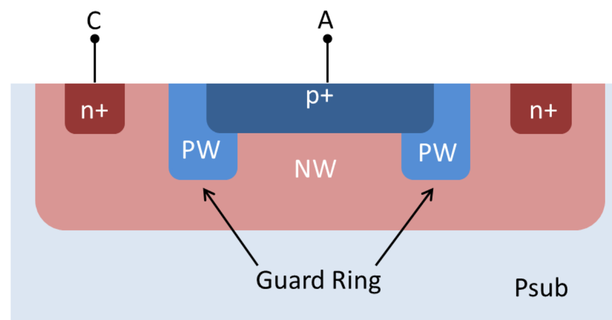

Figure 12: Schematic build-up of a single photon avalanche diode, including a p-well guard ring [1]

2.2.3 Photodiode parameters

In this section the most important parameters to characterize photodiodes will be introduced. The quality of a photodiode depends on the spectral responsivity and the quantum efficiency as well as on the dark current and response time.

Quantum efficiency

One can distinguish between two different definitions of quantum efficiency. On the one hand there is the external quantum efficiency and on the other hand the internal quantum efficiency. The external quantum efficiency η is defined as the number of electron-hole pairs contributing to the photocurrent, divided through the number of incident photons. A part of the incident light is reflected. This part is not contributing to the internal quantum efficiency. Thus the internal quantum efficiency is defined as the number of electron-hole pairs, which contribute to the photocurrent divided by the number of photons, which really penetrate into the semiconductor. [14]

Responsivity

The spectral responsivity is the photocurrent divided by the incident optical power. The equation for the responsivity and its relation to the quantum efficiency are shown in (2.33). [14]

$$R = \frac{I_{ph}}{P} = \frac{q\lambda}{hc} \cdot \eta \ \left[\frac{A}{W}\right] \tag{2.33}$$

The responsivity as well as the quantum efficiency are wavelength dependent, so talking about a responsivity value one has also to specify the wavelength. [14]

Response time

The response time is defined as the time a photodiode needs to respond to a sudden change of light level and gives information about the speed of a photodiode. It is expressed by three parameters, the rise and fall time and the 3dB bandwidth. The rise and fall time are the time differences between the 10% and 90% values of the stationary photocurrent. [14] The 3dB point indicates the point where the power has dropped by half, thus, the 3dB

bandwidth gives the range of frequency where the signal has still more than half of its maximum power. [16]

Dark current

The dark current is the current which flows without illumination in reverse bias direction. It is next to noise the limiting factor at low-light levels. [9] The dark current depends on doping concentration, lifetime of the minority and majority carriers and temperature.

Generally dark current is caused by one of the following sources [17]:

a. Defects within the depletion region, acting as generation-recombination centers
b. Carriers generated thermally in the bulk, diffusing to the depletion region
c. Surface states leading to generation at the surface
d. Tunneling currents
e. Impact ionization

Generation-recombination current

Carriers, which are generated by defects or thermal excitations in the depletion region, are a big contribution to the dark current. These carriers are swept out of the depletion region from the electric field the same way photo-generated carriers are. [1] Their contribution to the dark current is given by [17]

$$I_{dep} = \frac{qn_iW}{2\tau_{gen}} \tag{2.34}$$

n_i is the intrinsic carrier density, W the depletion region width and τ_{gen} the generation lifetime. Because of the dependence on the applied bias, the generation-recombination current increases with the square root of the applied bias. [1]

Diffusion current

Minority carriers (electrons on the p-side and holes on the n-side) in the bulk underneath the pixels can diffuse into the depletion region and are collected by the electrodes and, therefore, contribute to the dark current. [1] The diffusion current is calculated using

$$I_{diff} = -qD_n \frac{\partial n(x)}{\partial x} = \frac{qD_n n_i^2}{L_n N_A}$$
$$I_{diff} = -qD_p \frac{\partial p(x)}{\partial x} = \frac{qD_p n_i^2}{L_p N_D} \quad (2.35)$$

D_n and D_p are the diffusion coefficients for electrons and holes, L_n and L_p the diffusion lengths for electrons and holes and N_A and N_D the acceptor and donor concentrations respectively. [17]

Surface leakage current

At the surface of the device there is a high density of surface charge and interface states. These states can again act as generation-recombination centers that contribute to the dark current according to

$$I_{SS} = \frac{1}{2} q s_0 n_i \quad (2.36)$$

where s_0 is the surface generation velocity, q is the charge and n_i is the intrinsic carrier concentration. [17] To avoid surface leakage current, a passivation layer is used. [1]

Tunneling currents

Working under higher reverse bias it is possible that the conduction band energy E_C on the n-side is lower than the valence band energy E_V on the p-side. Under these circumstances an electron in the valence band on the p-side has the possibility to tunnel into the conduction band on the n-side. This effect is known as band-to-band tunneling. Another possibility is tunneling involving inter-band trap states. If such states exist in the depletion region and a sufficient high reverse bias is applied, a trapped electron has the possibility to tunnel to the conduction band. This process is known as trap-assisted tunneling. Both of these effects are strongly dependent on the applied reverse voltage. [1]

Impact ionization

Under reverse bias, the carriers are accelerated by the electric field and collide with atoms in the crystal. If the acceleration is large enough, carriers can reach enough energy to generate new electron-hole pairs. These electron-hole pairs can be a further contribution to the dark current. This process is called impact ionization and was already mentioned talking about avalanche photodiodes. [1]

One can see that there are a lot of possible sources for dark current, making the evaluation of dark current behavior complicated. In the further work one will see that the dark current is a very important parameter for photodiodes and the knowledge of the different sources for dark current is very important.

3 CMOS SENSORS

It is of great interest to improve and further develop photodiodes as the light-sensing element of CMOS sensor systems and CMOS imagers.
This chapter will provide a short introduction to the history of CMOS sensors, how they work and what the advantages are with respect to other leading technologies.

3.1 Historical background

Already in the middle of the 60s MOS diodes were used as light sensitive elements. At that time not only the conversion of photons into electrons was known, also the possibility to read a signal from a pixel array was already a topic. A drawback of these early CMOS image sensors was the large size of the transistors used in CMOS processes that led to large pixels, which further led to a small fill factor and poor performance. Another problem was the noise and the high dark current. Because of these reasons CMOS imagers and detectors lost importance and interest in the early 70s where they were largely replaced by charge-coupled devices (CCD). The improvements in CMOS technologies over the years, however, led to a comeback of CMOS sensors in the early 90s. After some years of further improvement, CMOS sensors reached a performance level comparable to CCDs and are not only used for low-end imaging products these days, but have become a serious competitor for CCDs in a variety of applications. [1]

3.2 Advantages and disadvantages

The following information are collected from [1], [18] and [19].
Today CMOS sensors offer many advantages compared to CCD sensors. CMOS sensors provide lower power consumption, lower voltage operation and lower costs. Due to the fact that CMOS sensors use the same circuit technology as common microprocessors and memory chips the compatibility with standard CMOS technology and the possibility of monolithic integration of readout electronics is a big advantage. Another benefit is the reduction of blooming and smearing effects which is a big problem with CCD sensors. CCD sensors cannot guarantee full functionality over the whole temperature and illumination range needed in new applications like automotive sector. With increasing the

temperature, the dark current of CCDs is increasing drastically, leading to a poor signal to noise ratio.
On the other hand there are still drawbacks regarding to CCD technology. One problem of CMOS sensors is the sensitivity, which is basically restricted through the fill factor and the quantum efficiency. The fill factor, talking about photodiodes, is defined as the ratio of light sensitive area to pixel size. Because every pixel contains its own read out electronics and amplifiers, the fill factor is reduced compared to a CCD. Another problem to deal with is noise and dark current. The CMOS technology brings several noise sources with it, which is particularly problematic at low illumination levels. Thus, one has to deal with lower image quality in comparison to CCDs and because of that CCD imagers are still predominant in the area of high quality "still" photography.

Besides the differences and various advantages of the two technologies, the improvement of CMOS sensors opens new areas of application because of the big advantages of lower costs and the possibility of monolithic integration. Examples are IR-vision, x-ray application for space or medical use and with further improve of the noise and the dark current, also for low-light applications, where both the CMOS as well as the CCD technologies are not perfect.

3.3 Basic principles and operation of CMOS sensors

There are several possibilities the light-sensing element of a CMOS sensor can look like. One can distinguish between photo-gates, charged coupled devices, as mentioned before, and photodiodes. [19]

In this chapter a short introduction of the structure and operating principle of different kinds of CMOS sensors, using photodiodes as light-sensing element, will be given. What all of the following structures have in common is the conversion of photons into electrical charge using a photodiode. This process was explained in earlier sections. Further the charge is converted into a measureable voltage. The difference of the technologies lies in the read out mechanism.

3.3.1 Passive Pixel Sensor (PPS)

Structure

The first CMOS pixel sensors used were passive pixel sensors (PPS). A schematic image of a PPS is shown in Figure 13. The pixel consists of the photodiode and an addressing transistor to connect the read out structure with the pixel. In the passive pixel sensor no amplification transistor is included inside the pixel. The pixel is addressed by opening the row select transistor RS. The advantages of this architecture are the possibility of realizing a very small pixel size and the high fill factor while the drawbacks are low sensitivity and high noise because of the large vertical bus capacitance compared to the pixel capacitance. [19]

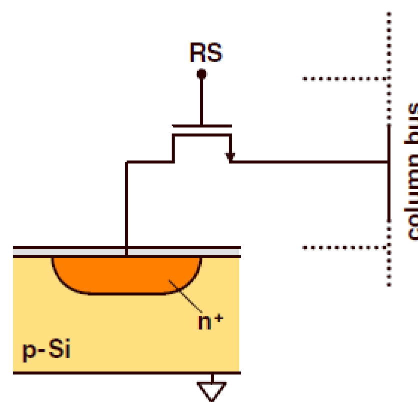

Figure 13: Schematic structure of passive pixel sensor with RS as the row selection transistor [20]

Operating principle

The photodiode is reversed biased or used at zero bias voltage during illumination. The reverse voltage across the photodiode decreases because of impinging photons during the illumination time. The remaining voltage across the diode is measured after the illumination time. The difference from the original value is proportional to the amount of photons hitting the photodiode during illumination. After resetting the photodiode, by closing the row selection transistor again, it is ready for another illumination time. [20]

3.3.2 Active Pixel Sensor (APS)

Structure

The Active Pixel (APS) Sensor is an improved CMOS sensor technology. Figure 14 shows the schematic structure of an APS. In addition to the addressing transistor (RS) also a source follower (SF) working as amplifier and a reset transistor (RST) are implemented. The implementation of an in-pixel amplifier improves the performance and minimizes the power dissipation. But this technology also brings some disadvantages like fixed pattern noise. [20]

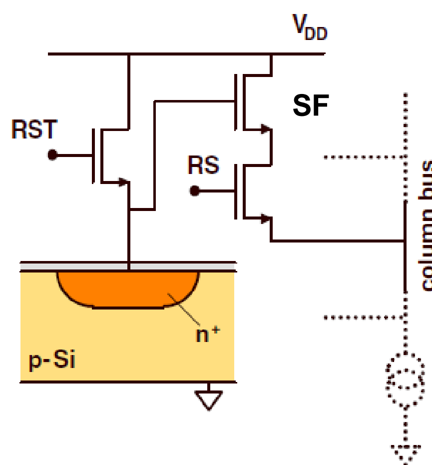

Figure 14: Schematic structure of Active Pixel Sensor with RST as reset transistor, RS as addressing transistor and SF as source follower [20]

Operating principle

The operating principle of the APS is very similar to the one of the PPS. The difference lies in having the amplification inside the pixel. At the end of the illumination, the pixel is addressed by the addressing transistor RS and transported out of the pixel through the source follower SF were the amplification takes place. With the reset transistor RST the photodiode is reset again. [20]

3.3.3 Active Pixel Sensor using a pinned photodiode

Structure

A further performance improvement can be achieved by using a pinned photodiode. The schematic structure can be seen in Figure 15. In addition to the actual photodiode another

so called pinned photodiode is added. This photodiode is connected to the readout circuit, which looks the same as in an APS, by a transfer gate TX. Like this the photodiode is separated from the readout circuit. [20]

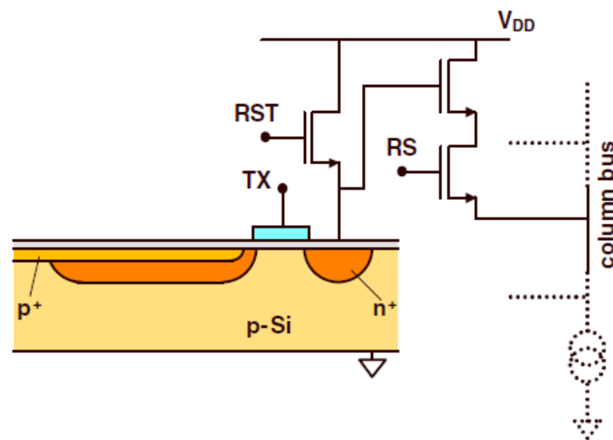

Figure 15: Schematic build-up of APS with a pinned Photodiode, TX is the transfer gate [20]

Operating principle

The conversion of the photons is done in the pinned photodiode and again with the reset transistor the photodiode is reset after illumination and a first measurement of the output voltage is done. By activating the transfer gate the pinned photodiode is emptied and all charges are transferred to the readout node. After the transfer the output voltage is measured again. The result is the subtraction of the two measurements; this method is called correlated double sampling. Further information can be found in [20] and [21].

By using this more complex structure, including 4 transistors, the noise of the readout circuit can be completely eliminated because of the correlated double sampling. [20] Another advantage is the increase of the depletion layer width leading to a better light sensitivity. Also the leakage current is reduced because of the double junction. Because of the structure of the read out circuit, consisting of four transistors and five interconnections, the quite complex architecture leads to a quite low fill factor and it is very hard to achieve small pixel sizes. [20]

One can see that all three different architectures have their advantages and disadvantages and it depends on the application which one fits best and is, therefore, used.

3.4 CMOS sensor structure

Figure 16 shows the schematic structure of CMOS sensor architecture. [20] It contains an array of identical pixels, of the types discussed before, the orange region of the single pixels indicates the active area of the pixel and the transistor indicates the read out circuit. One can see how a larger read out circuit reduces the active area, thus reducing the fill factor. Furthermore, a vertical scan circuit for row selection, a horizontal scan circuit to amplify and multiplex the signal and an output with the possibility of further amplification are included to the array structure. [18]

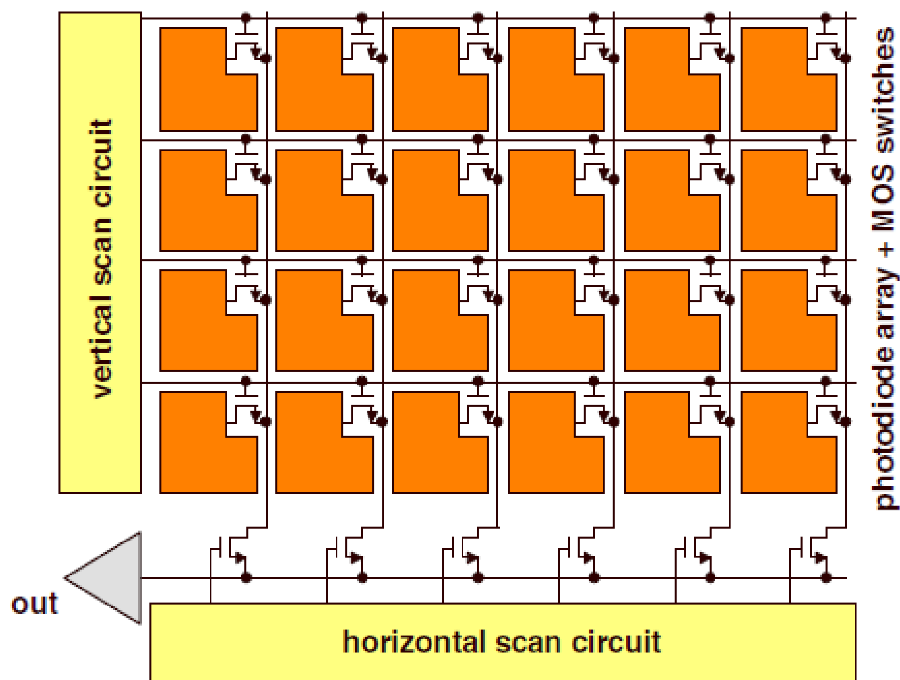

Figure 16: Architecture of a two-dimensional CMOS image sensor [20]

3.5 Sources of noise

The main parameter, limiting the performance of CMOS sensors is noise. In order to be able to minimize this disturbing effect one has to know the sources. One can distinguish between two main sources of noise, the temporal noise and the fixed pattern noise. [19]
Different sources for temporal noise can be found. The first source is the pixel noise, which originates from photon shot noise, which is because of the statistical variation of the number of impinging photons on the array during the illumination [20], thermal noise (reset or kt/C noise) resulting from resetting after the pixel read out, and dark current shot noise. Further types of noise are column amplifier noise, programmable gain amplifier noise, ADC noise and overall temporal noise. [19]

The second big group of noise is the fixed pattern noise, which is defined as the fixed variation in the output between pixels by having a uniform input applied. In a perfect sensor each pixel should have the same output when applying the same input, but this is not the case in actual pixel arrays. [19]

With this knowledge pixel sensors can be further improved with respect to low noise, high dynamic range, high sensitivity, high fill factor and low power consumption. Of course it is hard to achieve all these factors in one design, thus finding the right compromises between these parameters again depends on the intended application.

4 MEASUREMENT SETUP

The electrical as well as the optical measurements were done with a Cascade Microtech measurement system. In Figure 17 a picture of the used Cascade is shown. The system includes a moveable and heatable chuck, the possibility to connect four tips to a semiconductor parameter analyzer and a microscope. Additional to the standard build-up, two light sources are added for doing optical measurements. A tunable xenon light source and a source including two LED and two laser light sources with wavelengths of 670nm and 850nm are used for different measurement setups and applications.

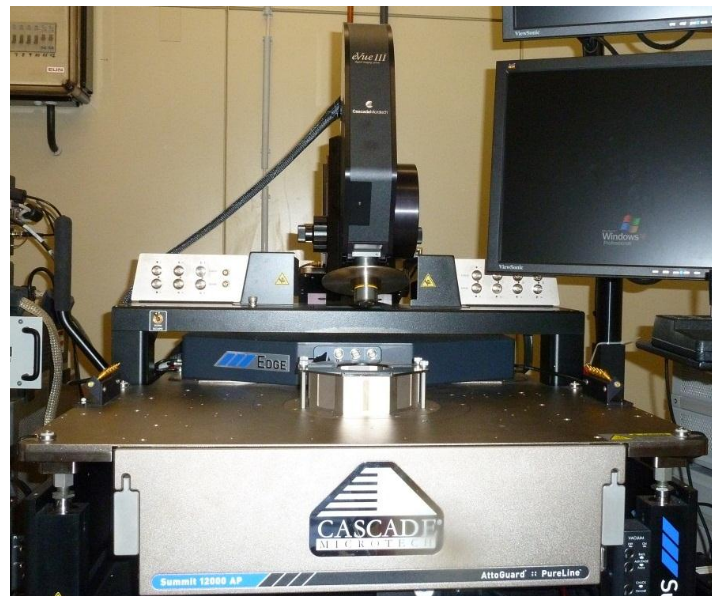

Figure 17: Measurement setup showing the Cascade Microtech point probe station

4.1 Dark current measurement

For dark current measurements, in the normal case, just two tips are necessary. If in certain cases a measurement of more than one diode in parallel is necessary, like done in this work, one has also the possibility to add more tips to the setup. The voltage is applied selectable either over the cathode or the anode. The cathode and anode current is detected in dependence on the applied voltage by a semiconductor parameter analyzer. For doing dark current measurements no light should reach the wafer.

4.2 Responsivity measurement

For responsivity measurements a tunable monochromatic light source measurement system is used. The light source consists of a xenon lamp followed by a monochromator. The block diagram of the light source is shown in Figure 18.

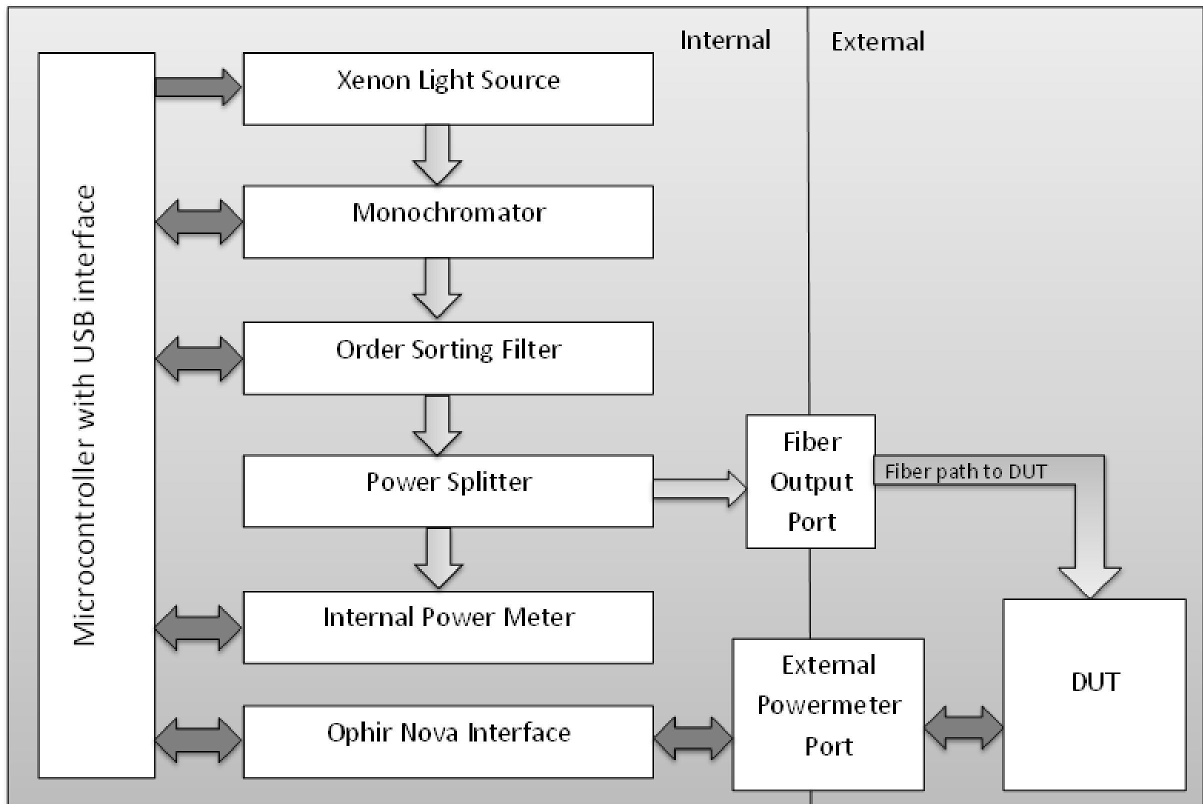

Figure 18: Block diagram of the tunable monochromatic light source [22]

To generate white light, a 175 W xenon light bulb is used. The spectrum ranges from 400 to 900 nm. To achieve monochromatic light, a monochromator is placed after the xenon lamp. A fine pitch is used to reach the spectral components of the white light. Through a small slit just a narrow portion of the spread light is transported. Due to the working principle of the monochromator, using a diffraction mechanism, not only light with fundamental color is produced but also higher orders. A sorting filter is used to overcome this problem. After the sorting filter, a power splitter is used to split the beam into two parts with the same power. One of the two paths goes to an internal power meter where the actual power is measured. The second beam goes to the fiber output port and through the fiber path to the device. At the device the light is focused on the sample with a fiber,

shown in Figure 20, of a diameter of 62.5µm. [22] The fiber diameter is dependent on the distance between the fiber and the sample. To achieve reproducible measurement results this distance should always be the same.

The power of a xenon lamp is very unstable. Therefore the optical power is measured continuously. That way the measurement of the external device can be referenced by the internal power. The internal optical power measurement together with an internal wavelength dependent calibration curve ensures the validity of the measurements. It is also possible to measure the optical power which is directly at the device under test (DUT) with an external power meter. This is also used to do the spectral calibration where a calibration curve is recorded using an already calibrated photodiode. The internal calibration curve leads to a correction of the actual optical power measured internal in respect to the values of the external optical. [22]

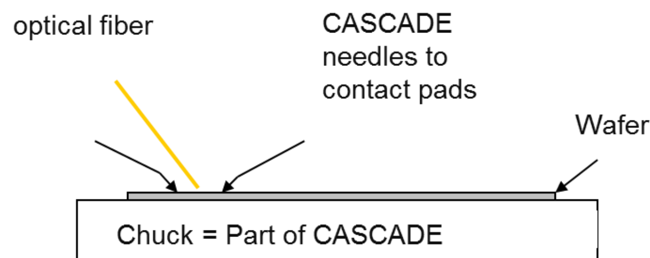

Figure 19: Schematic measurement setup for optical measurements

With this setup the photocurrent is detected in dependence on the wavelength. Dividing the photocurrent through the measured optical power leads to the responsivity like explained in section 2.

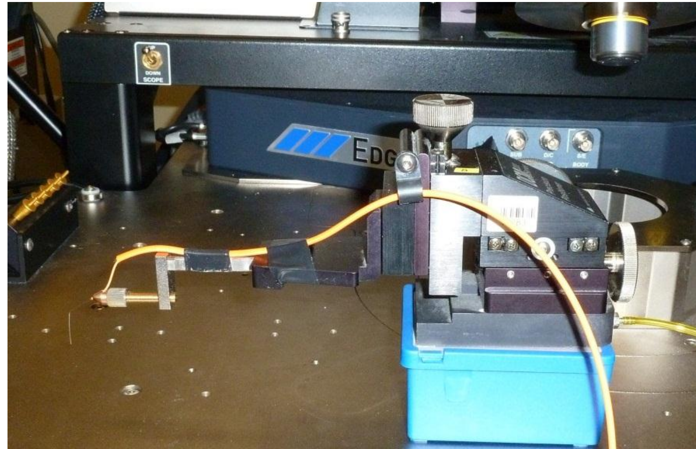

Figure 20: Fiber for optical measurements

At the end of this section it must be mentioned that for the responsivity measurements a very strong dependence of the results on the calibration curve of the equipment was found. Especially the low wavelength region is very sensitive. By repeating measurements, differences were found and after comparing the calibration curves also there the differences were observed. It is very important to take care that while doing calibration absolutely no light reaches the reference diode in order to get reproducible results. Furthermore one has to take care that the optical path is not changed after the calibration, otherwise the calibration has to be repeated.

4.3 Crosstalk measurement

Several ways to measure the crosstalk of a photodiode exist. In this work only the one used in the practical part is discussed.

In this particular case backside illumination was necessary making impossible to contact with the tips. For contacting the anode and the cathode without tips the device is in a package including connections for wires. The chuck is moved and like this the light source which is not touching the device is stepping over the desired region while the photocurrent is detected in dependence on the position. As light source LEDs with wavelengths of 670nm and 850nm are used.

5 EVALUATION OF DIFFERENT WELL COMBINATIONS CCCURRING IN A HIGH VOLTAGE PROCESS

5.1 Structures

In a standard high voltage CMOS process a lot of different well combinations are used to build the devices. Because of this, such a process provides a lot of p-n junctions which can be used as photodiodes that conserve as sensing elements of a device.

In order to characterize the different structures and to find suitable structures for certain applications, the different well combinations are evaluated with respect to spectral responsivity as well as dark current.

Before the results of these measurements are presented, the different structures are introduced. The wells used in the different designs in the present work and their acronym used in the labeling of the structures are summarized in Table 2

Table 2: Well label explanation ordered by doping type and doping concentration as well as depth of the junction

Acronym	Explanation
n^+	Very shallow and very highly doped n-well
SN	Shallow n-well, next highest doping level after n^+, deeper than n^+
NW	n-well
DN	Deep n-well, lowly doped, very deep
p^+	Very shallow and very highly doped p-well
SP	Shallow p-well, next highest doping level after p^+, deeper than p^+
PW	p-well
DP	Deep p-well, lowly doped, deeper than p-well but shallower than deep n-well and n-well
Psub	Very lowly doped p-substrate

5.1.1 n-well in p-substrate/p-well structures

To start with the less complex structures, at first, simple n-well structures in a p-doped substrate are presented. The wells used here differ in depth of the junction as well as in doping concentration. As substrate material is lowly p-doped silicon used.

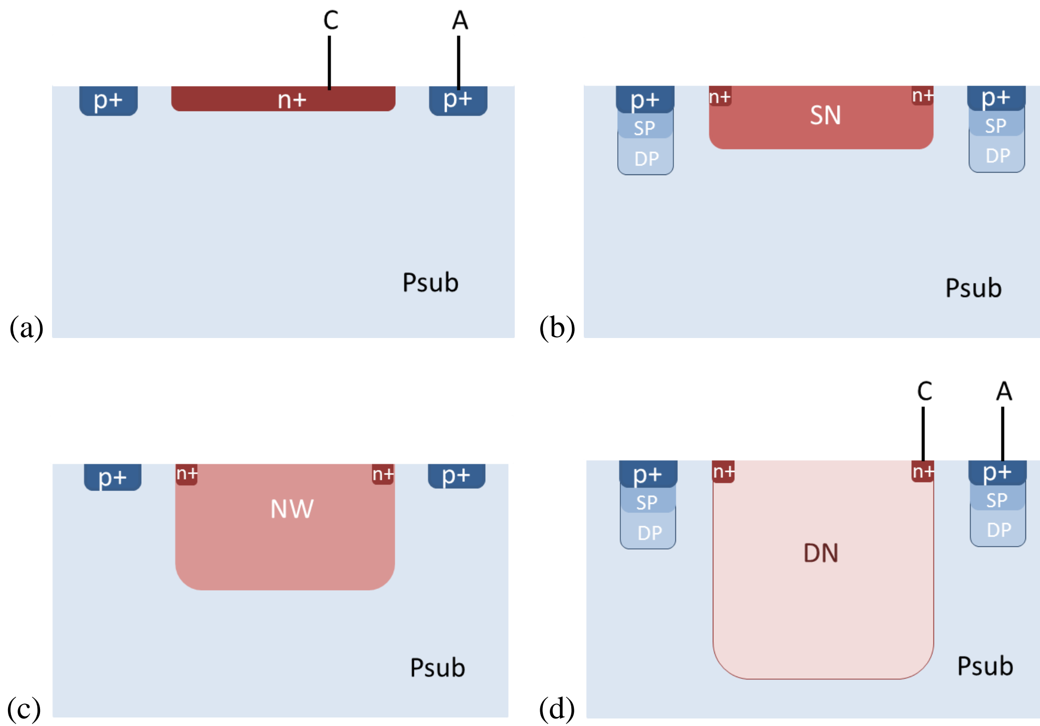

Figure 21: Schematic structure of photodiodes with: (a) shallow and very highly doped n^+-well in lightly p-doped substrate, (b) shallow n-well in lightly doped p-substrate, (c) n-well in lightly p-doped substrate, (d) deep n-well in lightly doped p-substrate. The meaning of the labels of the structures is explained in Table 2

The shading of the n-well structures shown in Figure 21 indicates the doping concentration. The more intense the color, the higher is the doping concentration. The order of the wells with respect to doping concentration, starting with the highest is: n^+/p^+-well, shallow n/p-well, n/p-well, deep n/p-well.

For the electrical contact, an anode and a cathode contact are used as indicated in Figure 21 (a) and (d). For the cathode, a contact with the active area of the photodiode is established by a n^+ region. The anode contact is build-up of a p^+-region in the p-substrate. In the structures including deeper wells a combination of p-regions with decreasing doping concentration is introduced as anode contact.

Also more complex combinations of n-wells have been investigated and are shown in Figure 22.

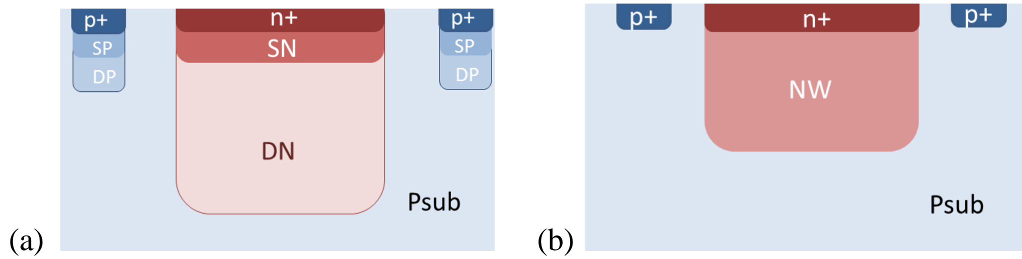

Figure 22: Schematic structure of photodiodes with: (a) n^+-well in shallow n-well in deep n-well in lightly doped p-substrate and (b) n^+-well in n-well in lightly doped p-substrate. The meaning of the labels of the structures is explained in Table 2

What all of the structures, shown in Figure 21 and Figure 22, have in common is that the junction is formed between differently doped n-wells and a lightly doped p-substrate. In these cases just the doping concentration of the n-well is changing and the p-side of the junction is always the same. To show the influence of the low doping concentrations of the substrate also the junction between a highly doped n^+-well and a p-well was studied. The design of this structure can be seen in Figure 23.

Figure 23: Schematic structure of photodiode with a n^+-well in p-well in lightly p-doped substrate. The meaning of the labels of the structures is explained in Table 2

5.1.2 p-well in n-well in p-substrate structures

In the following section even more complex structures will be discussed. The structures, which are shown in Figure 24, consist of two to three well combinations. Differently doped p-wells with varying depth in n-well or deep n-well combinations have been produced.

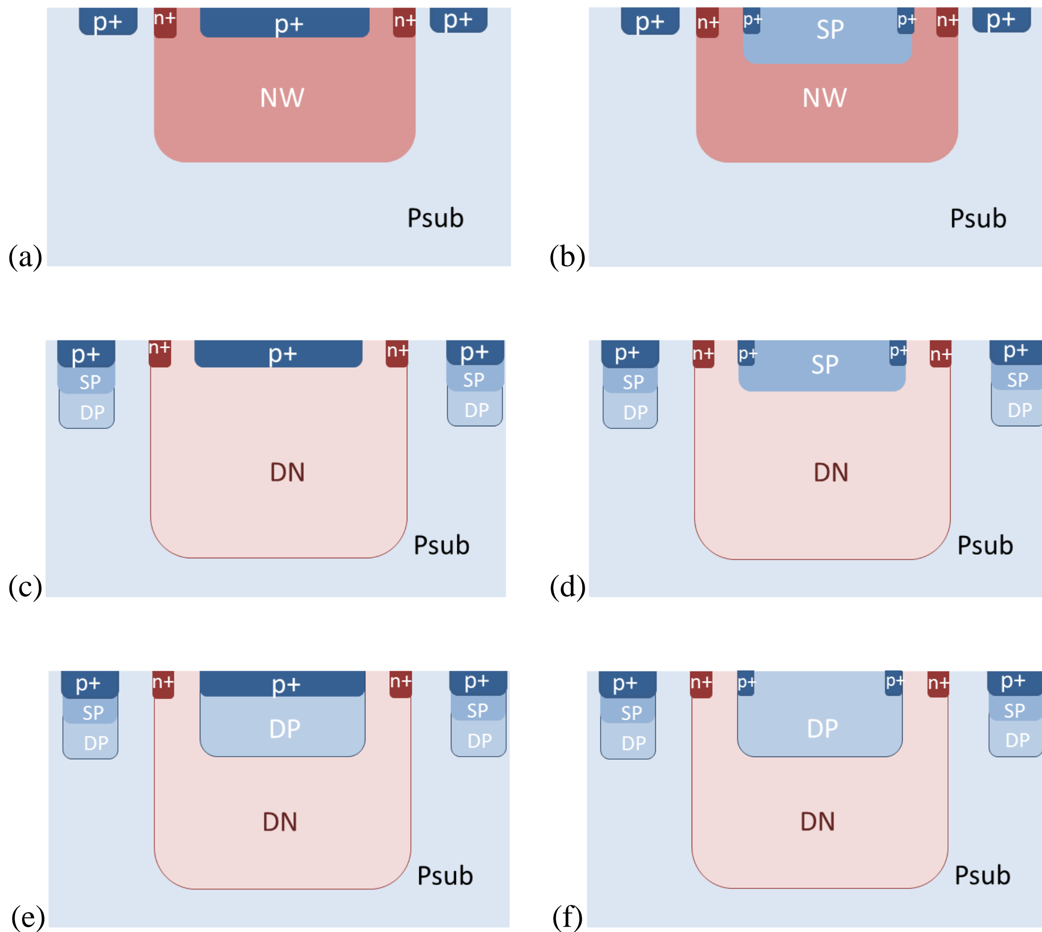

Figure 24: Schematic structure of photodiodes with: (a) very shallow and highly doped p$^+$-well in n-well in lightly doped p-substrate, (b) shallow p-well in n-well in lightly doped p-substrate (c) very shallow and highly doped p$^+$-well in deep n-well in lightly p-doped substrate, (d) shallow p-well in deep n-well in lightly doped p-substrate (e) very shallow and highly doped p$^+$-well in deep p-well in deep n-well in lightly doped p-substrate and (f) deep p-well in deep n-well in lightly doped p-substrate. The meaning of the labels of the structures is explained in Table 2

Looking at the structures in Figure 24, there are two possible junctions in every design, a shallow one including the p-well and the n-well and a deeper one including the n-well and the p-substrate.

Now one has the possibility to set one of these junctions active and to “deactivate” the other one at the same time by shorting certain wells. In Figure 25, it is shown how the different shorting is done.

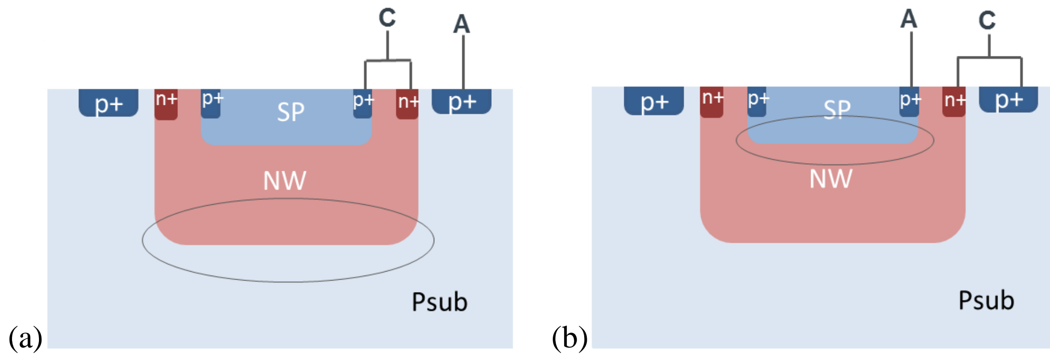

Figure 25: Different shorting modes: (a) activating the deep junction by shorting the p-well and the n-well and (b) activating the shallow junction by shorting the n-well and p-substrate.

By shorting the p-well with the n-well one activates the deep junction between the n-well and the p-substrate. At the same time carriers which are generated in the upper, inactive junction region are forced to recombine. They are also collected but because there is one connection going from the n-side of the junction to the p-side the carriers recombine in this case. Analogously one activates the shallow junction between p-well and n-well by shorting the n-well with the p-substrate; in this case the deep junction is inactive. The resulting effects will be discussed in the following section about responsivity measurements.

In a standard CMOS process a so called field oxide (FOX) is used for isolation. In the standard case the field oxide is formed on the field regions but not on the active regions. [12] Here, the influence of having a field oxide covering also the active region is investigated. In Figure 26 the two different designs are shown.

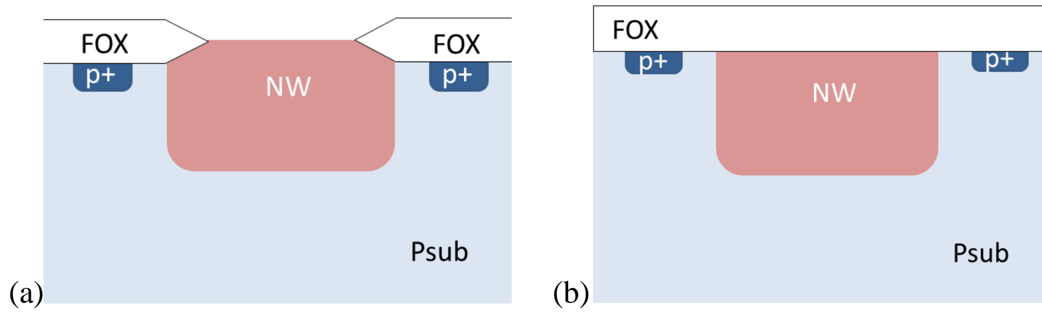

Figure 26: Positioning of field oxide on top of the photodiode structure, (a) active area of photodiode is free of field oxide and (b) field oxide over the whole photodiode

Above the actual photodiode is a stack of metal and oxide layers added. A schematic classical stack built up can be seen in Figure 27. With this stack, also in the case of the field oxide free active area structure (Figure 26 (a)) an oxide will be placed over the whole photodiode called interlevel dielectric. In the upcoming investigations one will see that the difference in stack thickness and the different absorption condition due to the additional field oxide is influencing the responsivity behavior.

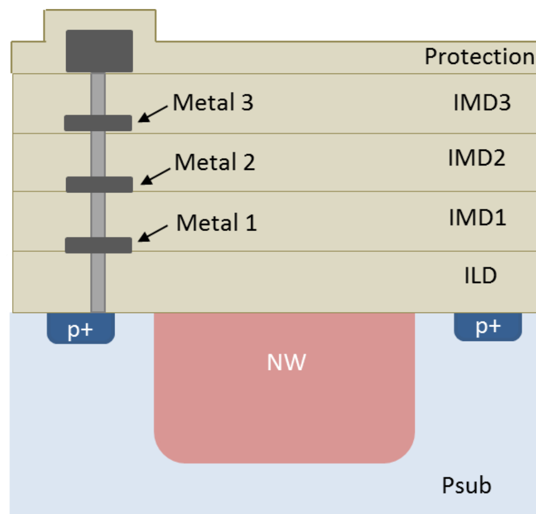

Figure 27: Exemplary built up of a photodiode including consisting of. With an Interlevel dielectric (ILD) several as Intermetal dielectrics (IMD) and a passivation layer for protection [12]

After introducing the different designs, it is useful to summarize the design variations which are of interest and which one should observe with actual measurements as well as with calculations. Using the first set of structures, which are presented in section 5.1.1 (n-well in p-substrate), one-sided junctions are observed. One can evaluate the influence of the depth of the junctions as well as the doping concentration of the more highly doped region. The p-well in n-well structures, beyond that, allows investigating the influence of

higher doping in both regions. The second group of designs introduced in section 5.1.2 provides even more tuning parameters. On the one hand, the depth of the n-well as well as of the p-well are varied, on the other hand, the doping concentrations of both wells in the junction are different for the different designs. Further, one can observe consequences of selecting a junction by different shorting of the well combinations.

Last but not least the effect of different field oxide positions will be discussed. Furthermore the use of an epi-wafer instead of a standard wafer will be investigated. Epi-wafers, which are silicon wafers where an epitaxial grown single crystalline low p-doped silicon layer is on top of a very highly p-doped substrate, are often used as substrate for silicon photodiodes. The advantage of using epi-wafers is that they allow to increase the speed of the photodiode. Just very small bias voltages are enough to deplete the complete epi-layer due to the low doping. Carriers which are generated below the epi-layer and also minority carriers are forced to recombine because of the large amount of recombination centers in the very highly doped p-sbustrate. Thus, the diffusion from this area to the depletion region is reduced resulting in faster photodiodes. [23]

5.2 Spectral responsivity

The first step to compare the different structures is to do spectral responsivity measurements. For the comparison of the different structures the measurements were done with zero bias voltage. The studied wavelength region is 400-900nm, which is the limited by the used light source.

5.2.1 n-well in p-substrate structures

In Figure 29 the responsivity measurements for all n-well structures in the lightly doped p-substrate introduced in section 5.1.1 are shown (exemplary structures are shown in Figure 28).

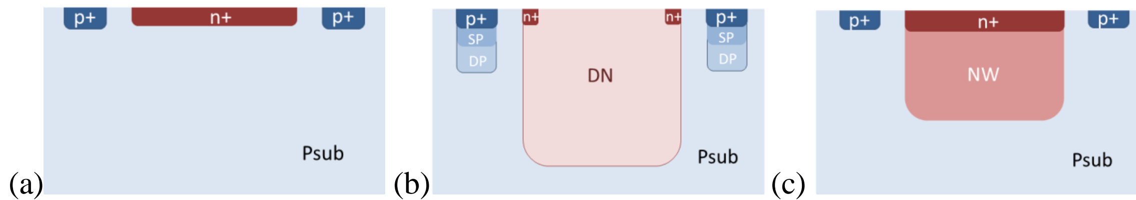

Figure 28: Exemplary one-junction structures with deep active junction used for the dark current measurements shown in Figure 29: (a) n^+-well in p-substrate, (b) deep n-well in p-substrate and (c) n^+-well in n-well in p-substrate.

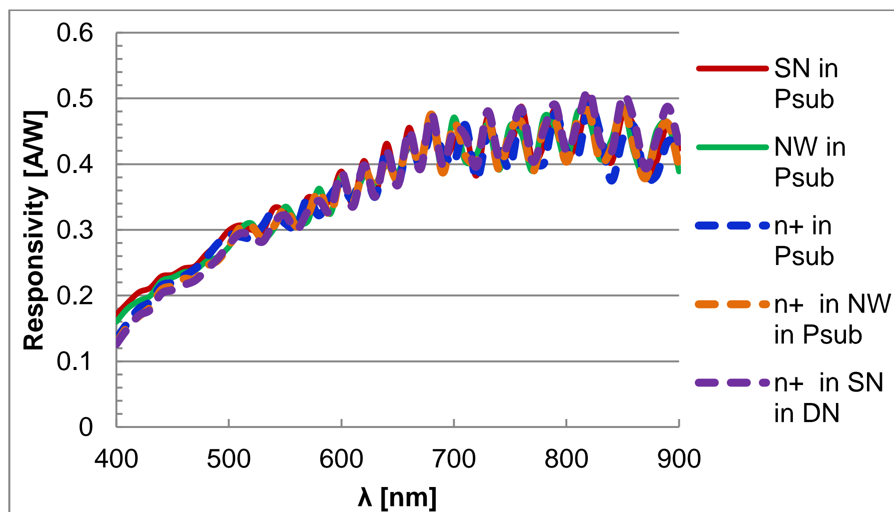

Figure 29: Responsivity as a function of wavelength comparing different n-well structures in p-substrate. Cross sections of the structures are shown in Figure 21.

Looking at the responsivity behavior, an interference pattern can be seen. The amplitude is increasing with increasing wavelength. The interference pattern has its source in the device stack shown in Figure 27. [24]

Comparing the responsivity behavior of the different structures in Figure 29, one can see that there is no significant difference in the spectral responsivity even though the n-wells in the different structures show different doping concentrations. This is surprising as one would expect differences in the responsivity because of the strong dependence of the depletion layer width on the doping concentration as detailed in section 2.

For a first estimation, the depletion layer width is calculated using the abrupt junction approximation with uniform doping introduced in section 2.

$$w_p = \sqrt{\frac{2\varepsilon_r\varepsilon_0}{q}\left(\frac{N_D}{N_A(N_A + N_{D)}}\right)V_{bi}} \tag{5.1}$$

$$w_n = \sqrt{\frac{2\varepsilon_r\varepsilon_0}{q}\left(\frac{N_A}{N_D(N_A + N_{D)}}\right)V_{bi}} \tag{5.2}$$

$$W = \sqrt{\frac{2\varepsilon_r\varepsilon_0}{q}\left(\frac{N_A + N_D}{N_A N_D}\right)V_{bi}} \tag{5.3}$$

Indeed, in this way one finds almost the same values for all the different structures, as shown in Table 3. To further investigate this result, the depletion layer widths in the p-regions and in the n-regions are calculated separately. They are also included in Table 3.

Table 3: Depletion layer width of the p-n junctions for n- in p-structures, V_{bi} is the built in voltage, w_n is the depletion layer width in the n-region, w_p is the depletion layer width in the p-region, and W is the entire depletion layer with

Structure	V_{bi} [V]	w_n [µm]	w_p [µm]	W [µm]
n^+ in Psub	0.803	8.5211E-05	1.217	1.217
SN in Psub	0.684	0.0078	1.120	1.127
NW in Psub	0.726	0.0016	1.156	1.158
DN in Psub	0.643	0.0374	1.070	1.108

These results hint towards a first explanation for the measurement results in Figure 29. Having a big difference in doping concentration between the two regions, the depletion layer is dominant in the lightly doped region and the width of the depletion layer in the more highly doped region is negligibly small. This shows that in these structures we are essentially dealing with a one-sided junction (see section 2).

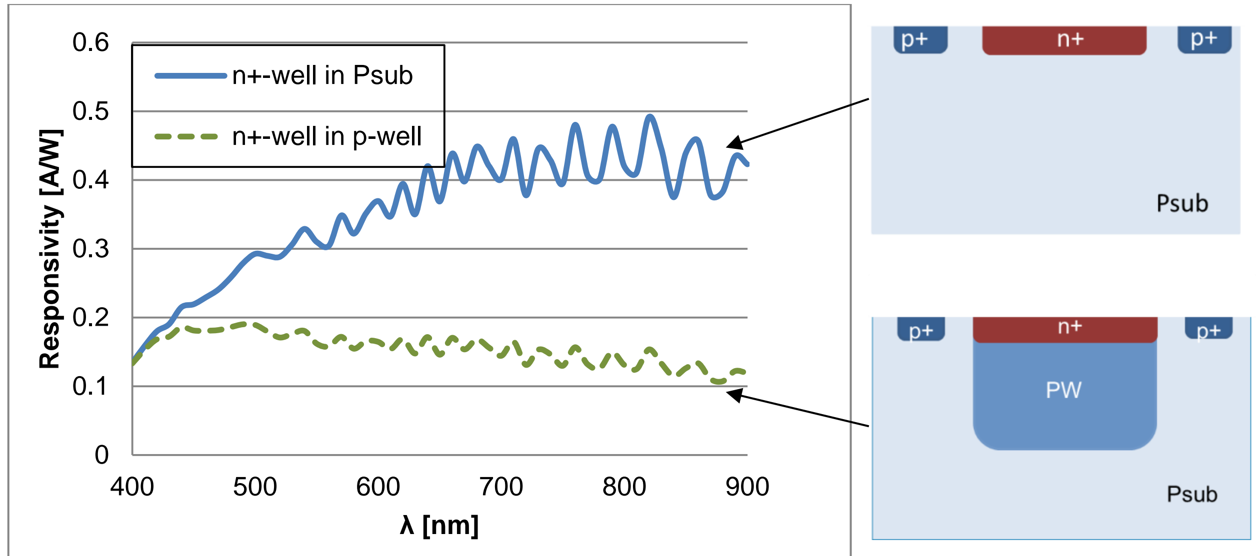

Figure 30: Comparison of responsivity as a function of wavelength between highly doped n^+-well in p-substrate and highly doped n^+-well in p-well

In Figure 30 the influence of the doping concentration of the p-region of the junction on the responsivity is shown. To that aim, the responsivity of the highly doped n^+-well in the very lightly doped p-substrate structure is compared to a junction including a n^+-well and a p-well. In the latter case, the difference in doping concentration between the n^+-well and the p-well is reduced and one no longer deals with of a one sided junction. Still, as the doping concentration in the p-well is lower than in the n^+-well, the width of the depletion region is higher on the p-side, as on the n-side, shown in Table 4.

Table 4: Depletion layer width of p-n junctions for n- in p-structures, V_{bi} is the built in voltage, w_n is the depletion layer width in the n region, w_p is the depletion layer width in the p region and W is the entire depletion layer with

Structure	V_{bi} [V]	w_n [µm]	w_p [µm]	W [µm]
n^+-well in Psub	0.803	8.5211E-05	1.217	1.217
n^+-well in p-well	0.968	0.0022	0.055	0.057

For the n^+-well in p-well structure the responsivity is very low over the whole wavelength range (dashed line in Figure 30). This measurement goes along with the depletion layer width shown in Table 4 and proves the strong dependence of the responsivity on the doping concentration.

An observation in Figure 29 that still needs to be explained is why there is no difference in responsivty for different depths of the junctions. On the one hand using the highly doped n^+-well the junction is very close to the surface and one would expect a high sensitivity at low wavelengths. On the other hand, looking at the deep n-well structure one has a junction several micrometers inside the bulk and the sensitivity at short wavelengths should be reduced and high at long wavelenghts. This is however not observed in the data. An explanation, why this is not the case here, is the long diffusion length in the high quality silicon used in this process as well as the very low doping of the substrate. There are very few recombination centers and so the lifetime and, thus, the diffusion length of the carriers are very large. Thus, there is enough time to also collect the carriers from the diffusion component generated outside the depletion region. This would explain that there is no difference in responsivity in respect to junction depth

The latter scenario is supported by the observation in Figure 29, that there are differences in responsivity for differently doped n-wells in the very short wavelength region. This can be associated with a reduced carrier lifetime for increasing doping concentrations. To show that more clearly, a plot of the short wavelength region of Figure 29 is shown in Figure 31. The structures with the lowest responsivity are the ones which include the very highly doped n^+-well at surface near regions (dashed lines).

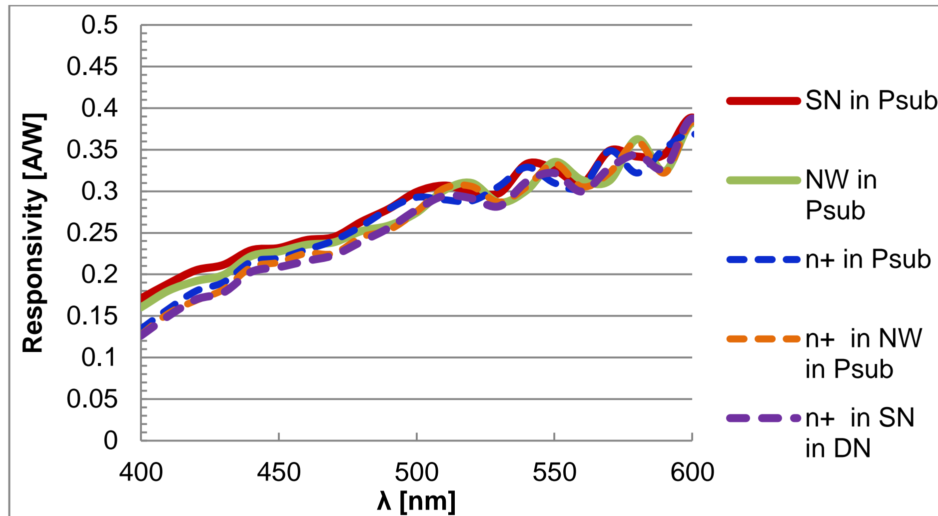

Figure 31: Responsivity as a function of wavelength comparing different n-well structures in p-substrate showing the low wavelength region.

These considerations also suggest a refinement of the explanation for the low responsivity of the n^+-well in the p-well structure, shown in Figure 30. In addition, to the reduced depletion layer width, the higher doping concentration of the p-side of the junction results in a reduced carrier lifetime underneath the junction and, thus, in a decreased contribution of the diffusion from carriers, generated in this region, to the photocurrent.

Another possibility to evaluate the influence of the depletion layer width is to repeat the responsivity measurements with an applied reverse bias voltage. As it is shown in section 2 the depletion layer width increases with increasing reverse bias. In theory the increased depletion layer width should lead to an increase of responsivity because of the enlarged amount of carriers produced inside the space charge region. The results of the corresponding measurements are shown in Figure 32 and Figure 33.

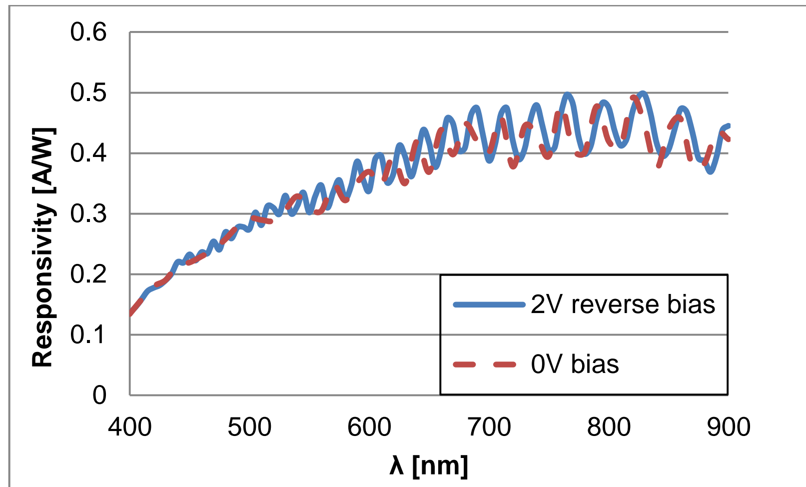

Figure 32: Comparison of responsivity as a function of wavelength between applied reverse bias of 2V and no applied bias for the n$^+$-well in p-substrate structure.

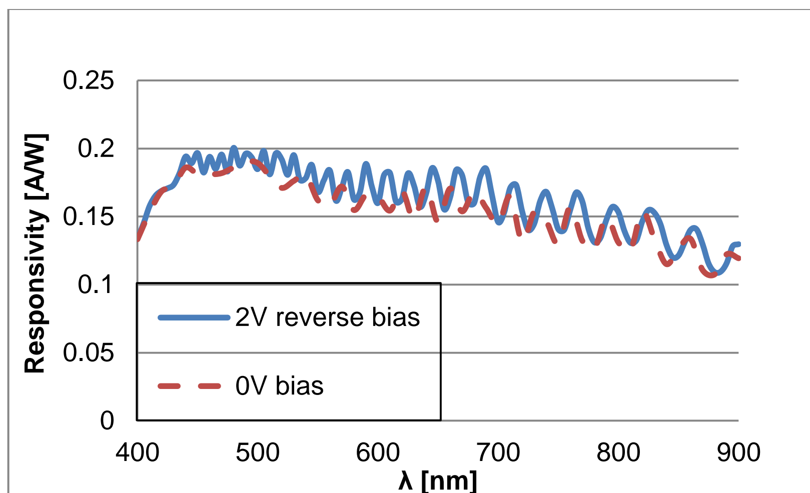

Figure 33: Comparison of responsivity as a function of wavelength between applied reverse bias of 2V and no applied bias for the n$^+$-well in p-well structure.

In Figure 32, where the responsivity of a n$^+$-well in p–substrate structure is shown with and without applied reverse bias, no significant difference between the two measurements can be observed supporting the assessment that in this structure the “diffusion contribution” is very large and the majority of the generated carriers are collected. In contrast, for the n$^+$-well in p-well structure, shown in Figure 33 one can see a slight increase of responsivity with applied reverse bias. This shows that for more highly doped materials the carrier lifetime is decreased and the depletion layer width starts to influence the spectral responsivity.

Influence of field oxide on top of active area

As a next step the role of the field oxide is investigated. The responsivty of the n-well in p-substrate structure with and without field oxide (cross section see Figure 26) are compared in Figure 34.

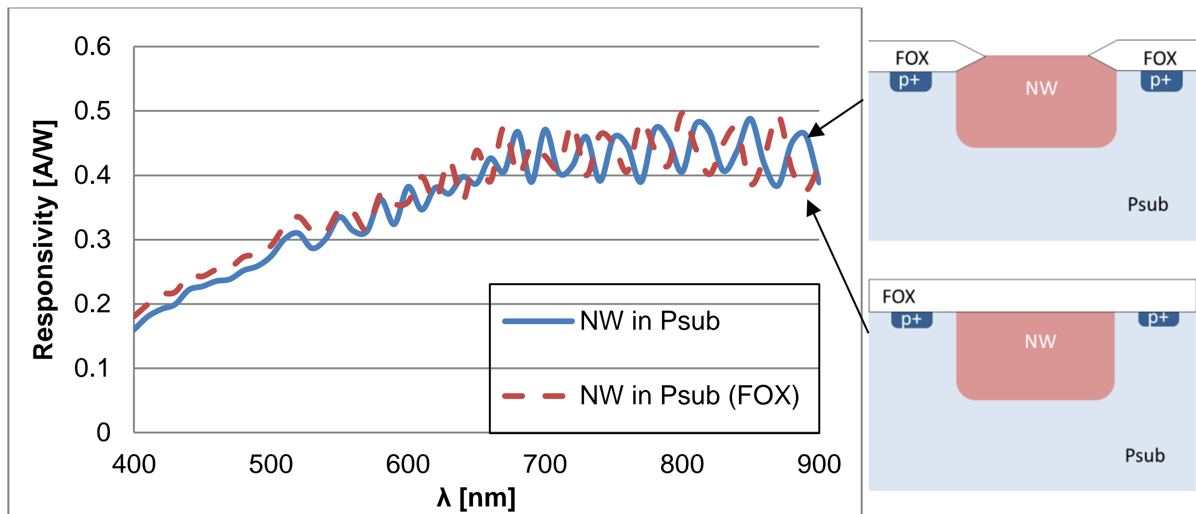

Figure 34: Comparison of responsivity as a function of wavelength between the n-well in p-substrate structure with and without field oxide on top of the photodiode. Structures are shown in Figure 26.

One can see that there is a slight increase of responsivity at low wavelengths when a field oxide is placed on top of the active area of the photodiode (dashed line in Figure 34). One possible explanation for this can be the protection effect of surface near regions of the field oxide from further production steps, which could introduce defects in this region that act as recombination centers. In section 5.2.2 it will be proved that there must be another reason for the increase, which is more significant. As explained in section 5.1, above the photodiode structure an additional stack is placed also including oxides. The different absorption of light in different kinds of oxides could be another explanation for the different responsivities.

Another effect which can be seen having a closer look at Figure 34 is that the interference pattern is shifted. Where there is a minimum for the blue line there is a maximum for the red line. By introducing a field oxide to the photodiode the thickness of the stack (see Figure 27) is changed, this influences the interference condition and leading to the observed change in phase.

5.2.2 p-well in n-well in p-substrate structures

As discussed in 5.1.2 there are two possibilities to short these well combinations. In the following figures different structures with equivalent shorting as well as identical structures with different shorting are compared.

In the beginning, to show the influence of shorting, the responsivity behavior of the two differently shorted shallow p-well in n-well in p-substrate structures, (Figure 35) and also the shallow p-well in deep n-well in p-substrate structures (Figure 36) are compared. One can see very nicely, how one junction is activated while blocking the other one. When activating the shallow junction sensitivity in the short wavelength region is observed while activating the deep junction the responsivity is high in the long wavelength region. Additionally, it is shown how easy one can tune the wavelength sensitivity without varying the design too much. Comparing Figure 35 and Figure 36 it can be seen, that the crossing point of the two characteristics is shifted to longer wavelengths for the deeper n-well.

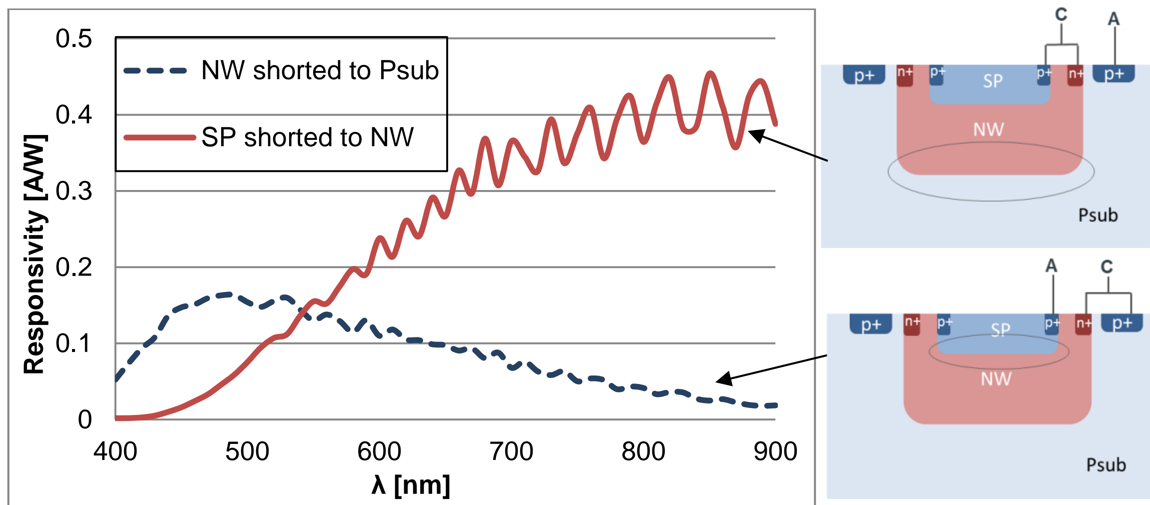

Figure 35: Comparison of responsivity as a function of wavelength of the shallow p-well in n-well in p-substrate structure between the two different shorting modes.

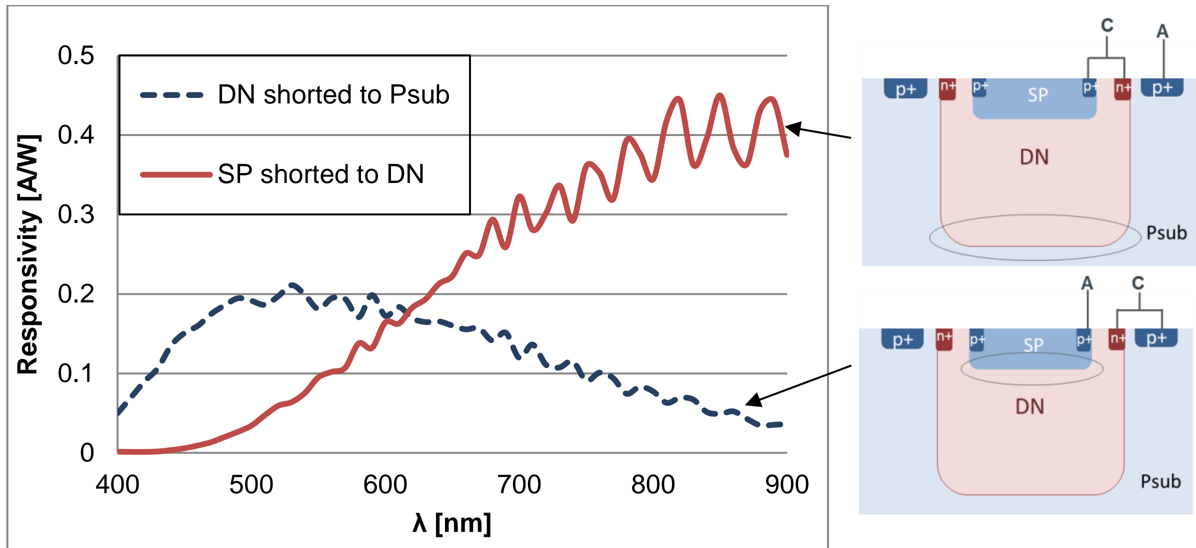

Figure 36: Comparison of responsivity as a function of wavelength of the shallow p-well in deep n-well in p-substrate structure between the two different shorting modes.

To get a better idea what effect the shorting of the wells has on the responsivity behavior, a plot which compares a one-junction structure to a two-junction structure is shown in Figure 37.

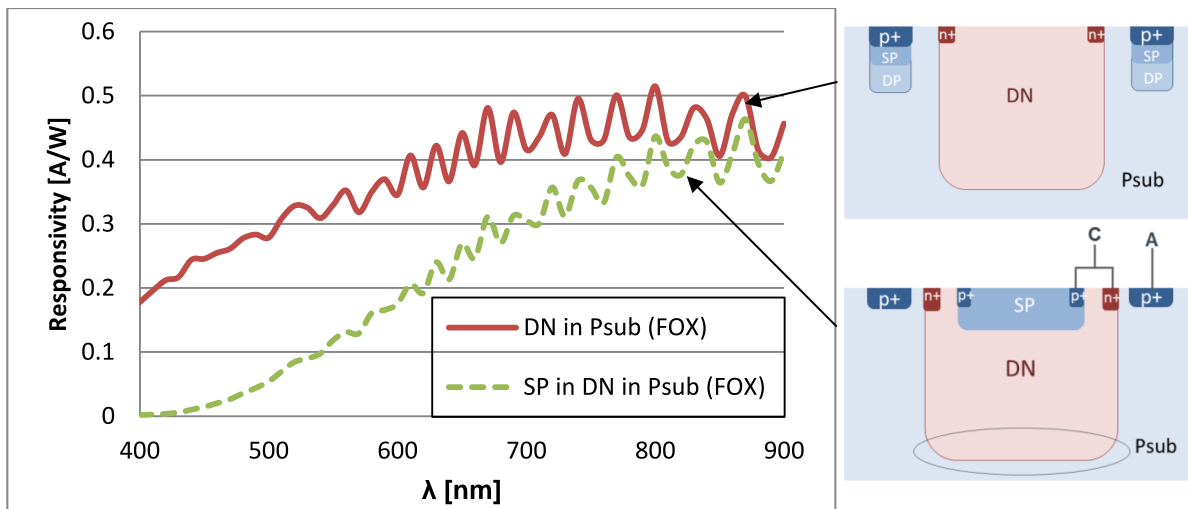

Figure 37: Responsivity as a function of wavelength of the deep n-well in p-substrate junction. The effect of an additional junction on the responsivity is shown.

The deep n-well to p-substrate junction is activated by shorting the shallow p-well to the deep n-well. The same junction is observed in both cases, thus, one can clearly see the effect of introducing a second junction and shorting this junction. One can see in Figure 37 that at short wavelengths the difference between the two curves is very big, but also over the whole range the responsivity for the not shorted single junction is higher. This is

because of the second inactive junction, where all carriers generated are recombined because of the shorting. Like this diffusion from the upper region of the structure is suppressed.

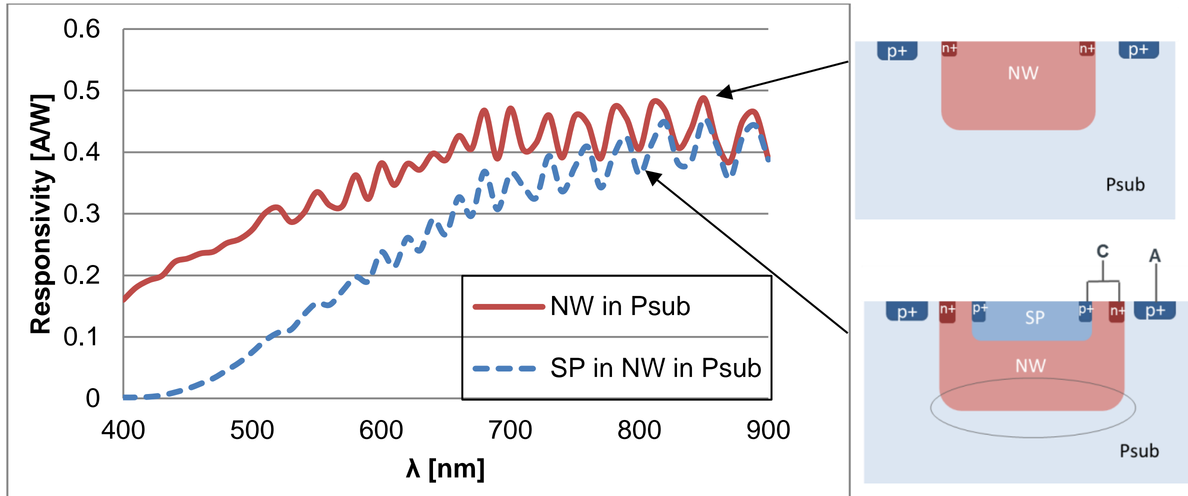

Figure 38: Responsivity as a function of wavelength, showing the effect of well combination to responsivity for a n-well in p-substrate junction. One time with an additional shallow p-well (dashed) and one time without (solid)

In Figure 38 the junction between an n-well and the p-substrate of a one-junction structure (solid line) is compared with a two-junction structure (dashed line) including an additional shallow p-well. The wavelength region where the two designs reach similar responsivites already starts at shorter wavelengths than in Figure 37. This could be due to the shallower position of the n-well compared to the deep n-well. In the case of the n-well, already light with shorter wavelength reaches the space charge region, generating carriers contributing to the photocurrent.

As a last step all designs discussed in section 5.1.2 are compared. The responsivity behavior of the different well combinations with different depths and doping concentrations are presented for the p-well shorted to the n-well in Figure 40. There the active region is the deeper one between the n-well and the lightly doped p-substrate. To recall the investigated structures three of them are exemplary shown in Figure 39.

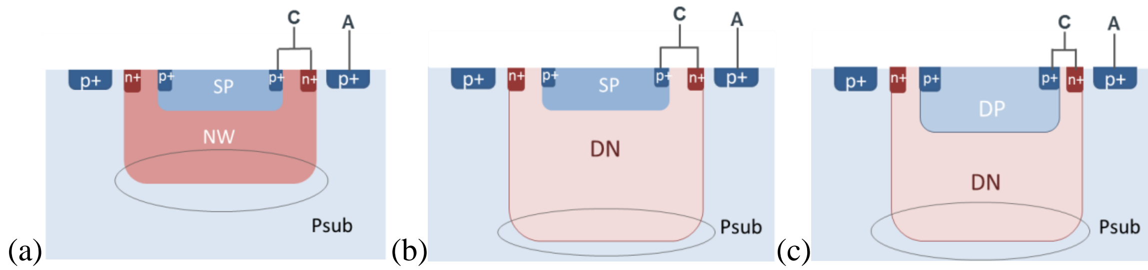

Figure 39: Exemplary structures with deep active junction used for the responsivity measurements shown in Figure 40: (a) Shallow p-well in n-well in p-substrate structure, (b) shallow p-well in deep n-well in p-substrate and (c) deep p-well in deep n-well in p-substrate.

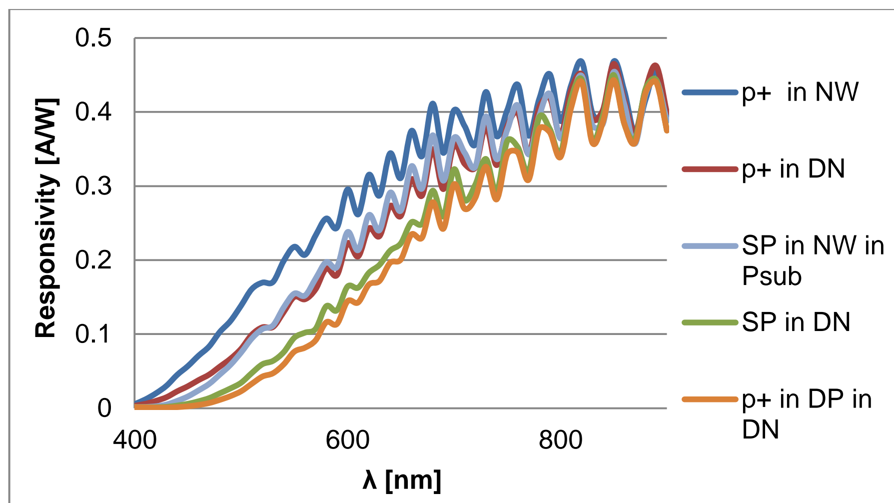

Figure 40: Responsivity as a function of wavelength of the p-well in n-well in p-substrate structures. The p-well is shorted to the n-well. All schematic structures are shown in Figure 24.

In the case of the structures with two junctions significant differences in responsivity can be seen. There are two sources for these differences. First, the position and the width of the depletion layer, and thus, the position of the active junction are of importance. This is explaining the difference in responsivity between the shallow p-well in n-well structure (light blue line in Figure 40 and schematic structure in Figure 39 (a)) and shallow p-well in deep n-well (green line in Figure 40 and schematic structure in Figure 39 (b)). The shallower active junction with the n-well has a shallower space charge region thus collecting carriers generated by light at already lower wavelength. Second the depth of the inactive junction is influencing the responsivity. The structure with the deepest inactive junction (yellow line in Figure 40 and schematic structure in Figure 39 (c)) shows also the lowest responsivity over the longest wavelength region. The bigger distance between the active and the inactive junction, in the shallow p-well in deep n-well structure, in

comparison to deep p-well in deep n-well structure, gives more possibilities to generate carriers in the space between the two junctions, which have then the possibility to diffuse to the space charge region of the active junction, thus, contributing to the photocurrent.
The same two sources are also responsible for the difference in responsivity of the last two structures, where a very shallow p^+-well forms a junction with either an n-well or a deep n-well.

In Figure 42 the same structures as before are shown, but now the n-well is shorted to the p-substrate activating the shallow junction between the p-well and the n-well (exemplary structures are shown in Figure 41). Again a significant difference in spectral responsivity between the different structures can be observed. After calculating the depletion layer width as done in 5.2.1, one can conclude that the bigger the depletion layer width is the higher is the maximum responsivity value. The values of the depletion layer width for the different structures are listed in Table 5.

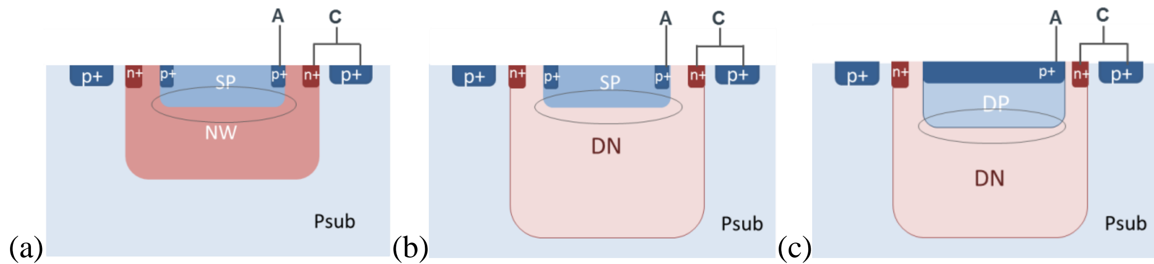

Figure 41: Exemplary structures with shallow active junction used for the responsivity measurements shown in Figure 40: (a) Shallow p-well in n-well in p-substrate structure, (b) shallow p-well in deep n-well in p-substrate and (c) deep p-well in deep n-well in p-substrate.

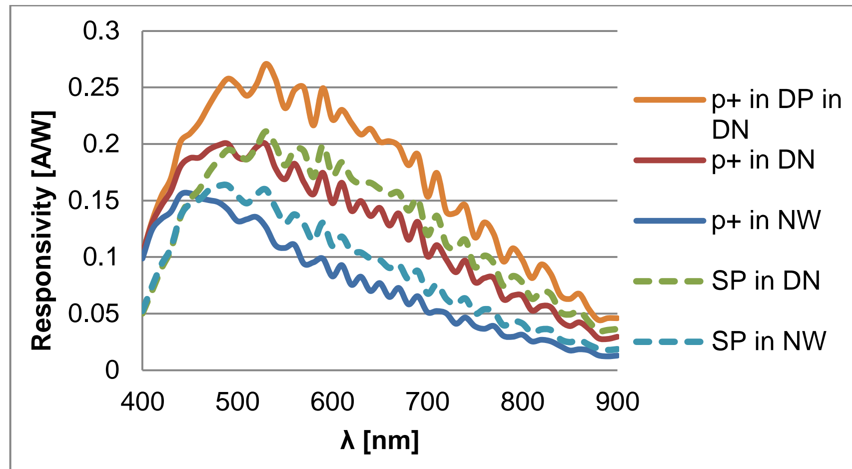

Figure 42: Responsivity as a function of wavelength of the p-well in n-well in p-substrate structures. The n-well is shorted to the p-substrate. Schematic structures are shown in Figure 24.

Table 5: Depletion layer width of p-well in n-well structures with V_{Bi} as the the built in voltage, w_n as the depletion layer width in the n region, w_p as the depletion layer width in the p region and W as the entire depletion layer with

Structure	V_{Bi} [V]	w_n [µm]	w_p [µm]	W [µm]
p^+ in NW	0.973	0.049	0.0024	0.051
SP in NW	0.803	0.093	0.0654	0.159
p^+ in DN	0.890	0.239	0.0005	0.240
SP in DN	0.77	0.204	0.040	0.244
DP in DN	0.758	0.192	0.064	0.255

The position of the responsivity peak also depends on the position of the junction. The p^+-well- in n-well structures (blue and red solid line) have the peak at shorter wavelengths than the shallow p-well in n-well structures (dashed lines), what means the deeper the junction the longer the peak wavelength.

Influence of field oxide

The field oxide dependence was also observed with the two-junction structures and again one can see an increase of responsivity in the low wavelength regions as shown in Figure 43 and Figure 44.

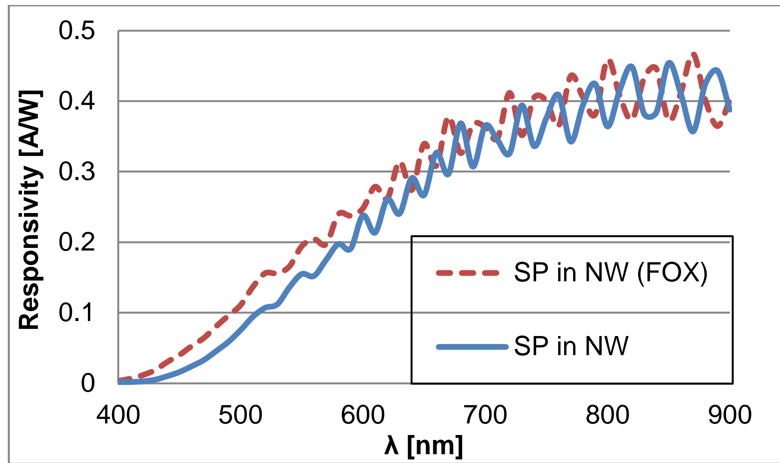

Figure 43: Responsivity as a function of wavelength of the shallow p-well in n-well in p-substrate (p-well shorted to n-well) structure with and without field oxide.

The first statement in the section before was that the increased responisvity is because of fewer defects as a result of the field oxide. Such an explanation cannot hold for the case displayed in Figure 43. As explained before, in this structure the diffusion from upper regions to the depletion layer is suppressed through the shorting of the p-well to the n-well. Nevertheless the increased responsivity is observed. A reduced absorption coefficient in the field oxide especially at short wavelengths, can thus explain at least part of the differences observed in Figure 43 and Figure 44.

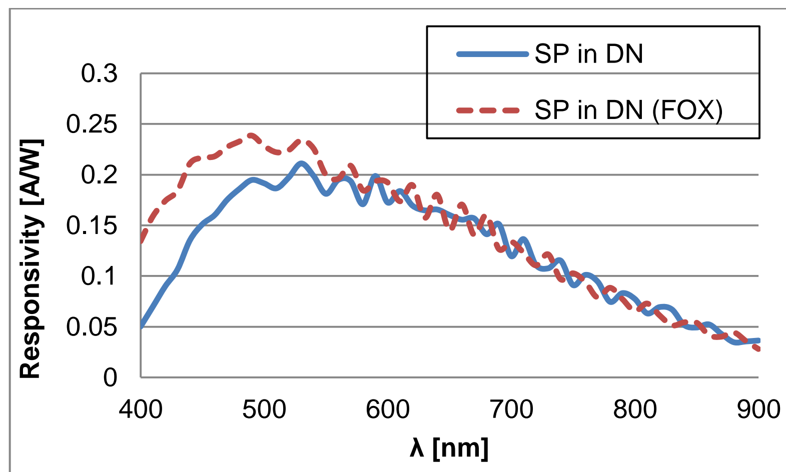

Figure 44: Responsivity as a function of wavelength of the shallow p-well in deep n-well in p-substrate (n-well shorted to p-substrate) structure between with and without field oxide.

As a consequence, especially for applications which require wavelength sensitivity in low wavelength region the use of a field oxide appears advisable.

Influence of epi-wafer

To study the influence of an epi-wafer compared to a standard wafer, the discussed structures are also produced on an epi-wafer.

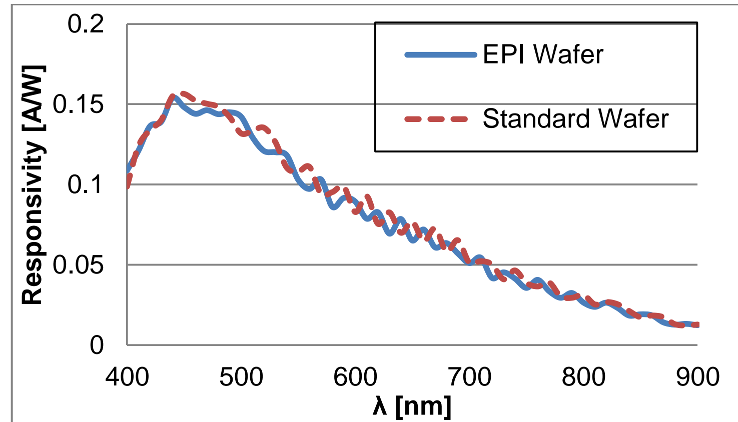

Figure 45: Responsivity as a function of wavelength of the p^+ in n-well in p-substrate (n-well shorted to p-substrate) structure. Use of epi-wafer (solid line) in comparison to standard wafer (dashed line).

In Figure 45 one can see that for structures sensitive at low wavelengths, like the p^+ in n-well structure where the n-well is shorted to the p-substrate, the use of epi-wafers make no difference because the high wavelength region is suppressed anyway and no carriers diffuse from deep regions to the active junction. Looking at structures, which are sensitive in the long wavelength range, the effect of epi-wafers can be seen as shown in Figure 46. At very long wavelengths, the responsivity is lower using an epi-wafer, which supports the assumption that diffusion from very deep areas is stopped.

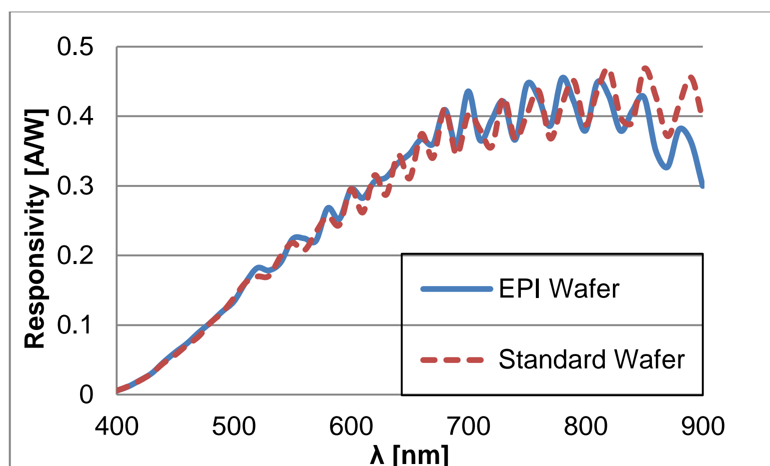

Figure 46: Responsivity as a function of wavelength of the p^+ in n-well in p-substrate (p^+ shorted to n-well) structure. Use of epi-wafer (solid line) in comparison to standard wafer (dashed line).

Using the shorted design and an epi-wafer at the same time suppresses the diffusion component to the photocurrent on both sides of the junction. Outside the space charge region, at low wavelengths, recombination is enforced by the shorting and at very high wavelengths recombination occurs because of the very highly doped p-layer underneath the epi-layer. Therefore, by using epi-wafers the speed of the photodiode can be optimized and at the same time by varying the thickness of the epi-layer the wavelength sensitivity can be tuned.

5.3 Analytical calculations

To further analyze the measurements done in section 5.2, analytical calculations of the depletion layer width, the electrical field, the potential, and the responsivity behavior have been performed. Compared to the theory section in this thesis, where a uniformly doping of the p-n junction has been assumed, in this section the calculations are done using the actual doping profile. One will see that with a Gaussian fit of the doping profiles, the Poisson equation can still be solved analytically.

By using the knowledge on the absorption behavior of light in silicon and the Lambert-Beer's law and taking into account the depletion layer width one can calculate the responsivity as a function of the wavelength. These results will be compared to the actual measurements.

5.3.1 Fit of doping profile

Before one can calculate the desired parameters, a suitable analytical function to approximate the actual doping profile has to be found. To compare the fitted profile, simulated data of the actual doping profile are used. The simulations were done with TCAD (Technology Computer Aided Design) by Jong-Mun Park [25]. Further information of how these simulations are done and implemented is shown in [26]. Looking at the simulated doping profiles the first guess is to use a Gaussian fit of the form

$$N_D = N_{D_0} e^{-\frac{x^2}{\sigma^2}} \tag{5.4}$$

where N_D is the donor doping concentration, N_{D_0} is the starting donor concentration on the surface and x the distance from surface.

Indeed, such a fit turns out to be useful for almost all junction types used in this thesis. The less complex the photodiode structure, the easier it is to find a suitable fit. Because of this, for the first try the deep n-well in p-substrate structure is used. In Figure 47 the doping concentration as a function of the distance from surface as obtained from TCAD simulations is shown. One clearly sees that the assumption of uniform doping does not

apply. The doping concentration of the deep n-well (light green) is shown as well as the doping concentration of the p-substrate (dark blue). Furthermore one can see the net-doping (dashed line) of the well structure.

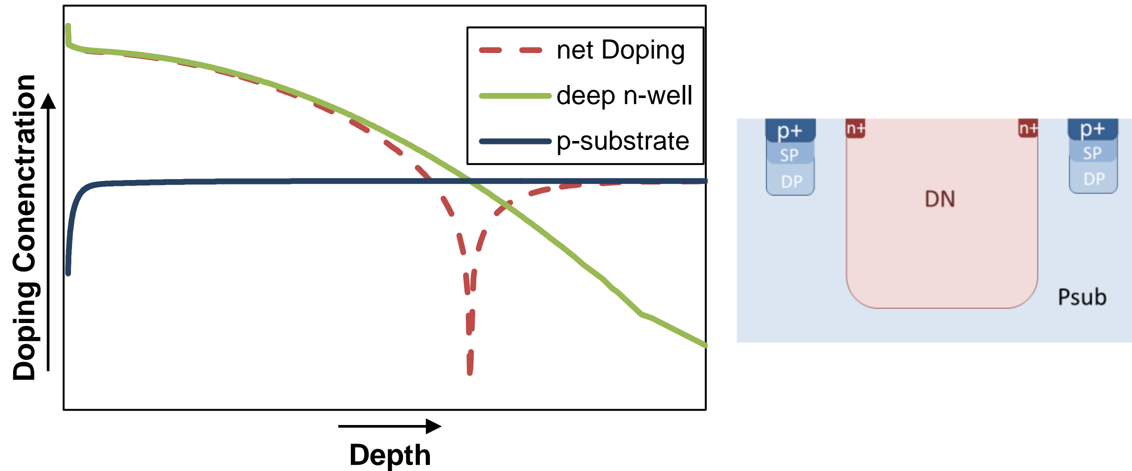

Figure 47: Logarithmic plot of the simulated doping concentration as a function of distance from surface for the deep n-well in p-substrate structure. Dashed red: net doping, green: doping concentration of deep n-well and blue: doping concentration of p-substrate.

To model the actual doping profile a Gaussian fit is used to describe the deep n-well and a constant doping concentration for the p-substrate is assumed. In this way, an excellent agreement between the fit (blue line) and the simulations (green line) is obtained as shown in Figure 47.

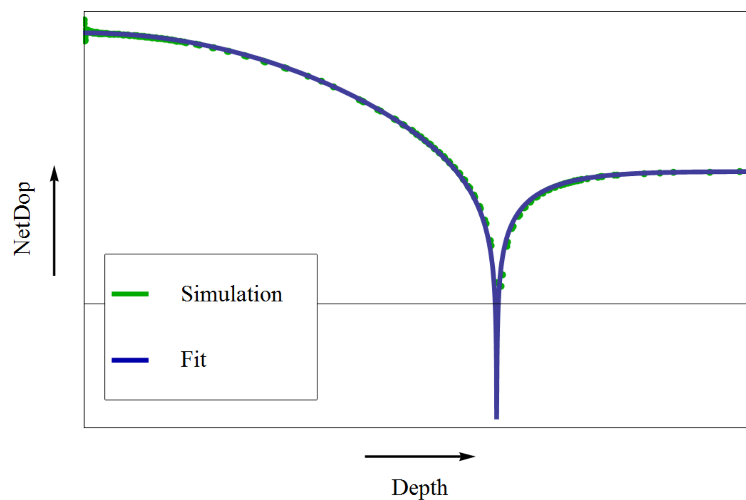

Figure 48: Logarithmic plot of the net-doping concentration as a function of distance from surface of the deep n-well in p-substrate structure. The simulated data are compared to the calculated data out of the fit.

Using shallow wells, the profile does not really show a Gaussian behavior anymore. This also applies to the simulations of the shallow n-well (Figure 49) and of the highly doped n^+-well (Figure 50).

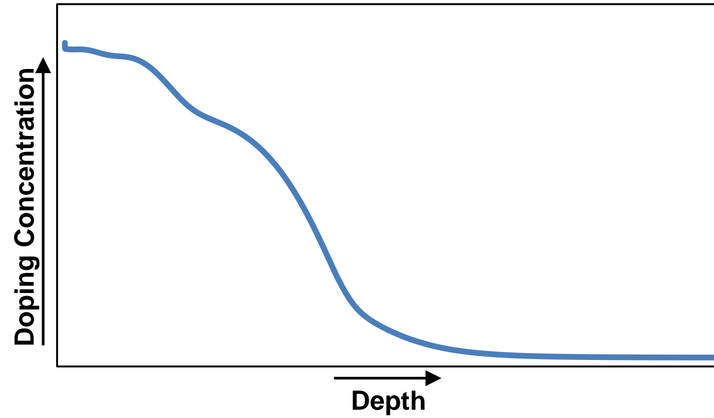

Figure 49: Logarithmic plot of the doping concentration as a function of distance from surface for the shallow n-well. The data is obtained from simulations.

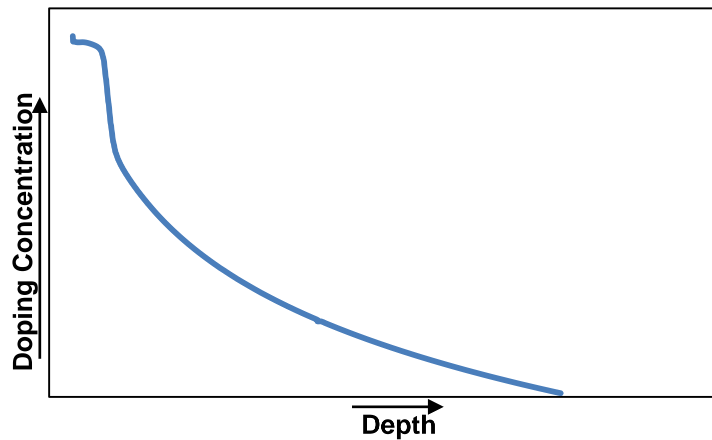

Figure 50: Logarithmic plot of the doping concentration as a function of distance from surface for the n+-well. The data is obtained from simulations.

Nevertheless, taking into account that for the planed calculations only the doping concentration close to the junction is important we attempted to find an adequate Gaussian fit at least for this region. As one can see in Figure 51 and Figure 52, this worked reasonably well.

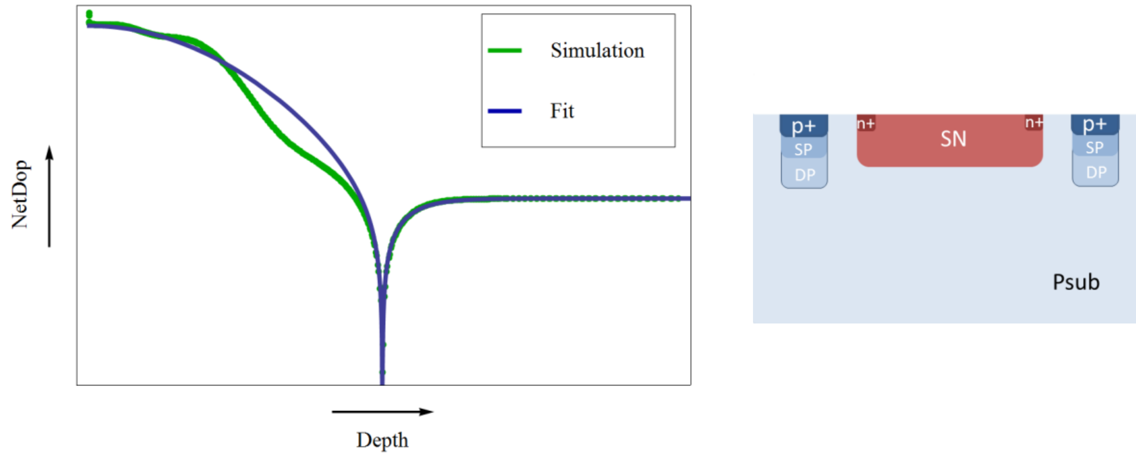

Figure 51: Logarithmic plot of the net-doping concentration as a function of distance from surface of the shallow n-well in p-substrate structure. The simulated data are compared to the calculated data out of the fit.

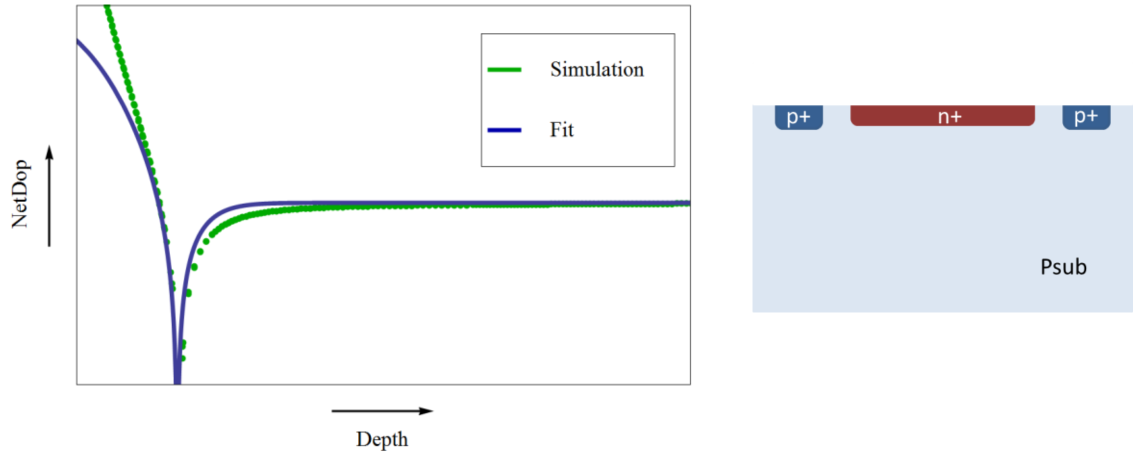

Figure 52: Logarithmic plot of the net-doping concentration as a function of distance from surface of the n^+-well in p-substrate structure. The simulated data are compared to the calculated data out of the fit.

The next step is to find the right fit also for two-junction structures like deep p-wells in deep n-wells and shallow p-wells in deep n-wells. In Figure 53 and Figure 54, respectively, the simulated doping concentration profiles are plotted.

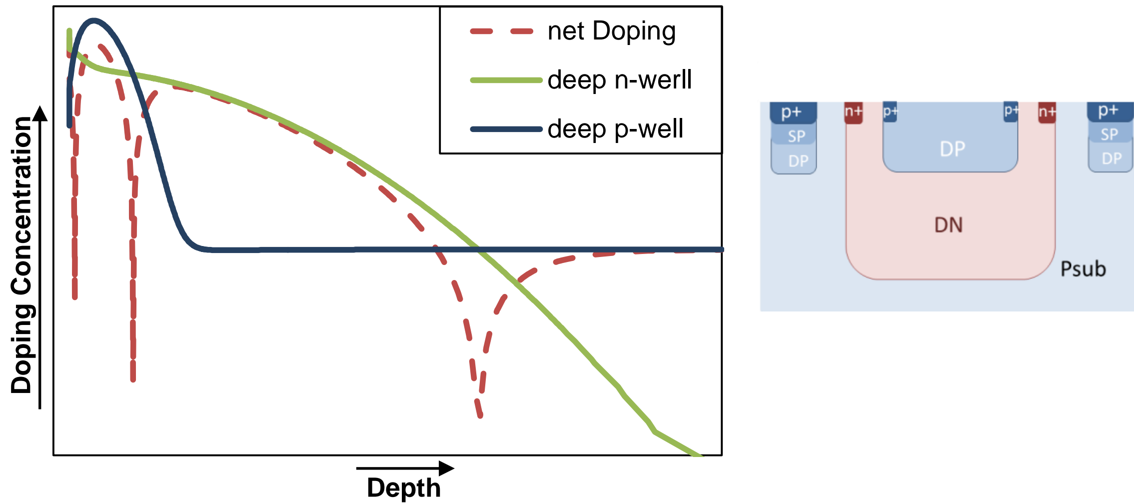

Figure 53: Logarithmic plot of the simulated doping concentration as a function of distance from surface for the deep p-well in deep n-well in p-substrate structure. Dashed red: net doping, green: doping concentration of deep n-well and blue: doping concentration of deep p-well.

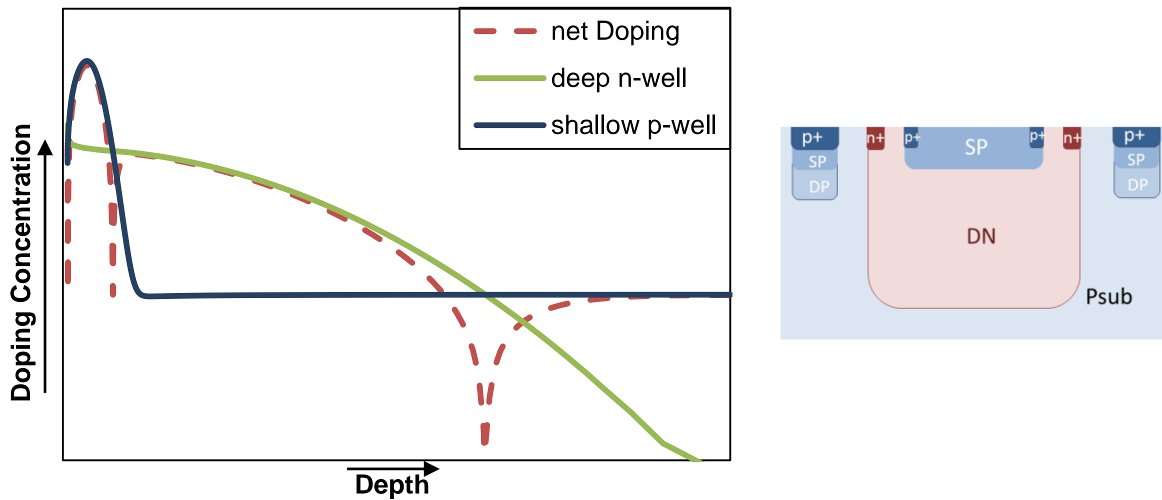

Figure 54: Logarithmic plot of the simulated doping concentration as a function of distance from surface for the shallow p-well in deep n-well in p-substrate structure. Dashed red: net doping, green: doping concentration of deep n-well and blue: doping concentration of shallow p-well.

One can see that the maximum of concentration of the deep p-well (dark blue line in Figure 53) as well as of the shallow p-well (dark blue line in Figure 54) is not on the surface but deeper in the material. With that knowledge the equation for the fit has to be changed slightly compared to equation (5.4). It now reads:

$$N_D = N_{D_0} e^{-\frac{(x-x_0)^2}{\sigma^2}} \tag{5.5}$$

x_0 is defined as the distance from surface with maximum doping concentration. This small variation is enough to reach again very good fits for the more complex structures as shown in Figure 55 and Figure 56.

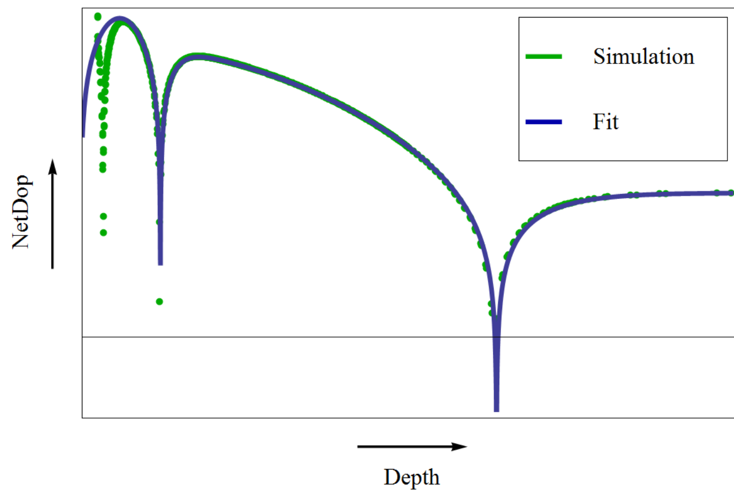

Figure 55: Logarithmic plot of the net-doping concentration as a function of distance from surface of the deep p-well in deep n-well in p-substrate structure. The simulated data are compared to the calculated data out of the fit.

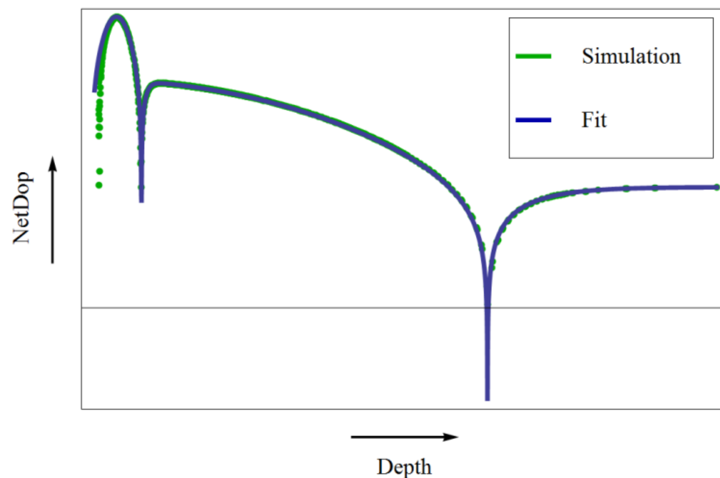

Figure 56: Logarithmic plot of the net-doping concentration as a function of distance from surface of the shallow p-well in deep n-well in p-substrate. The simulated data are compared to the calculated data out of the fit.

Again it is difficult to find a suitable fit for the structures with a well combination including the p^+-well for the whole depth range. The doping profile of the p^+-well is very similar to that of the n^+-well and one has the same problems as mentioned before. But also for these structures, in the important region, the final fit agrees well with the simulated doping profiles (see Figure 57).

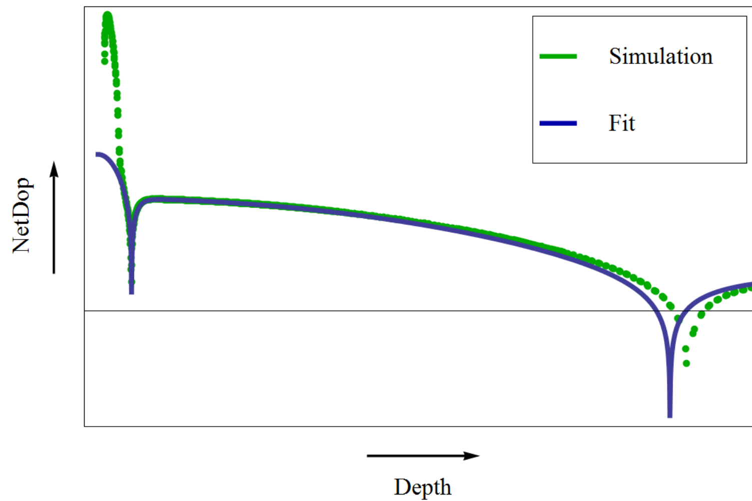

Figure 57: Logarithmic plot of the net-doping concentration as a function of distance from surface of the p^+-well in deep n-well in p-substrate structure. The simulated data are compared to the calculated data out of the fit.

The only structure for which no satisfying profile can be achieved is the n^+-well in p-well structure. Both wells, the p- as well as the very shallow n^+-well, are not following a Gaussian profile and, as one can see in Figure 58 the resulting fit does not agree with the simulations very well.

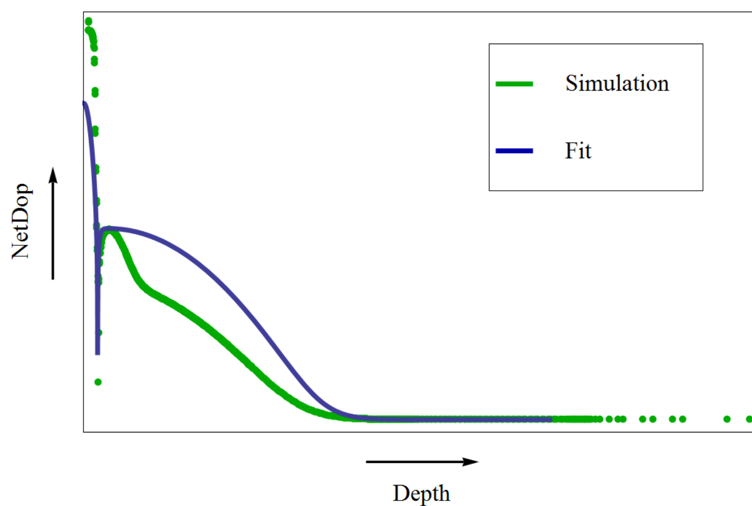

Figure 58: Logarithmic plot of the net-doping concentration as a function of distance from surface of the n^+-well in p-well in p-substrate structure. The simulated data are compared to the calculated data out of the fit.

5.3.2 Calculation of parameters

Using the fits described in 5.3.1 the depletion layer width, the electric field and the built-in voltage are calculated in analogy to the way described in section 2 using the Poisson equation. The results for the depletion layer width, the built in voltage and the electric field are shown in Table 6. They show clearly, how the parameters are dependent on the doping concentration. The higher the doping concentration the smaller the depletion layer width. The built-in voltage and the electric field are increasing with increasing doping concentration.

Table 6: Calculated values of depletion layer width in µm, built in voltage in V and electric field in V/cm for different well structures using Gaussian doping profile

Structure	Depletion layer width [µm]	Built in voltage [V]	Electric field [V/cm]
DN in Psub	1.80	0.572	4818.48
NW in Psub	1.42	0.600	6620.92
SN in Psub	1.28	0.615	7820.79
n^+ in Psub	1.20	0.628	9170.72
n^+ in PW	0.09	0.894	153747
DP in DN	0.42	0.734	-26616.4
SP in DN	0.29	0.775	-41713.1
SP in NW	0.24	0.792	-50075.3
p^+ in DN	0.28	0.778	-43399.2
p^+ in NW	0.18	0.825	-71378.3

In the following, the net-doping, the space charge distribution, the electric field distribution, the potential and the band diagram are illustrated for some exemplary structures. The schematic cross sections of the structures are shown in Figure 59, Figure 61 and Figure 63 respectively.

Figure 59Schematic cross section of the n+ in p-substrate structure

Figure 60: Calculated parameters as a function of distance from the surface for the deep n-well in p-substrate structure (see Figure 59); (a) net doping, (b) net doping with doping type, (c) band diagram, (d) space charge, (d) electric field and (e) potential.

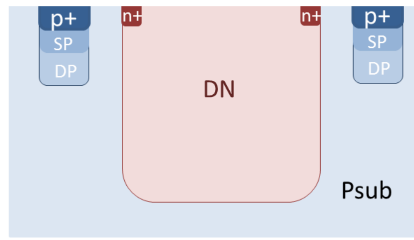

Figure 61: Schematic cross section of the deep n-well in p-substrate structure

Figure 62: Calculated parameters as a function of distance from the surface for the n⁺-well in p-substrate structure (see Figure 61); (a) net doping, (b) net doping with doping type, (c) band diagram, (d) space charge, (d) electric field and (e) potential.

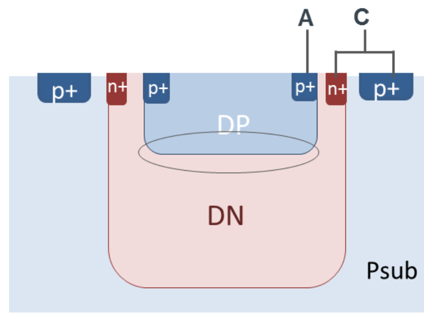

Figure 63: Schematic cross section of the deep p-well in deep n-well in p-substrate (n-well shorted to p-well) structure.

Figure 64: Calculated parameters as a function of distance from the surface for the deep p-well in deep n-well in p-substrate structure (see Figure 63); (a) net doping, (b) net doping with doping type, (c) band diagram, (d) space charge, (d) electric field and (e) potential.

5.3.3 Calculated responsivty behavior

With the knowledge of the absorption behavior of light and the generation of carriers in silicon one can also analytically calculate the responsivity behavior. To calculate the responsivity of a photodiode we start with calculating the photocurrent in the depletion region and this is done by using the generation rate introduced in section 2.2. Integrating the generation rate in a dedicated depth interval in Silicon leads to the photocurrent density generated in this junction. Setting as boundaries the depletion layer boundaries, the result corresponds to the dynamic responsivity of the junction. In a finite volume, the carriers contributing to the photocurrent must be the same as the carriers generated through the incident irradiance (see section 2.2.1). Furthermore the electron-hole pair generation in a finite volume must be the same as the absorbed irradiance at the borders of the unit volume or in this case the borders of the depletion region z2 and z1 (z2=z1+dz). In the case of homogenous irradiance all carriers flow perpendicular to A along the z-axis leading to a current density which is proportional to the carrier generation. Now by taking the difference of irradiance at the one side of the depletion region and the other side I get a value for the photocurrent in this region. This way the calculation of the responsivity is even easier than integrating over the electron-hole generation rate. [27]

As last step in this section this was done. The calculated responsivites can then be compared to the measured ones (see Figure 65 and Figure 66).
One serious approximation in the following calculations is that just the drift component of the photocurrent is observed and the diffusion component is neglected. This is done because it is numerically demanding to include it and it would be beyond the scope of this thesis. This is a particularly problematic simplification when describing these structures, because of the strong influence of the diffusion component as proved in section 5.2.1. This mismatch can be seen in Figure 65. The calculated data show a peak of the responsivity behavior, while the measured one is increasing steadily with increasing wavelength. The diffusion component blurred the peak in the measurements. Still, one will see that for the structures where diffusion is suppressed this approximation brings sufficient results.

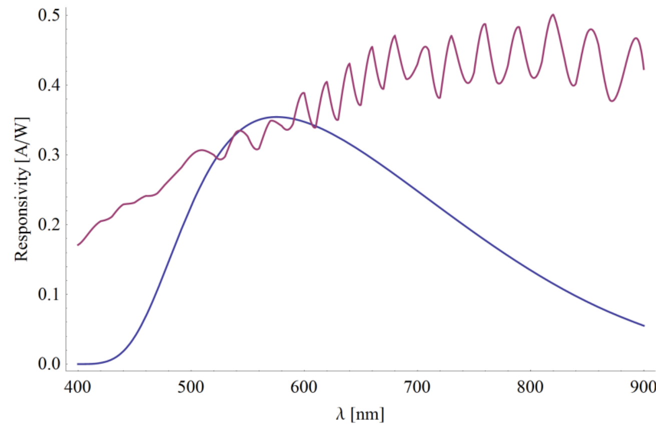

Figure 65: Responsivity as a function of wavelength for the shallow n-well in p-substrate structure. The measured responsivity values (purple) and the calculated values (blue) are compared.

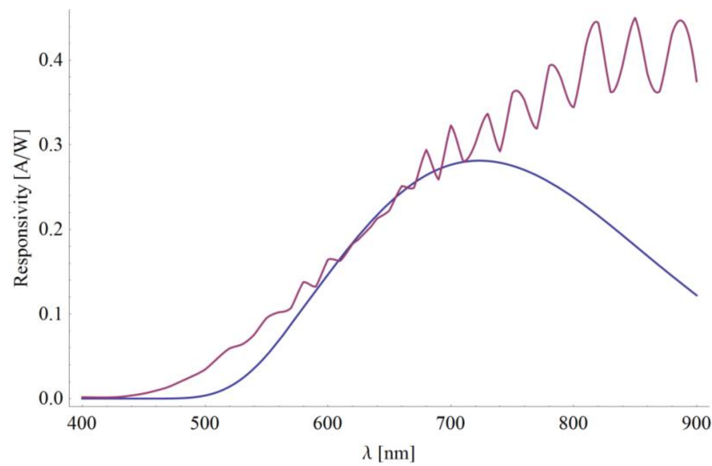

Figure 66: Responsivity as a function of wavelength of the deep p-well in deep-n-well (p-well shorted to n-well) structure. The measured responsivity values (purple) and the calculated values (blue) are compared.

In Figure 66 the effect of shorting is shown. The calculated responsivity curve of the deep n-well in p-substrate structure is compared with the measured one of the deep n-well in p-substrate structure with an additional junction formed by the deep p-well and the deep n-well. As explained before, by shorting the shallow junction, diffusion out of this region is suppressed. One can see that by suppressing the diffusion from one side of the junction the measured and calculated curves agree better. Just the diffusion from the substrate side of the junction can still be seen leading to an increase of the measured responsivity, above about 750 nm.

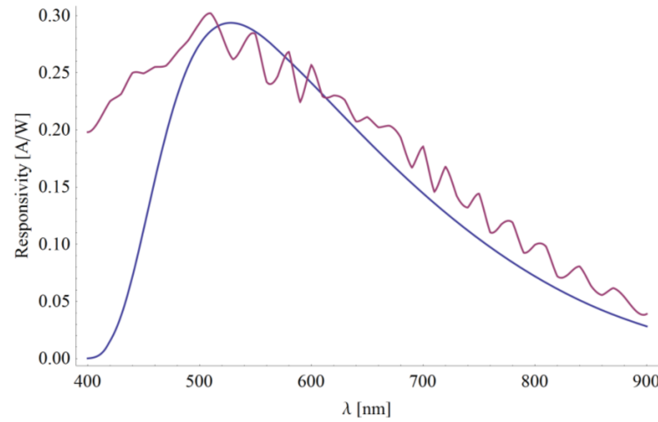

Figure 67: Responsivity as a function of wavelength of the deep p-well in deep n-well in p-substrate (n-well shorted to p-substrate) structure. The measured responsivity values (purple) and the calculated values (blue) are compared.

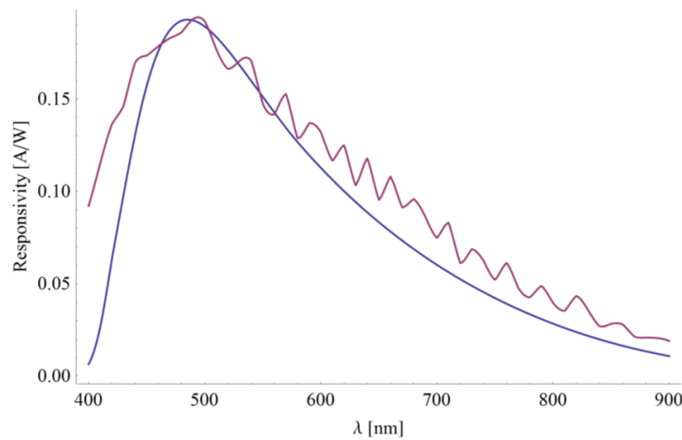

Figure 68: Responsivity as a function of wavelength of the shallow p-well in deep n-well in p-substrate (n-well shorted to p-substrate) structure. The measured responsivity values (purple) and the calculated values (blue) are compared.

In Figure 67 and Figure 68, structures with active shallow junction are shown. In this case the diffusion coming from the substrate is suppressed by shorting the n-well to the p-substrate. One can see that the measured curves fit very well to the calculated ones and just in the very low wavelength region a deviation can be seen resulting from diffusion of carriers above the active junction to the depletion region, thus, contributing to the photocurrent.

Concluding one can say that a strong deviation between simulations and experiments are observed whenever there is a strong diffusion contribution to the photocurrent. A good match is observed when diffusion is suppressed by shorting or high doping even when using Gaussian fits.

5.4 Dark current

For an even better understanding of the structures also the dark current was measured. As mentioned above in section 2, the dark current is a very important parameter limiting the detection minimum.

The measurements have been done at two temperatures. The first series of measurements were done at room temperature, but due to the very low dark currents of the investigated structures, the measurements at this low temperature showed a very low signal. Therefore, to prove the validity of the observed trends the measurements were repeated at 60°C.

For the measurement the voltage of the cathode relative to anode was swept from -1 to 6 V in the case of n- in p-structures and from -6 to 1 V for p- in n-structures. In the following plots the reverse bias region is shown because this is the one interesting for the dark current.

5.4.1 n-well in p-substrate/p-well Structures

First of all the dark current measurements were done for one-junction structures. Exemplary structures are shown in Figure 69: Exemplary one-junction structures with deep active junction used for the dark current measurements shown in Figure 70: (a) n^+-well in p-substrate structure, (b) deep n-well in p-substrate and (c) n^+-well in p-well structure.Figure 69.

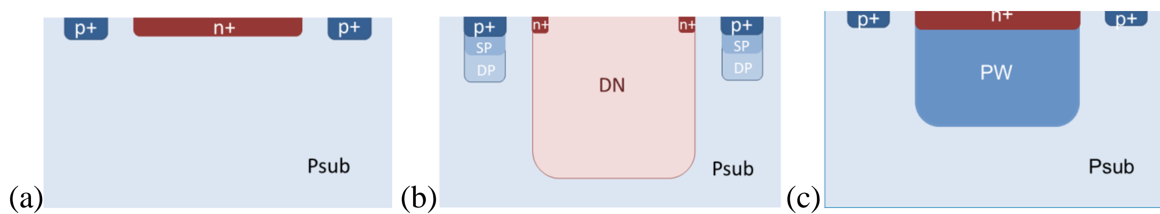

Figure 69: Exemplary one-junction structures with deep active junction used for the dark current measurements shown in Figure 70: (a) n^+-well in p-substrate structure, (b) deep n-well in p-substrate and (c) n^+-well in p-well structure.

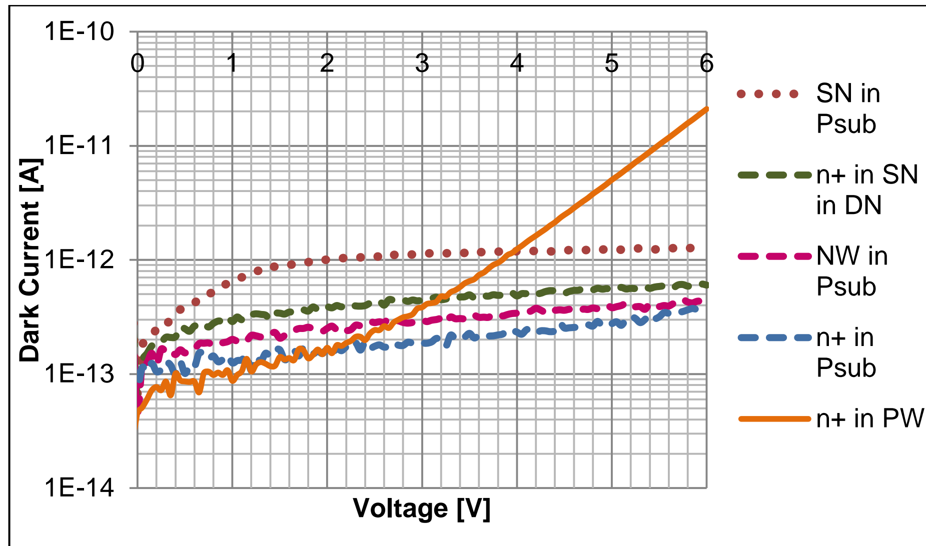

Figure 70: Dark current of the n-well in p-substrate structures as a function of voltage @ 25°C.

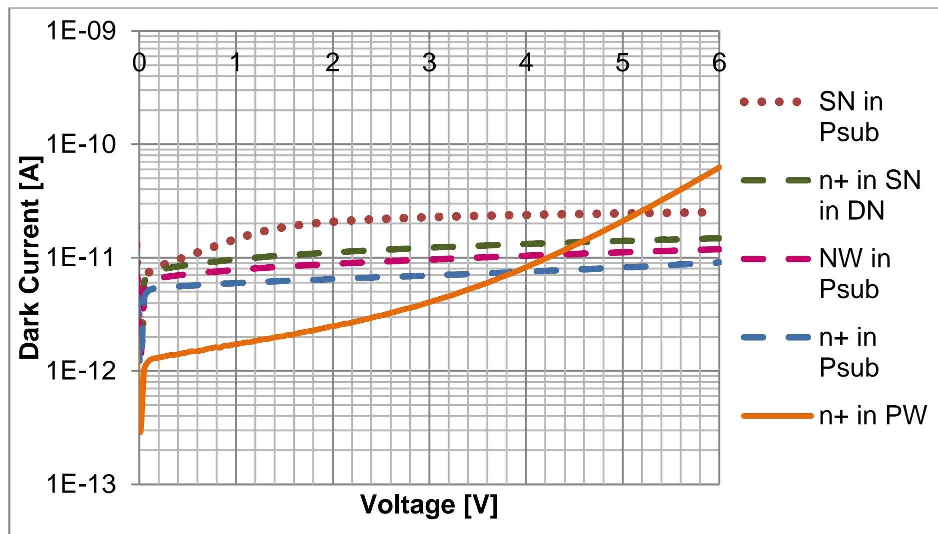

Figure 71: Dark current of the n-well in p-substrate structures as a function of voltage @ 60°C.

In Figure 70 and Figure 71, one can see the dependence of the dark current on the temperature very well. By doubling the temperature the dark current increases by more than one order of magnitude. Furthermore, one can see that measuring at 25°C the current values are that low that the detection limit of the set-up is almost reached.

The expected trend of dark current is that the dark current increases with decreasing doping concentration as shown in section 2.2.3. The shallow n-well in p-substrate structure, the n-well in p-substrate structure and the n^+-well in p-substrate structure (dashed lines) follow this trend.

The shallow n-well in p-substrate structure (points) is not behaving as expected. The doping concentration is higher than the one of the deep n-well and the n-well. Thus, the values should be between the n-well in p-substrate structure and the structure including the n^+-well. As it can be seen in Figure 70 and Figure 71 the structure shows a higher dark current than expected. A possible reason for that behavior could be found in the doping profile that cannot be fitted by a Gaussian profile as discussed in section 5.3.1.

Only the dark current for the n^+-well in p-well structure (yellow solid line) differs qualitatively from the others. It steadily increases with increasing voltage and no saturation is reached. The reason for this behavior is the very narrow depletion layer region of this structure as shown by the calculations in section 5.3.2. As discussed in [28], for such structures the diffusion and generation term is not enough anymore to describe the dark current. In fact, the small depletion layer width leads to short tunneling distances, giving rise especially to band-to-band tunneling. This results in the (super)exponential increase of the dark current with increasing reverse bias. [28]

Influence of field oxide on top of active area

Because of the effect of the field oxide on the responsivity measurements, also the dark current measurements of structures with and without field oxide are compared to each other.

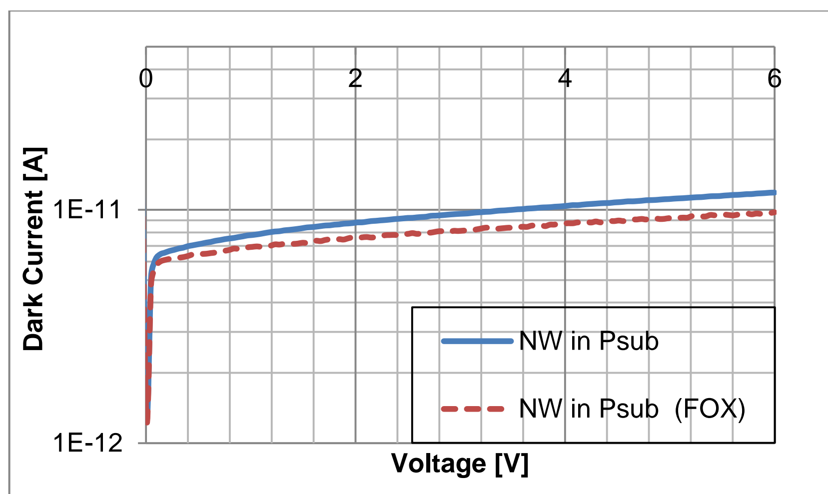

Figure 72: Comparison of the dark currenta for the n-well in p-substrate structure as a function of voltage between designs with (dashed line) and without (solid line) field oxide.

As shown in Figure 72 a somewhat decreased dark current is observed, when using a field oxide on top of the active area (dashed line). A reason for the improved dark current could be a reduced density of generation centers because of fewer defects on the surface due to the field oxide. But not all structures show this difference in dark current with and without field oxide. The shallow n-well in p-substrate structure in Figure 73 for example shows just a very small, quite insignificant difference in dark current.

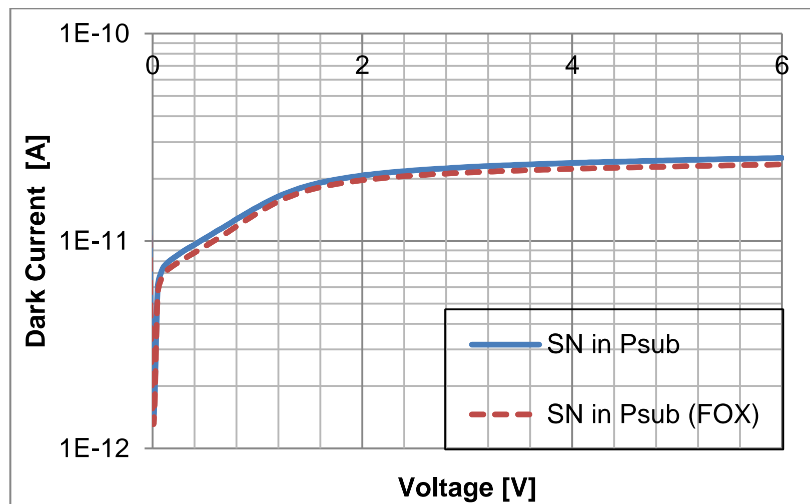

Figure 73: Comparison of the dark currenta for the shallow n-well in p substrate as a function of voltage between designs with (dashed line) and without (solid line) field oxide.

5.4.2 p-well in n-well in p-substrate structures

Following this, the dark currents for the two-junction structures are compared. In the case of Figure 75, the active junction is between the n-well and the p-substrate (exemplary structures in Figure 74).

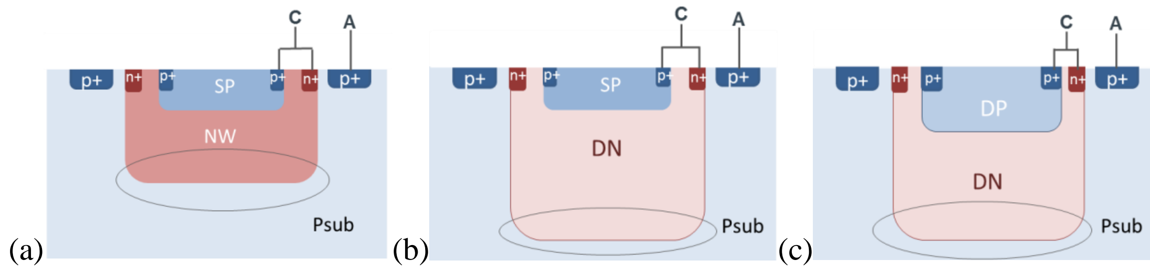

Figure 74: Exemplary structures with deep active junction used for the dark current measurements shown in Figure 40: (a) Shallow p-well in n-well in p-substrate structure, (b) shallow p-well in deep n-well in p-substrate and (c) deep p-well in deep n-well in p-substrate.

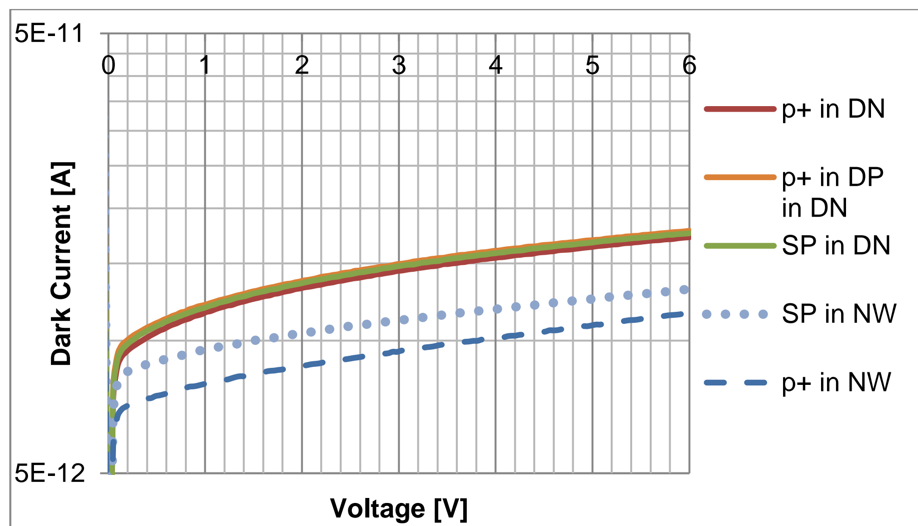

Figure 75: Dark current for the p-well in n-well structures (p-well shorted to n-well) as a function of voltage @ 60°C.

One can see that all structures show a similar trend regarding saturation. The expected behavior that with decreasing doping concentration the dark current is increasing is fulfilled. All structures where the junction is formed between a deep n-well and the p-substrate (solid lines) show almost the same dark currents. The difference in doping concentration and the depth of the p-well in the deep n-well structures seem to have no influence on the dark current. This is different from the observations for the n-well

structures (interrupted lines). The dark current of the structures including a p⁺-well (dashed line) is significant smaller than the one including a shallow p-well (points), and over all, all n-well structures display a reduced dark current. All in all, the different structures vary not a lot in dark current: At 6 V and 60°C they are all in a range between 10 and 25 pA.

In Figure 77 the dark currents of the p-well in n-well structures, where the n-well is shorted to the p-substrate are shown. In this case the junctions between the p-wells and the n-wells are active (exemplary structures shown in Figure 76).

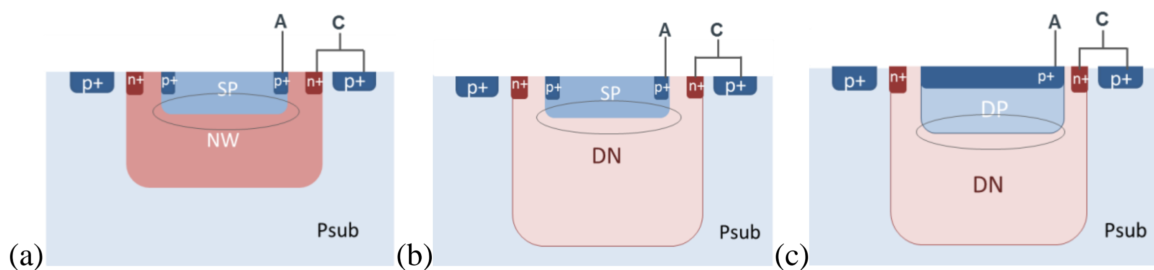

Figure 76: Exemplary structures with shallow active junction used for the dark current measurements shown in Figure 77: (a) Shallow p-well in n-well in p-substrate structure, (b) shallow p-well in deep n-well in p-substrate and (c) deep p-well in deep n-well in p-substrate.

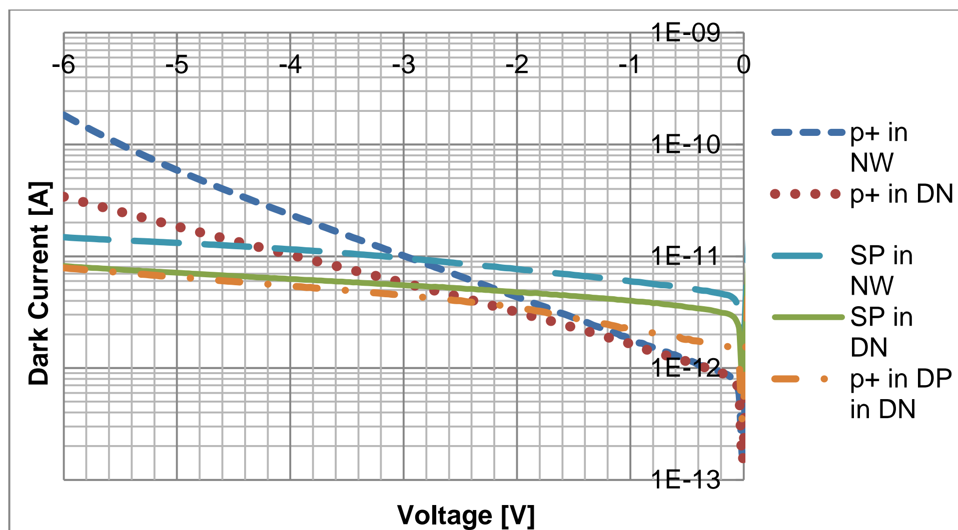

Figure 77: Dark current for the p-well in n-well structures (n-well shorted to p-substrate) as a function of voltage @ 60°C.

Looking at the interrupted lines, representing the p⁺-well in deep n-well (points) and p⁺-well in n-well (dashed), the band-to-band tunneling contribution can again be seen. Also

this time the junction is formed between two highly doped wells resulting again in a small depletion layer width. The higher slope of the p^+-well in n-well (blue dashed line) can be explained by the higher doping of the n-well compared to the deep n-well (red points).

The ordering of the rest of the structures cannot really be explained through the sources of dark current introduced in section 2.2. The shallow p-well in n-well (long dash) shows a higher dark current than the shallow p-well in deep n-well (solid), even though the n-well has higher doping concentration than the deep n-well. The deep p-well in deep n-well (dash dot) is lower in dark current than the shallow p-well in deep n-well (solid line) even though the slope of the yellow line is higher. The higher slope, of the p-well in n-well structure could be explained through the additional p^+-well added to the design.
In general one can see that the more complex the structures become the more effects influence the dark current preventing straightforward explanations.

Influence of field oxide on top of active area

The dark current behavior in dependence on the field oxide is in the case where the p-well is shorted to the n-well comparable to the behavior of the one-junction structures with field oxide, resulting in a decreased dark current with included field oxide.

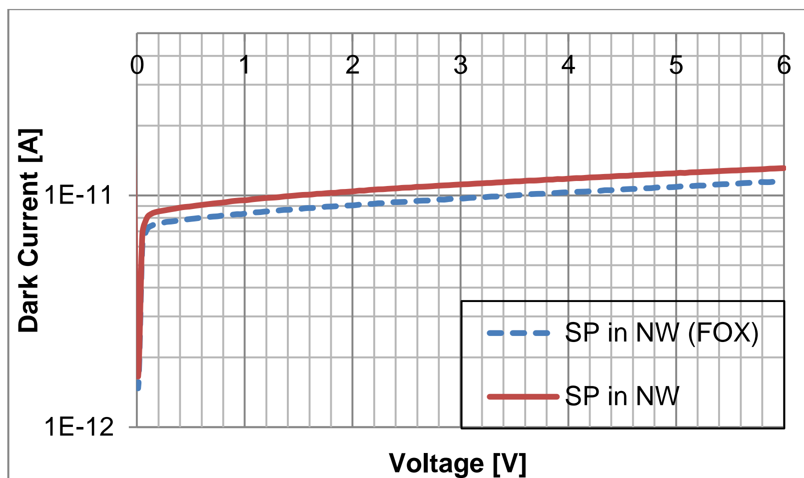

Figure 78: Comparison of dark current for the shallow p-well in n-well in p-substrate structure (p-well shorted to n-well) as a function of voltage between structures with (dashed line) and without (solid line) field oxide.

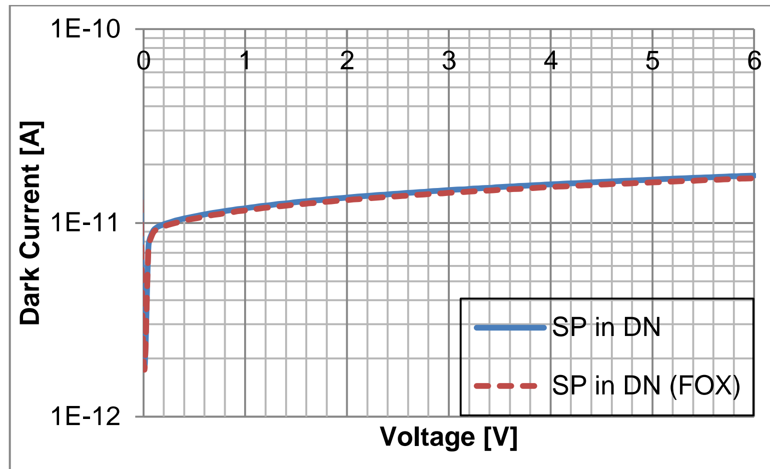

Figure 79: Comparison of dark current for the p-well in deep n-well in p-substrate structure (p-well shorted to n-well) as a function of voltage between structures with (dashed line) and without (solid line) field oxide.

As it can be seen in Figure 78 and Figure 79 again only the n-well structure shows a decreased dark current with field oxide on top of the active area and there is no difference when using the deep n-well structure.

A very unexpected effect of the field oxide was observed for the n-well shorted to the p-substrate, thus, observing the shallow junction. Examples are shown in Figure 80 and Figure 81.

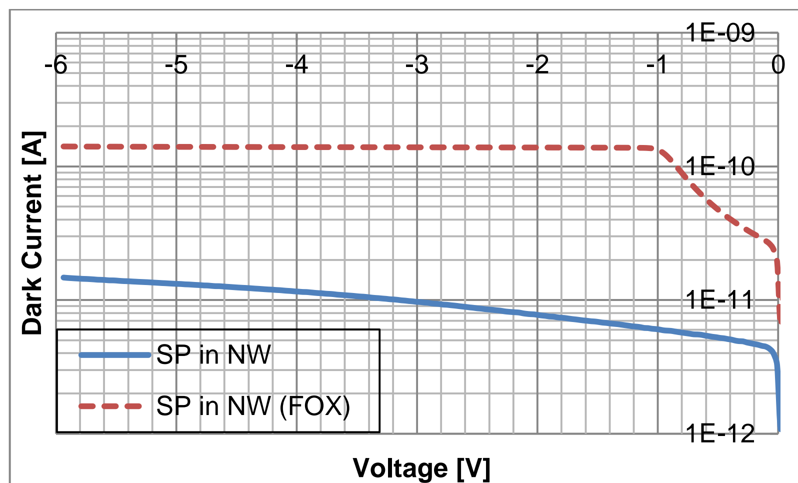

Figure 80: Comparison of dark current for the shallow p-well in n-well in p-substrate structure (n-well shorted to p-substrate) as a function of voltage between structures with (dashed line) and without (solid line) field oxide.

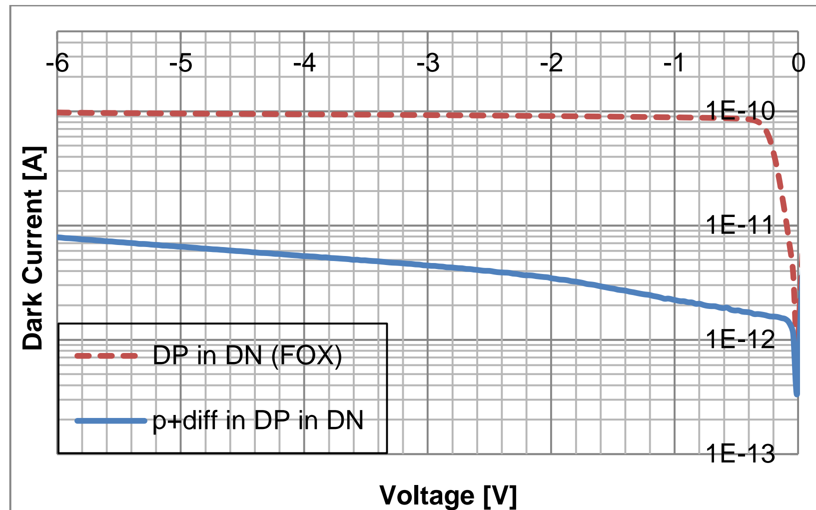

Figure 81: Comparison of dark current for the p-well in deep n-well in p-substrate structure (n-well shorted to p-substrate) as a function of voltage between structures with (dashed line) and without (solid line) field oxide.

In these cases, the dark current increases with adding field oxide on top of the active area. Looking at Figure 80, which compares the shallow p-well in n-well junctions with and without field oxide, a drastic increase of the dark current for the structure with field oxide can be seen. Beyond that, the field oxide results in saturation of the dark current at about 1V reverse bias voltage. A similar behavior can be seen in Figure 81 for the deep p-well in deep n-well in p-substrate structure, where saturation in the field oxide case starts already at lower voltages.

In the case of the shallow p-well in n-well junction this behavior can be explained by the doping profile and the production: The implantation step for the shallow p-well occurs after the field oxide formation. Like this the implantation has to be done all the way through the field oxide. This leads to a very shallow profile of the shallow p-well in the n-well. By increasing the reverse voltage the depletion layer width increases and touches the field oxide leading to a shorting of the diode.

A different effect is the source for the structure including the deep p-well. There the well is already implanted and diffused before the field oxide oxidation takes place. During the drive in step of the deep p-well, an interaction of the dopants in the silicon, with the field oxide takes place. This is called depletion effect and is explained in [29] and [30]. The cause is that the solid solubility of boron is higher in the SiO_2 than in the silicon itself this leads to diffusion of boron into the field oxide resulting in a depletion of boron atoms in

the silicon. This again leads to a shorting of the diode by applying a reverse voltage. Phosphor on the other hand, has a higher solid solubility in silicon than in the silicon dioxide leading to the so called pile-up effect during the drive in step, with the result that the phosphor atoms are pushed further into the silicon, having the maximum doping concentration deeper inside the silicon and not at the surface. In the case where no field oxide is on top of the photodiode but another oxide the drive in step of the deep p-well is already before the oxide is placed on the structure. Because of this, the depletion effect is not observed in these structures.

To show the influence of the additional junction in the two-junction design on the dark current a comparison with the dark current for a one-junction design is done. For this the dark currents of the simple deep n-well in p-substrate structure (Figure 82 (a)) is compared with the shallow p-well in deep n-well in p-substrate structure (Figure 82 (b)) and the deep p-well in deep n-well in p-substrate structure (Figure 82 (c)). All observed structures have the same active junction; the junction between the deep n-well and the p-substrate.

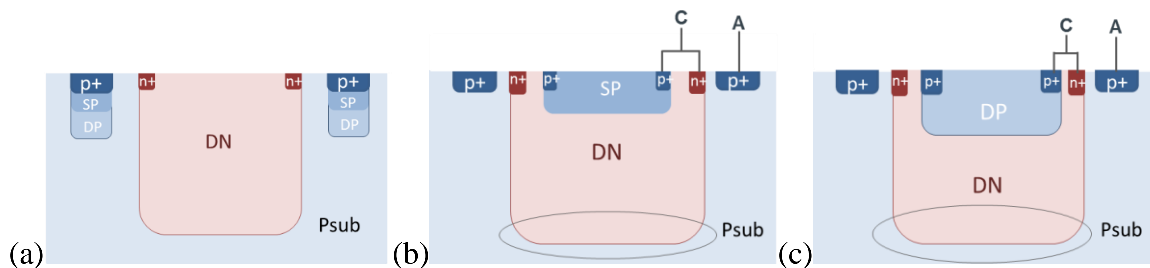

Figure 82: Schematic structures compared in Figure 83. (a): deep n-well in p-substrate, (b): shallow p-well in deep n-well in p-substrate and (c): deep p-well in deep n-well in p-substrate

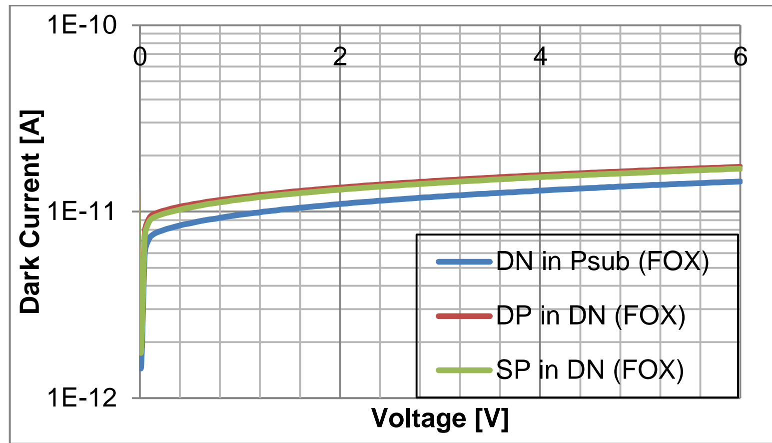

Figure 83: Dark current for different deep n-well structures as a function of voltage, showing the effect of different well combinations to dark current.

In Figure 83 one can see that by introducing a second well inside the deep n-well the dark current for the deep junction is slightly increased, while there is no difference between a shallow and a deep p-well is used.

Also the n-well structures shown in Figure 84 are compared with each other.

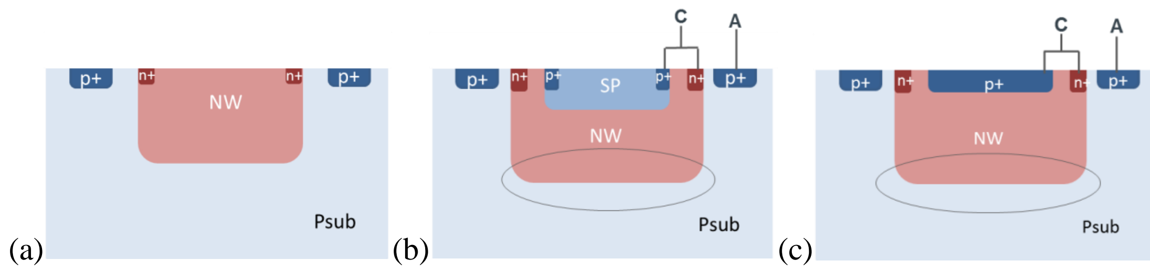

Figure 84: Schematic structures compared in Figure 85. (a): n-well in p-substrate, (b): shallow p-well in n-well in p-substrate and (c): p^+-well in n-well in p-substrate

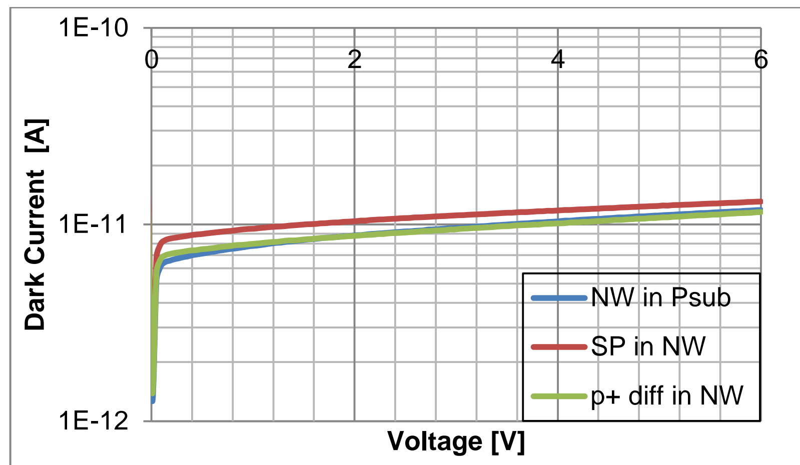

Figure 85: Dark current for different n-well structures as a function of voltage, showing the effect of different well combinations to dark current.

In Figure 85 one can see that for the n-well and p-substrate junction, again the well combination with the shallow p-well shows an increased dark current. The structure with the very shallow p^+-well has the same dark current as the n-well structure without additional junction.

Concluding one can say that for the simpler, one-junction structures the trend of the dark current is as expected and can be explained by the theory shown in section 2.2. The more complex the design of the photodiode gets, the more factors are influencing the dark current and the more difficult it becomes to explain the dark current behavior. For example using a two-junction structure and introducing a field oxide on top of the active area influences the dark current in an often non-trivial way.

6 DARK CURRENT AND CROSSTALK PERFORMANCE

Two very important parameters affecting the sensitivity of a sensor are dark current and crosstalk. As shown in this section for our devices the decrease of crosstalk leads to an increase of dark current.

In section 2 the structure of a CMOS sensor was described. It consists of an array of pixels. To avoid the interaction of these pixels, so called guard ring structures are introduced in the design. They should electrically separate the individual pixels from each other. To get a better understanding of the working principle of guard rings and their effect on crosstalk as well as on dark current; the following section will deal with these parameters as a function of guard ring designs.

6.1 Photodiode structure

Before the crosstalk effect, the dark current and the guard ring designs are introduced and the PIN photodiode used for the following investigations is presented. The advantages of using a PIN photodiode was already explained in section 2 where different photodiode types where presented. In Figure 86 the schematic cross section of the used PIN photodiode is shown. In all following investigations this kind of photodiode is used.

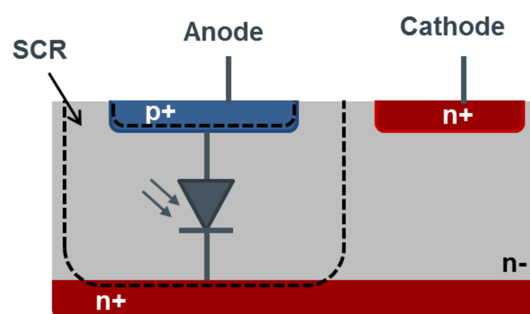

Figure 86: Schematic cross section of a PIN photodiode used in the following sections, SCR is the space charge region

A vertical PIN photodiode is formed between the buried n^+-cathode and the p^+-anode. The nearly intrinsic region of the PIN photodiode (grey region in Figure 86) consists of a high resistivity, n-type float zone silicon. This region is very lowly n-doped and labeled with n^-

in the schematics. To electrically connect the cathode, an n^+ implant layer is positioned on top and through the n^- layer down to the buried cathode. The series resistance induced through the low doped layer is no issue for the performance of the device. The space charge region is indicated through the dashed black line in Figure 86. [31]

6.2 Crosstalk theory

One has to distinguish between two different crosstalk mechanisms, the optical crosstalk and the electrical crosstalk. Optical crosstalk arises due to reflection, scattering and refraction of the light in the stack and at the surface. The mechanism of interest in this thesis will be the electrical crosstalk explained below.

The schematic principle causing this effect is shown in Figure 87. While illuminating a pixel, photons reaching the space charge region underneath the anode, are absorbed, and generate carriers inside the space charge region. These contribute to the photocurrent of the illuminated photodiode. Electron-hole pairs generated very deeply in the buried highly doped cathode are either also separated by the electric field or recombine. When carriers are generated in the field free intrinsic region between two diodes, they have the possibility either to diffuse to the illuminated photodiode or to neighboring photodiodes. The diffusion of minority carriers to neighboring photodiodes is referred to electrical crosstalk. This effect leads to carrier exchange between adjacent pixels resulting in smearing effects. [32]

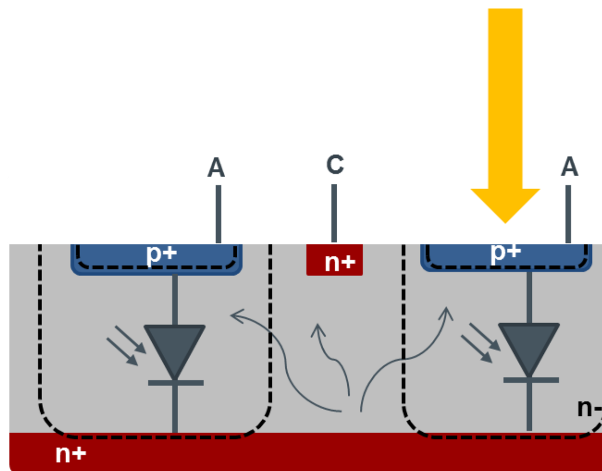

Figure 87: Schematic explanation for crosstalk, dashed lines indicate the space charge region of the pixels

To minimize this effect, so-called guard ring structures are introduced surrounding the photodiode. Their goal is to electrically separate the pixels from each other.

6.3 Working principle of a guard ring

One possible structure for a guard ring has already been presented in the work by Teva et al in [31]. It is a combination of highly doped p^+- and n^+-regions acting also as cathode contact. A schematic image of this structure is shown in Figure 88.

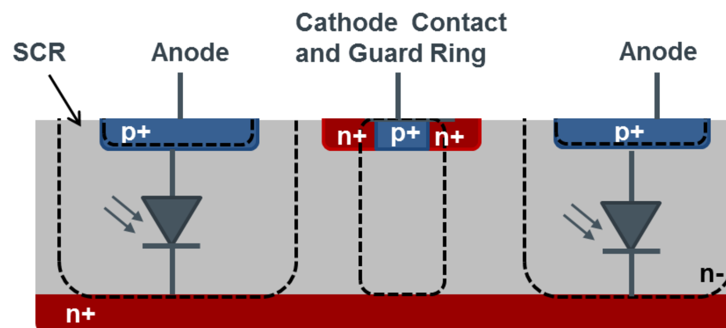

Figure 88: Schematic built up of a guard ring, consisting out of a combination of n- and p-doped regions

The n^+- and p^+-doped regions of the guard ring are shorted and kept at the same potential. Like this the guard ring does not act as active junction. Still, the p-n junction of the guard ring produces an electric field that results in an additional space charge region, as shown in Figure 88. On the one hand, a space charge region is formed between the n^+- and p^+-regions of the guard ring itself, and on the other hand, an even bigger space charge region is formed in vertical direction, because of the p^+ region of the guard ring and the buried cathode. This way, carriers which are generated between two neighboring pixels are collected by the guard ring. [31]

Introducing a guard ring also results in some drawbacks. The dark current is increased. Especially the continuing shrinking of the devices increases this effect. Thus, while one needs the guard ring to suppress the crosstalk effect; one has to deal with the increased dark current. This knowledge comes from earlier measurements comparing the dark current of arrays with and without guard ring. [33]

To find a way to minimize this additional dark current one has to find its source. To that aim an area-perimeter model can be used. By comparing the dark current of structures with differently sized anodes, which differ in the area to perimeter ratio, one find out whether the dark current is produced in the bulk or around the perimeter of the photodiode. A similar model is presented in [28].

6.4 Dark current

As first step to get an idea of the influence of the diode size, dark current measurements of the differently sized structures (listed in Table 7) have been performed. The parameter, which is varied, is the edge size of the anodes resulting in square or rectangular shaped diodes. To show the dependence of the dark current on the distance between the pixels to the guard ring, the dark current values of the differently sized diodes are compared with each other varying also the distance between the pixels. For this comparison dark current values at 5V reverse bias voltage were taken. The pixels used for these measurements, have the design and the guard ring structure shown in Figure 88. For the measurement, an array of 2 times 2 pixels is used (Figure 89).

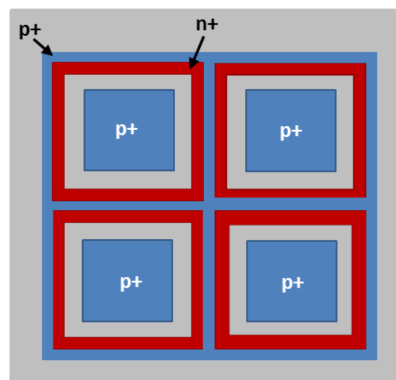

Figure 89: Top-view of diode array with npn-guard ring

All of the pixels share a common cathode (n^+-regions of the guard ring). For the dark current measurement the anodes of three pixels are contacted with tips and also the cathode is contacted. The voltage is applied at the common cathode and the current at the three anodes is recorded at the same time. The advantage of this measurement method is to measure three diodes at a time. To further minimize the error the measurements were done at 5 positions at the wafer. The shown dark current values for one structure are an average of these measurements.

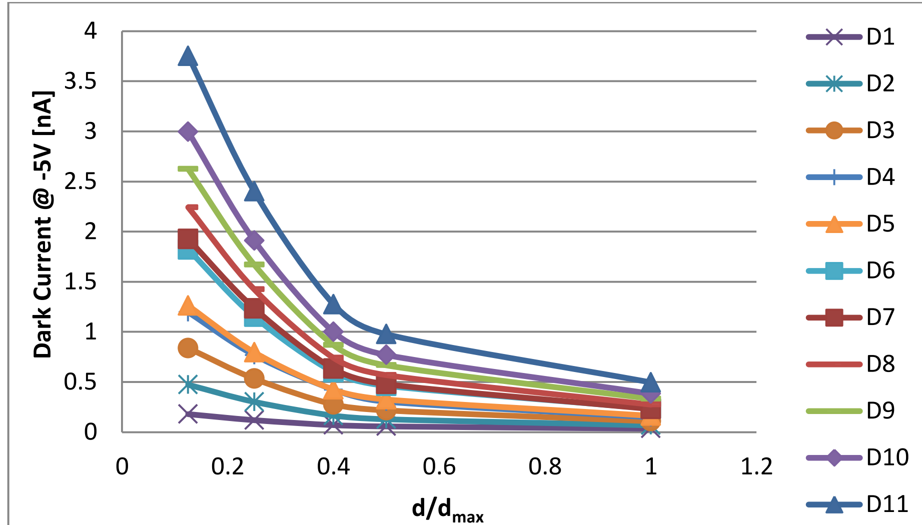

Figure 90: Dark current as a function of normalized distance between pixel and guard ring for different photodiode sizes. D1-D11 refer to anodes varying in size and area to perimeter ratio as listed in Table 7

Figure 90 shows the strong dependence of the dark current on the distance between pixel and guard ring. When decreasing the pixel-to-guard ring distance, a drastic increase in dark current is observed. Furthermore, one can see that the dark current decreases with decreasing anode size. For D1 (purple crosses) the dark current is the lowest it is the smallest structure and it increases in magnitude reaching a maximum for D11 (dark blue triangles, the device with the largest anode).

Table 7: List of diode structures compared in this chapter with different area to perimeter ratio

Name	Area to perimeter ratio [µm]
Diode1 (D1)	25
Diode2 (D2)	42
Diode3 (D3)	45
Diode4 (D4)	47
Diode5 (D5)	210
Diode6 (D6)	300
Diode7 (D7)	48
Diode8 (D8)	208
Diode9 (D9)	375
Diode10 (D10)	468.75
Diode11 (D11)	625

6.5 Area-perimeter model

In order to get a better understanding of dark current generation it is important to get an idea of where in the pixel the dark current is primarily generated. With that goal, a model, presented in [28], is used where the dark current is separated in a surface junction length dependent term and an area dependent term. The length dependent part arises from the p-n junction at the surface. The depletion layer region is not only vertical but extends also laterally along the sidewalls of the well. Therefore, there is a region on the surface that is part of the depletion layer, as can be seen in Figure 86 as well as in Figure 88. The area-dependent part is generated in the bulk underneath the anode of the pixel. The dark current resulting from the sum of the two terms is given by:

$$I_D = \alpha A + \beta P \tag{6.1}$$

Here, A is the area of the photodiode, P is the perimeter of the photodiode, α is defined as the current density generated in the bulk [A/µm²] and β is the current per µm generated at the surface [A/µm]

Using different size diodes with different area to perimeter ratio, α and β are calculated to get a model for the dark current for given structural dimensions. To validate this model the calculated values are compared to measured ones.

For calculating α and β two differently sized structures are chosen. For that a big one (D10) and a small one (D7) are chosen. Using the data for these, α and β are calculated for different distances between the pixels and the guard ring. To show also the temperature effect, the model values are calculated for experiments performed at 40°C as well as at 60°C. For all 5 different pixel-to-guard ring distances the two parameters are calculated using currents at 5mV reverse bias voltage and applying the following equations shown in (6.2). The results are compiled in Table 8.

$$\alpha = \frac{I_2 - \frac{P_2}{P_1} I_1}{A_2 - \frac{P_2}{P_1} A_1} \tag{6.2}$$

$$\beta = \frac{I_1 - A_1 \alpha_1}{P_1}$$

Table 8: α and β determined form the area-perimeter model as described in (6.2), T=60°C, 5mV reverse bias voltage

Normalized pixel-to-guard ring distance d/d_{max}	**α [A/µm²]**	**β [A/µm]**
0.125	1.8E-20	3.6E-14
0.25	1.5E-18	2.7E-14
0.4	-9.4E-19	1.6E-14
0.5	6.1E-20	1.3E-14
1	1.2E-18	6.5E-15

The values of α are very small, thus, the negative value of α for d/d_{max}=0.4 can be considered a numerical artifact. Using these parameter values, the perimeter related current as well as the area related current is calculated, for an exemplary structure (D11). The current values are listed in Table 9.

Table 9: Area related current and perimeter related current calculated for D11 (Table 7), reverse bias voltage is 5mV

Normalized pixel-to-guard ring distance d/d_{max}	**αA [A]**	**βP [A]**
0.125	1.1E-13	3.6E-10
0.25	9.6E-12	2.8E-10
0.4	-5.9E-12	1.6E-10
0.5	3.8E-13	1.3E-10
1	7.4E-12	6.5E-11

Although the used structure (D11) has the highest area to perimeter ratio of the tested structures, the perimeter related current is higher by one to three orders of magnitude.
This shows (compare [28]) that the surface depletion is the leading contribution to the dark current. But with the diode design used here, another point has to be kept in mind. A higher dark current was observed, using a guard ring, in comparison to guard less structures. [33] This led to the assumption that the guard ring structures are the reason for the enlarged dark currents. But this assumption fits just fine with the perimeter dependence of the dark current for the investigated diodes. The larger the perimeter of the structure the larger the perimeter of the guard ring and the bigger the influence of the guard ring. Furthermore one can see that the effect decreases with decreasing the distance between pixel and guard ring. That means the closer the guard ring is to the diode the higher the dark current.

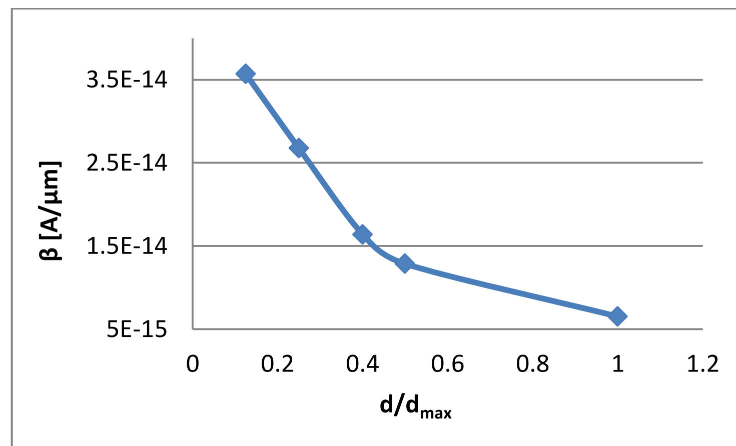

Figure 91: β as a function of normalized pixel-to-guard ring distance, parameters calculated for 60 °C, values for 5mV reverse bias

In Figure 91, β is shown as a function of the pixel to guard ring distance. One can see that β increases significantly with decreasing distance. In fact the evaluation displays the same shape as the dark current did as a function of pixel-to-guard ring distance (see Figure 90).

To determine whether there is a difference in α and β at higher voltage ranges, the parameters are calculated also for a higher reverse bias of 5V. The perimeter related current as well as the area related current are calculated out of α and β and the results are shown in Table 10. Also at high voltages the guard ring generated carriers are the

dominating effect. Moreover, in Figure 92 the dependence of the current on the guard ring to pixel distance has the same shape as in Figure 91.

Table 10: Area related current and perimeter related current calculated for D11 (Table 1), reverse bias voltage is 5V

Normalized pixel-to-guard ring distance d/d_{max}	αA [A]	βP [A]
0.125	2.4E-11	3.7E-04
0.25	3.8E-11	2.4E-04
0.4	4.7E-11	1.2E-04
0.5	5.5E-11	9.3E-05
1	4.5E-11	4.5E-05

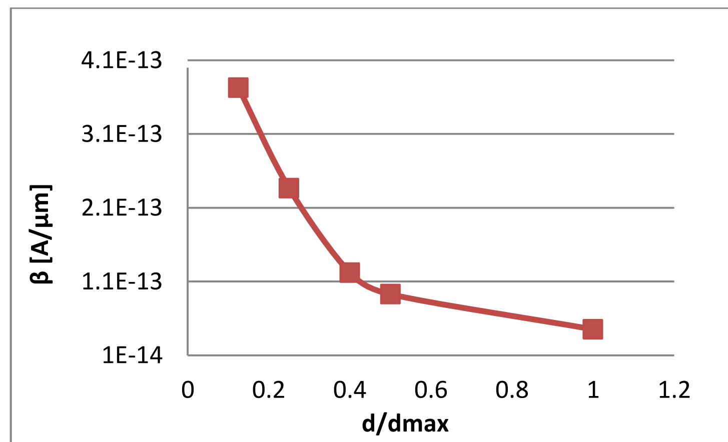

Figure 92: β as a function of normalized pixel-to-guard ring distance, parameters calculated for 60 °C, values for 5V reverse bias

To check the appropriateness of the determined values of α and β, the current is calculated for different pixel-to-guard ring distances and temperatures for all different size structures. The results are shown in Figure 93 and Figure 94. One can see that the model values fit very well to the measurements for both temperatures.

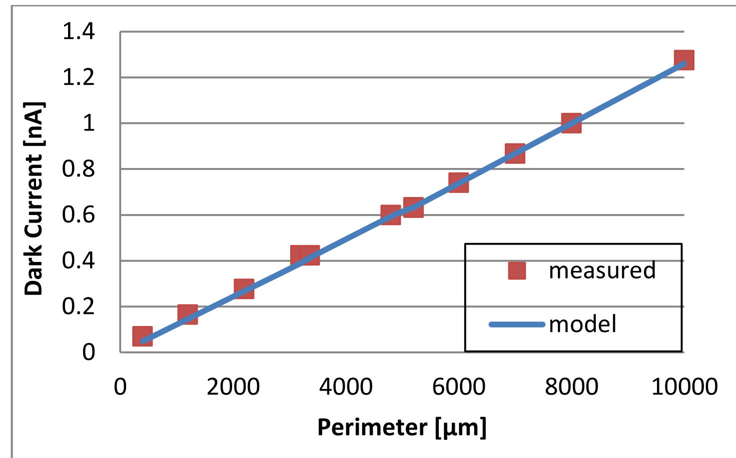

Figure 93: Dark current as a function of the perimeter of the structures in µm, fixed pixel-to-guard ring distance, T=60°C, reverse bias is 5V

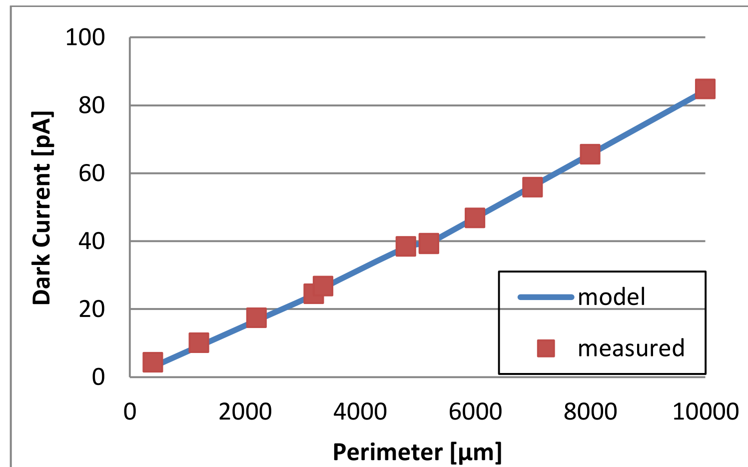

Figure 94: Dark current as a function of the perimeter of the structures in µm, fixed pixel-to-guard ring distance, T=40°C, reverse bias is 5V

A possible explanation for the additional dark current was already proposed in [31] and even more explicitly in [34]. It is rooted in the structure of the guard ring, shown in section 6.3. In fact, a parasitic bipolar transistor is created, which is responsible for additional carriers produced in this region. This is indicated in Figure 95.

As shown in [31], for guard-less structures, the diffusion and the generation term, are sufficient for describing the dark current behavior. Introducing a guard ring to the design increases the dark current, because of this there must be an additional contribution to the dark current. Like stated in [31] and [34] this additional part comes from a PNP transistor

which is formed by the p^+ guard ring (collector), the n^+ cathode contact and the n^- intrinsic layer forming together the base and the p^+ anode acting as emitter

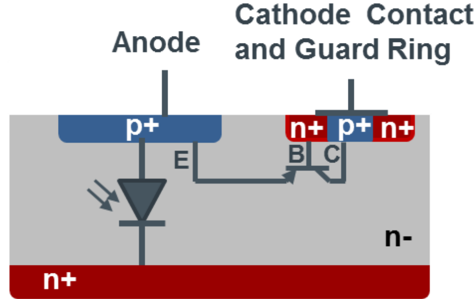

Figure 95: Schematic built up of photodiode with guard ring including the parasitic bipolar transistor

To model the lateral diffusion current between the anode and the guard ring, the emitter current of a PNP transistor is used in [34]. The emitter current of a PNP bipolar transistor, where the base is shorted to the collector is given by:

$$J_E = q\frac{D_p p_n}{L_p} coth\left(\frac{L_{GR}}{L_P}\right)\left[\left(e^{qV_{EB}/kT} - 1\right)\right] + q\frac{D_N n_p}{L_n}\left(e^{qV_{EB}/kT} - 1\right) \tag{6.3}$$

$D_{p/n}$, $L_{p/n}$ and p_n and n_p are the diffusion constants of hole and electrons, the diffusion length of holes and electrons and the carrier concentrations. L_{GR} is the distance between the guard ring and the anode of the photodiode.

Because of the very high doping concentration of the emitter compared to the base, the second term in (6.3) is negligible. Furthermore, by using an emitter to base voltage of -5V the exponential term can be ignored and the diffusion current coming from the PNP transistor is simplified to:

$$I_{Diff-pnp} \cong -qA_i\frac{D_p p_n}{L_p} coth\left(\frac{L_{GR}}{L_P}\right) \tag{6.4}$$

The first important thing, resulting from equation (6.4), is the negative sign of the current, indicating a current flow from the collector to the emitter. This is the same direction as the reverse current of the PIN photodiode, resulting in a summation of the parasitic current from the PNP transistor with the generation current in the space charge region of the photodiode. The second important point is the strong dependence of the parasitic current on the $\frac{L_{GR}}{L_P}$ ratio. This explains the influence of the guard ring to pixel distance on the dark current. [34]

The reason for the big impact of the parasitic transistor is the use of high quality float zone material in these photodiodes. By using such a high quality material, diffusion lengths of about 4mm are reached [34]. If a lower quality material was used the diffusion length would be reduced and, therefore, the parasitic effect of the guard ring would be lowered.
A more detailed discussion of the parasitic transistor and its influence to the dark current was already shown in the former work of Teva et al in [34].

6.5.1 Conclusion of area to perimeter model

In conclusion one can say that there is a strong dependence of the dark current on the pixel to guard ring distance. Furthermore, also a dependence on pixel size of the dark current was observed, where a better performance is observed for smaller pixels.

6.6 Temperature dependence of the dark current

The temperature dependence of the dark current is an important parameter dealing with photodiodes. [14] Because of this it was also investigated in this section. In order to do this the dark current was measured for selected diodes at different temperatures, for 27°C, 40°C, 55°C and 60°C.

To prove if the measured values fit with the theory, they are compared to a simplified model used in [35]. The temperature dependence occurs due to thermal generated carriers. Therefore, the dark current increases exponentially with the temperature and can be expressed by

$$I_{dark} = I_{dark,ref} \cdot 2^{(T-T_{ref})/T_d} \tag{6.5}$$

with I_{dark} being the dark current and $I_{dark,ref}$ the dark current at a reference temperature T_{ref}. T_d is the temperature range in which the dark current doubles. In the model 60°C are used as reference temperature and T_d was out of experience chosen to be 5°C [33].

The calculated values fit well with the measured ones and are compared in Figure 96. One can see a drastic increase of the dark current with temperature starting from about 40°C.

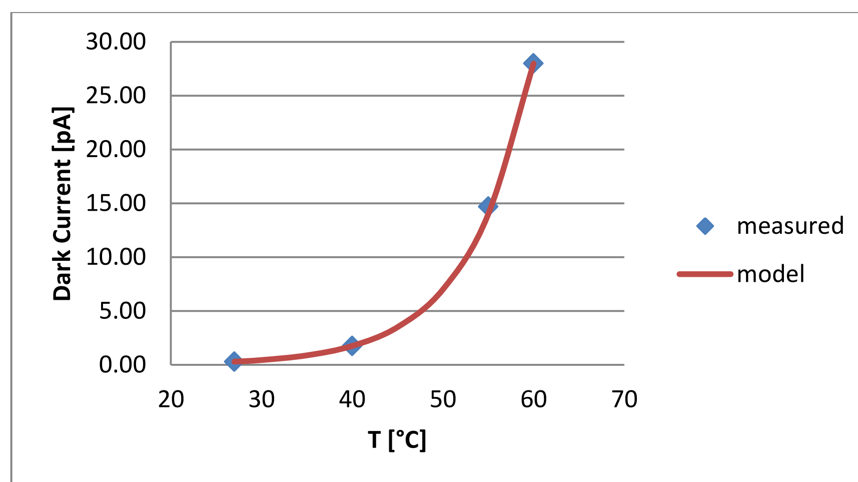

Figure 96: Dark current as a function of temperature in °C, comparison of measured data to model data

6.7 Evaluation of different guard ring designs

With the knowledge on the behavior of the photodiodes observed in the section above, the next step is to optimize the behavior of the guard ring. To find a compromise between low dark current and good crosstalk-behavior, different guard ring structures are designed and compared with each other with respect to dark current and crosstalk. One group of the guard-rings includes similar to the guard ring introduced in the section above a p-n junction to avoid crosstalk. Also 3 other design variations are tested avoiding crosstalk without including an additional p-n junction.

The labeling of the different teststructures in the following investigations is summarized in Table 11

Table 11: List of guard ring teststructures investigated in the following sections.

Labeling	**Explanation**
GR1	Variation of p-n junction structure
GR2	Variation of p-n junction structure
GR3	Variation of p-n junction structure
GR4	Variation of p-n junction structure
GR5	Variation of p-n junction structure
GR6	structure without p-n junction
GR7	structure without p-n junction
GR8	structure without p-n junction, electrical separation
NG	guard-less structure

6.7.1 Dark current

First of all the reverse bias region, for the different guard ring structures is compared. For these measurements the same pixel to guard ring distance is chosen for all structures.

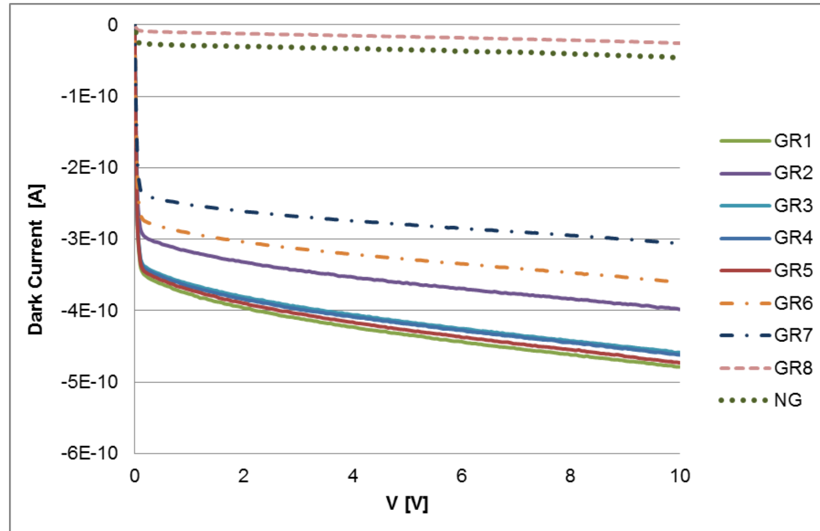

Figure 97: Dark Current as a function of. Voltage, comparison of reverse bias region of different guard ring designs (see Table 11), d/d_{max}=0.4

In Figure 97 a comparison of the dark current over the whole reverse bias region for the different designs can be seen. A big difference in dark currents between the guard-less (green dots) as well as the GR8 (pink stripes) structures and the other structures are observed. This proves the big effect of the guard ring on the dark current as stated in section 6.3. In particular, one can see that using the GR8 causes no additional dark current because of the absence of a junction in this design. The next structures with the next lowest dark current are GR6 and GR7. The guard ring designs including a p-n junction, show very similar dark currents.

As next step, the dependence of the guard ring on the distance between guard ring and pixel is analyzed. To illustrate this, dark current values for every guard ring design with a given voltage value of 5V, are plotted as a function of guard ring to pixel distance an in Figure 98.

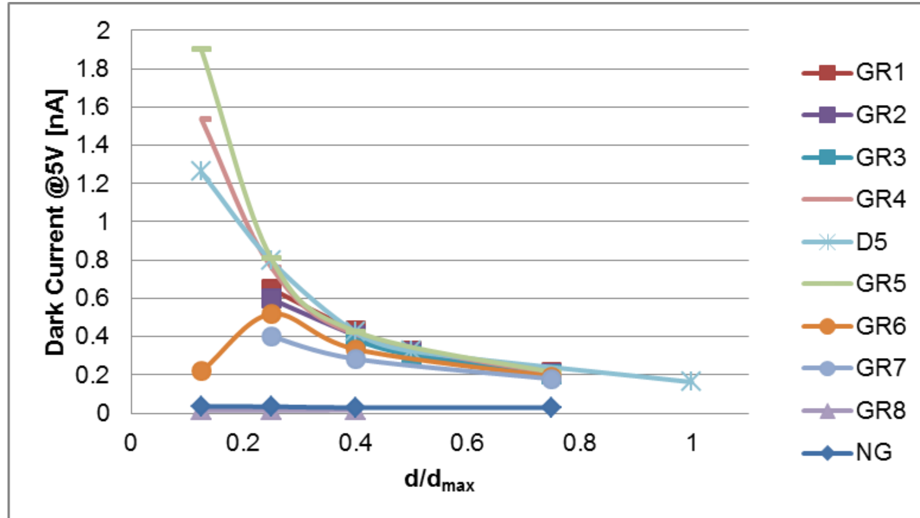

Figure 98: Dark current @ 5V as a function of pixel to guard ring distance for different guard ring designs

One can clearly see the influence of the pixel to guard ring distance on the dark current. Except for the guard-less structure (diamonds) and the GR8 structure (triangle) dark current increases with decreasing pixel to guard ring distance. The GR8 structure and the guard less structure show no dependence on the distance, which is related to the absence of a parasitic transistor in these structures.

The GR6 and GR7 structure (dots) show first also an increase of the dark current with decreasing distance. However, at very small distances, for GR6, the dark current decreases again.

Another finding is that the difference in dark current between the different designs is getting more significant with decreasing pixel-to-guard ring distance. While looking at longer distances, almost no difference in dark current for the different designs can be seen.

These results show clearly that the structures with additional p-n junctions in the guard ring show a higher dark current than the ones without. At that point one has to keep in mind that the implementation of a guard ring is necessary to reduce crosstalk, i.e. even though the dark current is much lower using no guard ring, the guard less structure is no option and included here only for comparison. The only design, which shows an even lower dark current than using no guard ring, is the GR8 structure, which does not include a

p-n junction or any other kind of diode. Thus, for minimizing the dark current, the best guard ring design is the GR8 followed by GR6 and GR7.

6.7.2 Crosstalk

After evaluating the dark current characteristics of the different guard ring structures, the crosstalk has to be measured and evaluated.

The crosstalk measurement is done using backside illumination. An array of photodiodes consisting out of 2 by 2 pixels is used. The measurement is started at the edge of one pixel. Then the chip is moved under the fiber so that the second photodiode becomes illuminated. The photocurrent is recorded as a function of the position of the device. A similar crosstalk measurement method is also used in [6] as well as in [7] and [36].

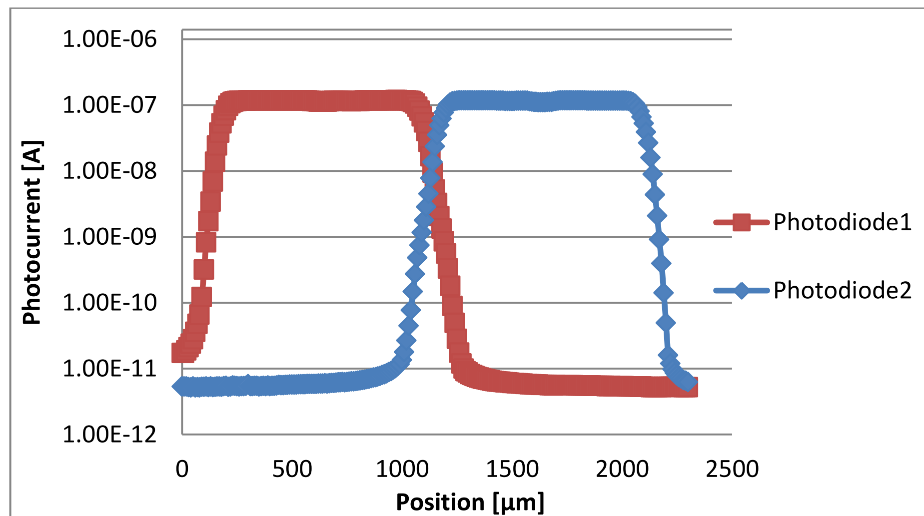

Figure 99: Crosstalk measurement, photocurrent of photodiode 1 and photodiode 2 as a function of position of the fiber on the chip

In Figure 99 the result of such a measurement can be seen. While the first diode is illuminated its photocurrent reaches a maximum and the second diode is at its minimum. The situation is reversed, when illuminating photodiode 2. In between these two regions there is an overlapping area. In this area, for example, carriers contribute to the photocurrent of the second photodiode while the first one is still illuminated. The percentage of this amount of current in respect to the current, produced in photodiode 1 while illuminating this photodiode, is defined as the crosstalk.

To calculate the crosstalk, the photocurrent was integrated from the edge of photodiode 1 to the crossing point of the two curves. The crossing point is defined as the point where photodiode 1 and photodiode 2 have the same photocurrent value. In the ideal case, this point is the position of the center of the guard ring.

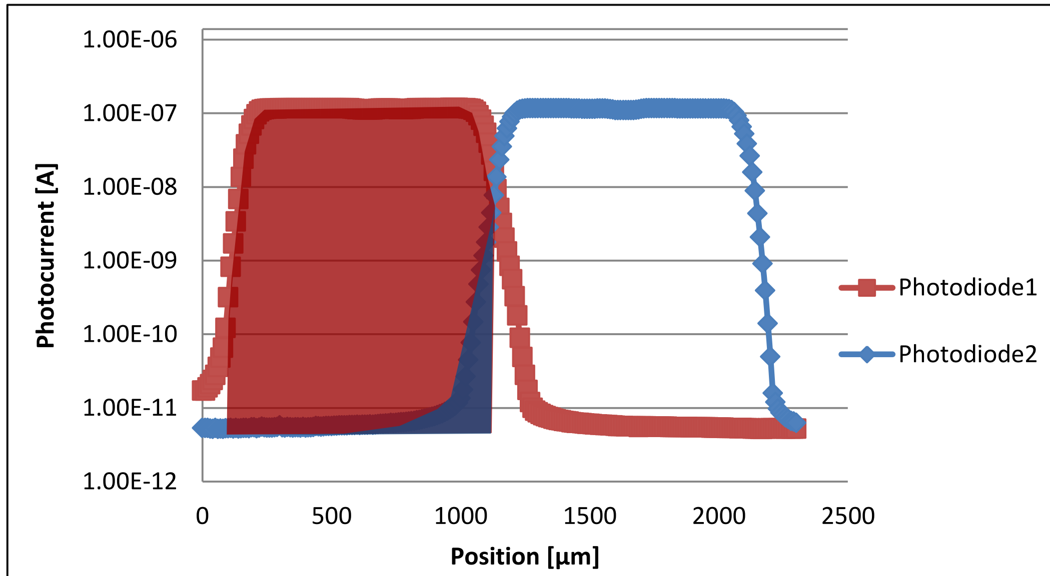

Figure 100: Crosstalk measurement, photocurrent as a function of position, with area under photodiode 1, from starting point to crossing point (red area) and area under photodiode 2, from starting point to crossing point (blue area)

The blue area in Figure 100 is the area below the photocurrent from photodiode 2 and the red area is the area below the photocurrent from photodiode 1. By dividing the blue area by the red area the relative response of photodiode 2 when illuminating photodiode 1 is given. The same is done with calculating from the right side getting the relative response of photodiode 1 when illuminating photodiode 2. The average of the two calculations is used as crosstalk value.

By using this method one has to be aware that the crossing point cannot be evaluated absolutely precisely because the step size of the chuck is too big. Still even when using a smaller step size it is unlikely to measure exactly in the middle of the guard ring.

Using this procedure the crosstalk is measured and evaluated for all used guard ring structures as a function of the pixel-to-guard ring distance. The measurements were done for two different wavelengths in order to investigate a possible wavelength dependence of

the crosstalk. Two LED light sources are used with a peak wavelength of 670nm and 850nm. The results are shown in Figure 101 and Figure 102.

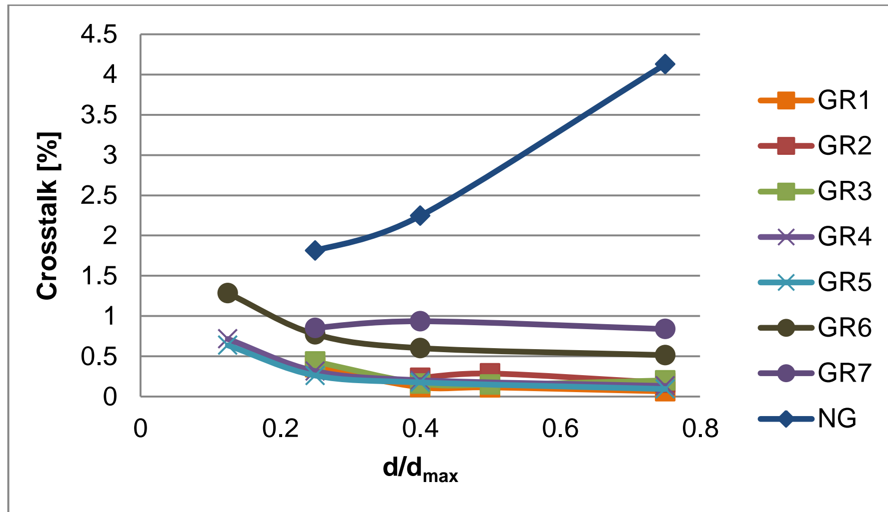

Figure 101: Crosstalk as a function of normalized pixel to guard ring distance of different guard ring structures at a wavelength of 670nm

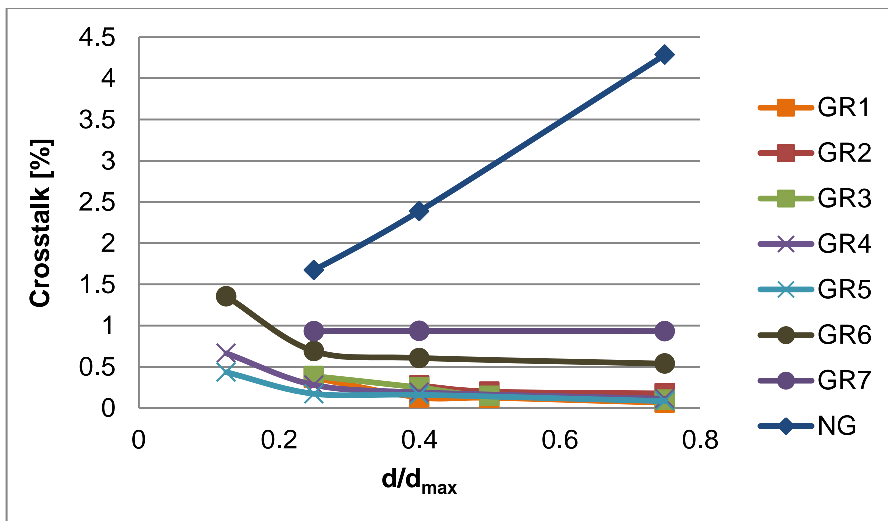

Figure 102: Crosstalk in as a function of normalized pixel to guard ring distance of different guard ring structures at a wavelength of 850nm

Comparing Figure 101 and Figure 102 one can see that there is no significant difference between the measurements with different wavelengths. By having a closer look to the plots two unexpected effects can be seen. The crosstalk for the guard-less structure (blue diamonds) increases with increasing distance. This is related to the long diffusion length mentioned before. The bigger the distance between the pixel and the guard ring, the larger

is the space in between the pixels where carriers are generated by illumination. The more carriers are generated the more diffuse to the pixels, thus, leading to an increased crosstalk. Due to the integration from the edge to the crossing point this effect can be seen in the crosstalk results. Because of this one sees that the crosstalk measurements for the guard less structures are not adequate. Due to the design of GR8 it was not possible to achieve satisfying results for the crosstalk with this measurement method. The reason for this is due to the too big fiber diameter, which is much bigger than the width of the guard ring structure. Even when the center of the fiber is exactly at the position of the guard ring, one still generates carriers on the right as well on the left side of the structure. This shows that the used measurement method is not suitable for this structure. Because of the built-up, assuring electrical separation, of the GR8 structure no crosstalk is possible.

Furthermore one can see in Figure 101 and Figure 102 that the crosstalk for the GR6 and GR7 (dots) are larger than for the other guard rings including a p-n junction. Moreover there is almost no variation in crosstalk for the different p-n junction designs.

One has to keep in mind that the measurement goes along with a lot of errors resulting from the big fiber diameter and the step size of the measurement as well as the distance of the fiber to the surface resulting in a wider or narrower diameter. Another complication was that the fiber had to be changed during the time the measurements where done. Thus, not all data were recorded with exactly the same fiber conditions. Because of all complications described above, it is hard to come to a clear conclusion and one must not forget that the systematic error of each data point can be large. Still it appears that the guard ring structures from GR1 to GR5 show a similar crosstalk, while the situation is worse for the GR6 and GR7, “compensating” for their lower dark currents.

6.8 Guard-less design

While measuring the dark current of the guard less design, an unexpected observation was made prompting to further investigations of this structure. As a result an additional effect of the guard ring concerning the dark current was observed.

As explained in section 6.4 to minimize the error, the dark currents of three pixels were measured simultaneously. It would be expected to get an almost equal value for the current at all three anodes (A1, A2 and A3), because of the same design and measurement conditions. That is not the case for the dark current measurements of the guard-less photodiodes. Always the same diode shows a lower current compared to the others. The diodes are ordered like shown in Figure 103 in an array.

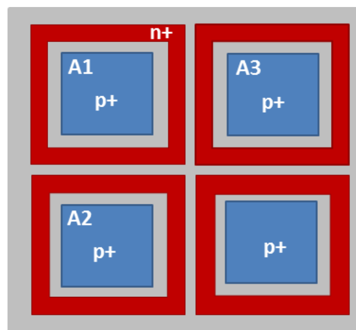

Figure 103: Top-view of array built up of guard-less design

The diode with the low current is always the one which faces two other diodes, in this case A1. The dark current measurements of the three pixels are compared in Figure 104. Resulting from these findings more measurements were made to find the reason for this behavior.

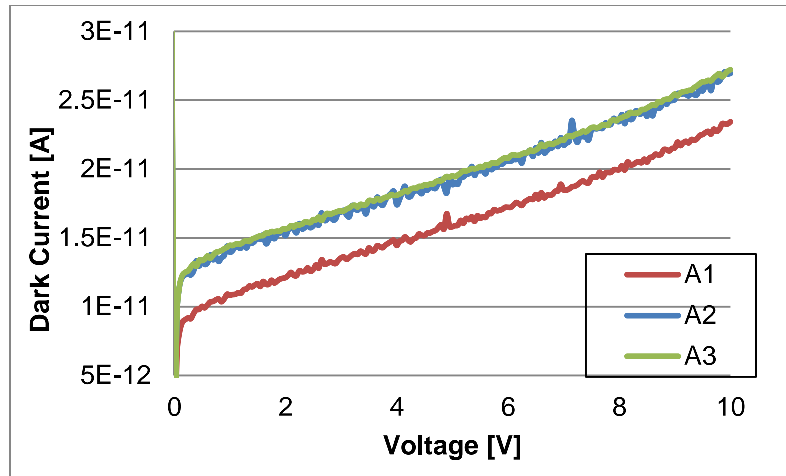

Figure 104: Comparison of the dark current as a function of cathode voltage between the three different anodes A1, A2 and A3

To get a better idea of the effect, a measurement with just one contacted anode (single-anode measurement) was done and is compared to the measurement of the same diode while contacting three anodes (multi-anode measurement), shown in Figure 105.

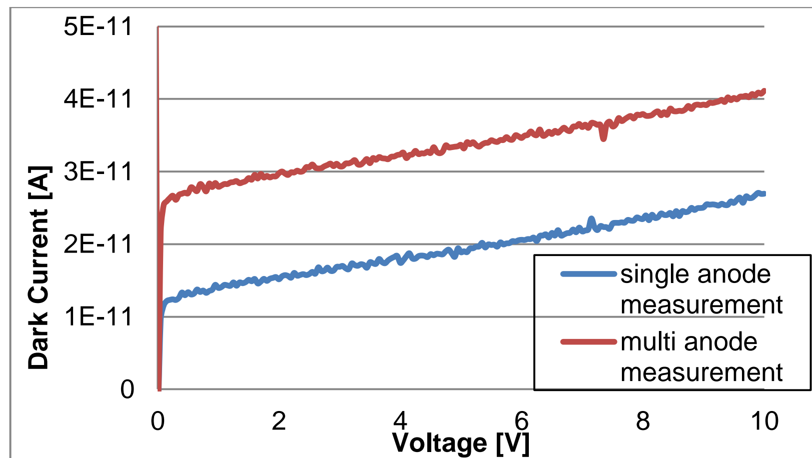

Figure 105: Comparison of dark current as a function of cathode voltage between single-anode and multi-anode measurement

This difference in dark current (Figure 105) between single- and multi-anode measurements leads to the conclusion that the diodes are interacting with each other during the measurement.

In a next step the anode is forced to a voltage and the cathode current is recorded. This way one has the possibility to connect the anodes in parallel by shorting the anode tips. When contacting one anode the current at the cathode should be the same as at the current

at the anode. By contacting 2 anodes the current at the cathode should be twice the value and so on. Doing the measurements this is not observed. The current at the cathode increases when more diodes are connected in parallel but not linearly with the number of diodes. The results can be seen in Figure 106.

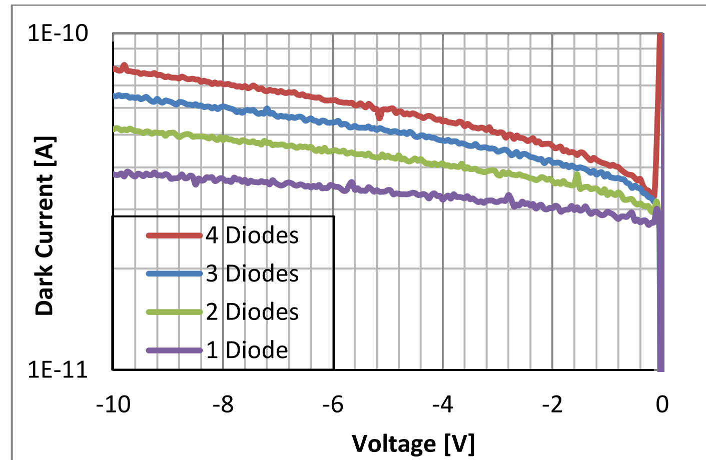

Figure 106: Comparison of dark current as a function of voltage between 1 to 4 diodes measured in parallel

It is assumed that the difference in current obtained for single- and multi-anode measurements is due to minority carriers in the intrinsic region. Because the different diodes are not elecrtical seperated form each other, it makes a difference whether just one or more anodes are contacted. In Figure 107 and Figure 108 the situation is scatched qualitatively. When there is just one anode activated, all the minority carriers of the array will diffuse to this anode as schematically shown in Figure 107. When two or more anodes are contacted, these andoes will share the minority carriers and, therefore, the current at an individual anode will decrease compared to the measurement of just one anode (Figure 108). A similar situation is also discussed in [37].

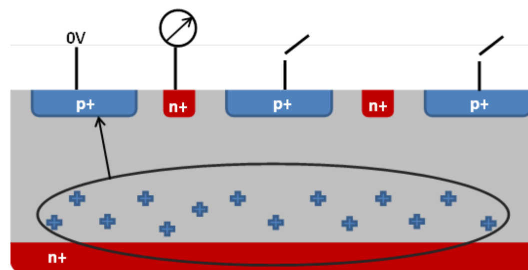

Figure 107: Single-anode measurement where the voltage is swept over the cathode, behavior without guard ring

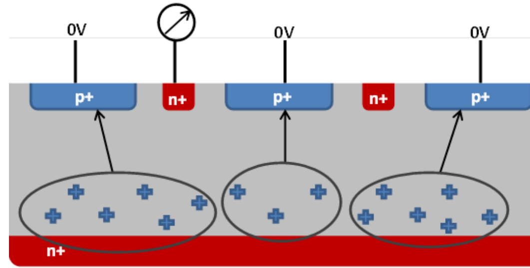

Figure 108: Multi-anode measurement where the voltage is swept over the cathode, behavior without guard ring

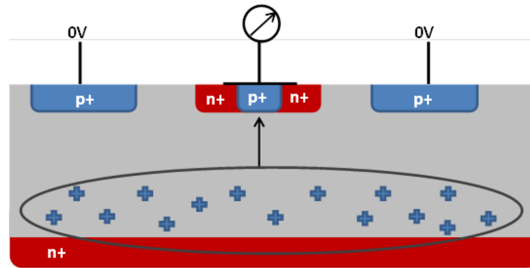

Figure 109: Multi-anode measurement where the voltage is swept over the cathode, behavior with guard ring

In Figure 109 the behavior after introducing a guard ring to the structure is schematically shown. The electrical field produced by the guard ring does not only remove carriers affecting crosstalk, but also the minority carriers in the bulk. This is the reason why the above described effect of different measurement results for multi- and single-anode measurements is not observed for structures with guard ring.

Althouhg the dark current of guard-less structures is higher for single-anode measurements, it is still much lower than the dark current of structures with a guard ring. One can say that the contribution to the dark current coming from minority carriers is much smaller than the carriers produced due to the guard ring.

In order to quantify these assumptions the minority carrier concentration in the charge neutral region is calculated and compared to the current difference between single- and multi-anode measurements. To do that the following equation for dark current is used. [14]

$$J_R = \underbrace{-q\sqrt{\frac{D_p}{\tau_p}} * p_n}_{\substack{minority\ carrier\ diffusion \\ from\ charge \\ neutral\ region}} + \underbrace{\frac{q n_i W}{\tau_p}}_{\substack{gereration\ current\ inside \\ the\ depletion\ region}} \left[\frac{A}{cm^2}\right] \tag{6.6}$$

With q as the elemental charge, D_p the diffusion coefficient of holes, τ_p the carrier lifetime of holes, p_n the minority carrier concentration, n_i the intrinsic carrier concentration and W as the space charge region width. [14]

In the following investigations just the first term of equation (6.6) is of interest, because we want to evaluate the contribution to the dark current coming from minority carriers in the field free region.

The minority carrier lifetime in the lowly doped n^- region is about 5 ms [34] and the temperature dependend diffusion coeficient is calculated with the following equation [34].

$$D_p(T) = \frac{\mu_p(T)kT}{q} \tag{6.7}$$

Also the hole mobililty μ_p is temperature dependend additionally it is dependent on the impurity level of the substrat. In this case a low-doped substrate is used and the mobility is calculated with a semi empirical formula, given by [34]:

$$\mu_p\left(\frac{cm^2}{Vs}\right) = 500 * \left(\frac{T}{300}\right)^{-2.3} \tag{6.8}$$

Also the intirnsic carrier concentration is usually calculated with a semi empirical model.

$$n_i(cm^{-3}) = 9.15 * 10^{19} * \left(\frac{T}{300}\right)^2 * e^{\left(-\frac{6800}{T}\right)} \tag{6.9}$$

At room temperature the following relation for the minority carrier concentration p_n applies.

$$p_n = \frac{{n_i}^2}{N_D} \tag{6.10}$$

Where N_D is the donor doping level. But with increasing temperatures this equation comes to its limitation and has to be replaced by an other expression, shown in (6.11).

$$p_n = \sqrt{n_i^2(T) + \left(\frac{N_D}{2}\right)^2} - \frac{N_D}{2} \tag{6.11}$$

Equation (6.11) takes into account that with increasing temperature the semiconductor becomes intrinsic. [34]

Out of these equations the current produced through the diffusion of minority carriers is calculated to evaluate the portion of this current to the dark current. As a result one gets a value of about 1.792 pA what is in the range of the difference between singel- and multi-anode measurements. With this result it is proved that the increased dark current in single-anode measurements is due to minority carriers in the field free region of the device. Furthermore an additional effect of the guard ring was found, next to avoiding crosstalk also the minority carriers from the bulk are collected by the guard ring.

6.9 Conclusion to guard ring

The above described results show that all guard ring designs including a p-n junction show a similar behavior in crosstalk as well as in dark current. The Schottky diode structure, which showed a better dark current behavior, “compensates” this with an increased crosstalk.

The only structure not producing a lot of dark current and being effective against crosstalk, even though it was not possible to prove that with the experimental method used here, is the isolation trench.

7 CONCLUSION

In this thesis the influence of different design variations on photodiode parameters is discussed. The evaluated parameters are in the first part the spectral responsivity and the dark current and in the second part the dark current and the crosstalk.

In the first part it was shown that one can tune the spectral responsivity by design variations, in particular the doping profiles. It is, however, found that this works only, when the diffusion component of the photocurrent is suppressed. One way to do this is to use well combinations with higher doping to decrease the diffusion length. A second, more efficient, way is to include an additional inactive junction to collect carriers generated in undesired regions outside the active depletion region. Furthermore, the spectral responsivity can be influenced positively by introducing an additional field oxide and by using an epi-wafer instead of a standard wafer. It is shown that for structures where the diffusion component to the photocurrent is suppressed it is possible to calculate the responsivity behavior with a simple analytical model neglecting the diffusion part.

Regarding the dark current a very promising behaviour was observed for all structures discussed in this thesis. Structures with a very narrow depletion region are found to display a (super)exponential increase of the dark current with reverse bias resulting from tunneling effects. The more complex the structures become, the more complicated it gets to unambiguously explain the dark current behavior. An undesired very high dark current was observed when introducing a field oxide on top of the active area of the photodiode structures.

In the second part of the thesis, the influence of different guard ring designs on the dark current and on the crosstalk was evaluated. By introducing the necessary guard rings to suppress crosstalk, an increased dark current is observed. Furthermore, by reducing the distance between the pixels, thus, between the anode and the guard ring, the dark current is further decreased. Between the different guard-ring designs including a p-n junction no significant difference neither in dark current nor in crosstalk was found. While the GR6 and GR7 structures show a lower dark current compared to the p-n junction structures, the

crosstalk is increased within these structures. The only guard ring structure having an even lower dark current than the guard-less structure and being effective against cross talk is the GR8 structure, which ensures electrical separation between pixels. Additionally, a second effect of the guard ring was found. Not only carriers due to crosstalk are collected by the guard ring but also minority carriers in the bulk are collected.

8 LIST OF FIGURES

Figure 1: Formation of depletion region with a negative region on p-side and a positive region on n-side [11] 4
Figure 2: Abrupt p-n junction in thermal equilibrium: (a) Space charge distribution, (b) electric field distribution, (c) potential variation with distance (V_{bi} is the built-in potential) [8] 5
Figure 3: Ideal diode IV-characteristic [11] 9
Figure 4: Biasing modes – depletion layer width and energy bands: (a) 0V bias, (b) forward bias, (c) reverse bias [8] 10
Figure 5: Irradiance of light at different wavelengths as a function of the distance from surface, blue line: λ=400nm, green line: λ=600nm, yellow line: λ=800nm and red line: λ=1000nm 16
Figure 6: Absorption coefficient and penetration depth as a function of wavelength and energy [15] 17
Figure 7: Generation rate divided by I_0 as a function of propagation depth nm for different wavelengths, blue line: λ=400nm, green line: λ=600nm, yellow line: λ=800nm and red line: λ=1000nm 18
Figure 8: Effect of electron-hole pair generation through light resulting in photocurrent [1] 19
Figure 9: Drift and diffusion current regions contributing to the photocurrent 20
Figure 10: Schematic build-up of a PIN photodiode 21
Figure 11: PIN photodiode: (a) PIN photodiode schematic structure, (b) carrier distribution, (c) charge distribution, (d) electric field distribution and (e) band diagram of a pin junction under reverse bias [1] 22
Figure 12: Schematic build-up of a single photon avalanche diode, including a p-well guard ring [1] 23
Figure 13: Schematic structure of passive pixel sensor with RS as the row selection transistor [20] 30
Figure 14: Schematic structure of Active Pixel Sensor with RST as reset transistor, RS as addressing transistor and SF as source follower [20] 31
Figure 15: Schematic build-up of APS with a pinned Photodiode, TX is the transfer gate [20] 32
Figure 16: Architecture of a two-dimensional CMOS image sensor [20] 33
Figure 17: Measurement setup showing the Cascade Microtech point probe station 35
Figure 18: Block diagram of the tunable monochromatic light source [22] 36
Figure 19: Schematic measurement setup for optical measurements 37
Figure 20: Fiber for optical measurements 38
Figure 21: Schematic structure of photodiodes with: (a) shallow and very highly doped n^+-well in lightly p-doped substrate, (b) shallow n-well in lightly doped p-substrate, (c) n-well in lightly p-doped substrate, (d) deep n-well in lightly doped p-substrate. The meaning of the labels of the structures is explained in Table 2 40

Figure 22: Schematic structure of photodiodes with: (a) n^+-well in shallow n-well in deep n-well in lightly doped p-substrate and (b) n^+-well in n-well in lightly doped p-substrate. The meaning of the labels of the structures is explained in Table 2 41
Figure 23: Schematic structure of photodiode with a n^+-well in p-well in lightly p-doped substrate. The meaning of the labels of the structures is explained in Table 2 41
Figure 24: Schematic structure of photodiodes with: (a) very shallow and highly doped p^+-well in n-well in lightly doped p-substrate, (b) shallow p-well in n-well in lightly doped p-substrate (c) very shallow and highly doped p^+-well in deep n-well in lightly p-doped substrate, (d) shallow p-well in deep n-well in lightly doped p-substrate (e) very shallow and highly doped p^+-well in deep p-well in deep n-well in lightly doped p-substrate and (f) deep p-well in deep n-well in lightly doped p-substrate. The meaning of the labels of the structures is explained in Table 2 42
Figure 25: Different shorting modes: (a) activating the deep junction by shorting the p-well and the n-well and (b) activating the shallow junction by shorting the n-well and p-substrate............. 43
Figure 26: Positioning of field oxide on top of the photodiode structure, (a) active area of photodiode is free of field oxide and (b) field oxide over the whole photodiode...................... 44
Figure 27: Exemplary built up of a photodiode including consisting of. With a Interlevel dielectric (ILD) several as Intermetal dielectrics (IMD) and a passivation layer for protection [12] 44
Figure 28: Exemplary one-junction structures with deep active junction used for the dark current measurements shown in Figure 29: (a) n^+-well in p-substrate, (b) deep n-well in p-substrate and (c) n^+-well in n-well in p-substrate. 46
Figure 29: Responsivity as a function of wavelength comparing different n-well structures in p-substrate. Cross sections of the structures are shown in Figure 21. 46
Figure 30: Comparison of responsivity as a function of wavelength between highly doped n^+-well in p-substrate and highly doped n^+-well in p-well 48
Figure 31: Responsivity as a function of wavelength comparing different n-well structures in p-substrate showing the low wavelength region. 50
Figure 32: Comparison of responsivity as a function of wavelength between applied reverse bias of 2V and no applied bias for the n^+-well in p-substrate structure. 51
Figure 33: Comparison of responsivity as a function of wavelength between applied reverse bias of 2V and no applied bias for the n^+-well in p-well structure... 51
Figure 34: Comparison of responsivity as a function of wavelength between the n-well in p-substrate structure with and without field oxide on top of the photodiode. Structures are shown in Figure 26. 52
Figure 35: Comparison of responsivity as a function of wavelength of the shallow p-well in n-well in p-substrate structure between the two different shorting modes. 53
Figure 36: Comparison of responsivity as a function of wavelength of the shallow p-well in deep n-well in p-substrate structure between the two different shorting modes. 54

Figure 37: Responsivity as a function of wavelength of the deep n-well in p-substrate junction. The effect of an additional junction on the responsivity is shown. ... 54
Figure 38: Responsivity as a function of wavelength, showing the effect of well combination to responsivity for a n-well in p-substrate junction. One time with an additional shallow p-well (dashed) and one time without (solid) ... 55
Figure 39: Exemplary structures with deep active junction used for the responsivity measurements shown in Figure 40: (a) Shallow p-well in n-well in p-substrate structure, (b) shallow p-well in deep n-well in p-substrate and (c) deep p-well in deep n-well in p-substrate. ... 56
Figure 40: Responsivity as a function of wavelength of the p-well in n-well in p-substrate structures. The p-well is shorted to the n-well. All schematic structures are shown in Figure 24. ... 56
Figure 41: Exemplary structures with shallow active junction used for the responsivity measurements shown in Figure 40: (a) Shallow p-well in n-well in p-substrate structure, (b) shallow p-well in deep n-well in p-substrate and (c) deep p-well in deep n-well in p-substrate. ... 57
Figure 42: Responsivity as a function of wavelength of the p-well in n-well in p-substrate structures. The n-well is shorted to the p-substrate. Schematic structures are shown in Figure 24. ... 58
Figure 43: Responsivity as a function of wavelength of the shallow p-well in n-well in p-substrate (p-well shorted to n-well) structure with and without field oxide. ... 59
Figure 44: Responsivity as a function of wavelength of the shallow p-well in deep n-well in p-substrate (n-well shorted to p-substrate) structure between with and without field oxide. ... 59
Figure 45: Responsivity as a function of wavelength of the p^+ in n-well in p-substrate (n-well shorted to p-substrate) structure. Use of epi-wafer (solid line) in comparison to standard wafer (dashed line). ... 60
Figure 46: Responsivity as a function of wavelength of the p^+ in n-well in p-substrate (p^+ shorted to n-well) structure. Use of epi-wafer (solid line) in comparison to standard wafer (dashed line). ... 60
Figure 47: Logarithmic plot of the simulated doping concentration as a function of distance from surface for the deep n-well in p-substrate structure. Dashed red: net doping, green: doping concentration of deep n-well and blue: doping concentration of p-substrate. ... 63
Figure 48: Logarithmic plot of the net-doping concentration as a function of distance from surface of the deep n-well in p-substrate structure. The simulated data are compared to the calculated data out of the fit. ... 63
Figure 49: Logarithmic plot of the doping concentration as a function of distance from surface for the shallow n-well. The data is obtained from simulations. ... 64
Figure 50: Logarithmic plot of the doping concentration as a function of distance from surface for the n+-well. The data is obtained from simulations. ... 64
Figure 51: Logarithmic plot of the net-doping concentration as a function of distance from surface of the shallow n-well in p-substrate structure. The simulated data are compared to the calculated data out of the fit. ... 65

Figure 52: Logarithmic plot of the net-doping concentration as a function of distance from surface of the n^+-well in p-substrate structure. The simulated data are compared to the calculated data out of the fit. 65

Figure 53: Logarithmic plot of the simulated doping concentration as a function of distance from surface for the deep p-well in deep n-well in p-substrate structure. Dashed red: net doping, green: doping concentration of deep n-well and blue: doping concentration of deep p-well. . 66

Figure 54: Logarithmic plot of the simulated doping concentration as a function of distance from surface for the shallow p-well in deep n-well in p-substrate structure. Dashed red: net doping, green: doping concentration of deep n-well and blue: doping concentration of shallow p-well. 66

Figure 55: Logarithmic plot of the net-doping concentration as a function of distance from surface of the deep p-well in deep n-well in p-substrate structure. The simulated data are compared to the calculated data out of the fit. 67

Figure 56: Logarithmic plot of the net-doping concentration as a function of distance from surface of the shallow p-well in deep n-well in p-substrate. The simulated data are compared to the calculated data out of the fit. 67

Figure 57: Logarithmic plot of the net-doping concentration as a function of distance from surface of the p^+-well in deep n-well in p-substrate structure. The simulated data are compared to the calculated data out of the fit. 68

Figure 58: Logarithmic plot of the net-doping concentration as a function of distance from surface of the n^+-well in p-well in p-substrate structure. The simulated data are compared to the calculated data out of the fit. 68

Figure 59Schematic cross section of the n+ in p-substrate structure 70

Figure 60: Calculated parameters as a function of distance from the surface for the deep n-well in p-substrate structure (see Figure 59); (a) net doping, (b) net doping with doping type, (c) band diagram, (d) space charge, (d) electric field and (e) potential. 70

Figure 61: Schematic cross section of the deep n-well in p-substrate structure 71

Figure 62: Calculated parameters as a function of distance from the surface for the n^+-well in p-substrate structure (see Figure 61); (a) net doping, (b) net doping with doping type, (c) band diagram, (d) space charge, (d) electric field and (e) potential. 71

Figure 63: Schematic cross section of the deep p-well in deep n-well in p-substrate (n-well shorted to p-well) structure. 72

Figure 64: Calculated parameters as a function of distance from the surface for the deep p-well in deep n-well in p-substrate structure (see Figure 63); (a) net doping, (b) net doping with doping type, (c) band diagram, (d) space charge, (d) electric field and (e) potential. 72

Figure 65: Responsivity as a function of wavelength for the shallow n-well in p-substrate structure. The measured responsivity values (purple) and the calculated values (blue) are compared. 74

Figure 66: Responsivity as a function of wavelength of the deep p-well in deep-n-well (p-well shorted to n-well) structure. The measured responsivity values (purple) and the calculated values (blue) are compared. 74

Figure 67: Responsivity as a function of wavelength of the deep p-well in deep n-well in p-substrate (n-well shorted to p-substrate) structure. The measured responsivity values (purple) and the calculated values (blue) are compared. 75

Figure 68: Responsivity as a function of wavelength of the shallow p-well in deep n-well in p-substrate (n-well shorted to p-substrate) structure. The measured responsivity values (purple) and the calculated values (blue) are compared. 75

Figure 69: Exemplary one-junction structures with deep active junction used for the dark current measurements shown in Figure 70: (a) n^+-well in p-substrate structure, (b) deep n-well in p-substrate and (c) n^+-well in p-well structure. 76

Figure 70: Dark current of the n-well in p-substrate structures as a function of voltage @ 25°C. ... 77

Figure 71: Dark current of the n-well in p-substrate structures as a function of voltage @ 60°C. ... 77

Figure 72: Comparison of the dark currenta for the n-well in p-substrate structure as a function of voltage between designs with (dashed line) and without (solid line) field oxide. 78

Figure 73: Comparison of the dark currenta for the shallow n-well in p substrate as a function of voltage between designs with (dashed line) and without (solid line) field oxide. 79

Figure 74: Exemplary structures with deep active junction used for the dark current measurements shown in Figure 40: (a) Shallow p-well in n-well in p-substrate structure, (b) shallow p-well in deep n-well in p-substrate and (c) deep p-well in deep n-well in p-substrate. 80

Figure 75: Dark current for the p-well in n-well structures (p-well shorted to n-well) as a function of voltage @ 60°C. 80

Figure 76: Exemplary structures with shallow active junction used for the dark current measurements shown in Figure 77: (a) Shallow p-well in n-well in p-substrate structure, (b) shallow p-well in deep n-well in p-substrate and (c) deep p-well in deep n-well in p-substrate. 81

Figure 77: Dark current for the p-well in n-well structures (n-well shorted to p-substrate) as a function of voltage @ 60°C. 81

Figure 78: Comparison of dark current for the shallow p-well in n-well in p-substrate structure (p-well shorted to n-well) as a function of voltage between structures with (dashed line) and without (solid line) field oxide. 82

Figure 79: Comparison of dark current for the p-well in deep n-well in p-substrate structure (p-well shorted to n-well) as a function of voltage between structures with (dashed line) and without (solid line) field oxide. 83

Figure 80: Comparison of dark current for the shallow p-well in n-well in p-substrate structure (n-well shorted to p-substrate) as a function of voltage between structures with (dashed line) and without (solid line) field oxide. 83

Figure 81: Comparison of dark current for the p-well in deep n-well in p-substrate structure (n-well shorted to p-substrate) as a function of voltage between structures with (dashed line) and without (solid line) field oxide. 84
Figure 82: Schematic structures compared in Figure 83. (a): deep n-well in p-substrate, (b): shallow p-well in deep n-well in p-substrate and (c): deep p-well in deep n-well in p-substrate 85
Figure 83: Dark current for different deep n-well structures as a function of voltage, showing the effect of different well combinations to dark current. 86
Figure 84: Schematic structures compared in Figure 85. (a): n-well in p-substrate, (b): shallow p-well in n-well in p-substrate and (c): p^+-well in n-well in p-substrate 86
Figure 85: Dark current for different n-well structures as a function of voltage, showing the effect of different well combinations to dark current. 87
Figure 86: Schematic cross section of a PIN photodiode used in the following sections, SCR is the space charge region 88
Figure 87: Schematic explanation for crosstalk, dashed lines indicate the space charge region of the pixels 89
Figure 88: Schematic built up of a guard ring, consisting out of a combination of n- and p-doped regions 90
Figure 89: Top-view of diode array with npn-guard ring 91
Figure 90: Dark current as a function of normalized distance between pixel and guard ring for different photodiode sizes. D1-D11 refer to anodes varying in size and area to perimeter ratio as listed in Table 7 92
Figure 91: β as a function of normalized pixel-to-guard ring distance, parameters calculated for 60 °C, values for 5mV reverse bias 95
Figure 92: β as a function of normalized pixel-to-guard ring distance, parameters calculated for 60 °C, values for 5V reverse bias 96
Figure 93: Dark current as a function of the perimeter of the structures in µm, fixed pixel-to-guard ring distance, T=60°C, reverse bias is 5V 97
Figure 94: Dark current as a function of the perimeter of the structures in µm, fixed pixel-to-guard ring distance, T=40°C, reverse bias is 5V 97
Figure 95: Schematic built up of photodiode with guard ring including the parasitic bipolar transistor 98
Figure 96: Dark current as a function of temperature in °C, comparison of measured data to model data 100
Figure 97: Dark Current as a function of. Voltage, comparison of reverse bias region of different guard ring designs (see Table 11), d/d_{max}=0.4 102
Figure 98: Dark current @ 5V as a function of pixel to guard ring distance for different guard ring designs 103

Figure 99: Crosstalk measurement, photocurrent of photodiode 1 and photodiode 2 as a function of position of the fiber on the chip 104
Figure 100: Crosstalk measurement, photocurrent as a function of position, with area under photodiode 1, from starting point to crossing point (red area) and area under photodiode 2, from starting point to crossing point (blue area) 105
Figure 101: Crosstalk as a function of normalized pixel to guard ring distance of different guard ring structures at a wavelength of 670nm 106
Figure 102: Crosstalk in as a function of normalized pixel to guard ring distance of different guard ring structures at a wavelength of 850nm 106
Figure 103: Top-view of array built up of guard less design 108
Figure 104: Comparison of the dark current as a function of cathode voltage between the three different anodes A1, A2 and A3 109
Figure 105: Comparison of dark current as a function of cathode voltage between single-anode and multi-anode measurement 109
Figure 106: Comparison of dark current as a function of voltage between 1 to 4 diodes measured in parallel 110
Figure 107: Single-anode measurement where the voltage is swept over the cathode, behavior without guard ring 110
Figure 108: Multi-anode measurement where the voltage is swept over the cathode, behavior without guard ring 111
Figure 109: Multi-anode measurement where the voltage is swept over the cathode, behavior with guard ring 111

9 LIST OF TABLES

Table 1: Absorption coefficient in cm^{-1} for the wavelength used in Figure 5 and Figure 7 17
Table 2: Well label explanation ordered by doping type and doping concentration as well as depth of the junction 39
Table 3: Depletion layer width of the p-n junctions for n- in p-structures, V_{bi} is the built in voltage, w_n is the depletion layer width in the n-region, w_p is the depletion layer width in the p-region, and W is the entire depletion layer with 47
Table 4: Depletion layer width of p-n junctions for n- in p-structures, V_{bi} is the built in voltage, w_n is the depletion layer width in the n region, w_p is the depletion layer width in the p region and W is the entire depletion layer with 48
Table 5: Depletion layer width of p-well in n-well structures with V_{Bi} as the the built in voltage, w_n as the depletion layer width in the n region, w_p as the depletion layer width in the p region and W as the entire depletion layer with 58
Table 6: Calculated values of depletion layer width in µm, built in voltage in V and electric field in V/cm for different well structures using Gaussian doping profile 69
Table 7: List of diode structures compared in this chapter with different area to perimeter ratio 92
Table 8: α and β determined form the area-perimeter model as described in (6.2), T=60°C, 5mV reverse bias voltage 94
Table 9: Area related current and perimeter related current calculated for D11 (Table 7), reverse bias voltage is 5mV 94
Table 10: Area related current and perimeter related current calculated for D11 (Table 1), reverse bias voltage is 5V 96
Table 11: List of guard ring teststructures investigated in the following sections. 101

10 BIBLIOGRAPHY

[1] M. Bigas, E. Cabruja, J. Forest and J. Salvi, "Review of CMOS Image Sensors," *Microelectronics Journal,* vol. 37, pp. 433-451, 2006.

[2] C.-Y. Wu, Y.-C. Shih, J.-F. Lan, C.-C. Hsieh, C.-C. Huang and J.-H. Lu, "Design, Optimization, and Performance Analysis of New Photodiode Structures for CMOS Active-Pixel-Sensor (APS) Imager Applications," *IEEE Sensors Journal,* vol. 4, pp. 135-144, 2004.

[3] A. Titus, M. C.-K. Cheung and V. P. Chodavarapu, "CMOS Photodetectors," in *Photodiodes - World Activites in 2011*, InTech, 2011, pp. 65-100.

[4] P. Magnan, "Detection of visible photons in CCD and CMOS: A comparative view," *Nuclear Instruments & Methods in Physics Research,* vol. 504, pp. 199-212, 2003.

[5] T. Coura, L. P. Salles and D. W. de Lima Monteiro, "Quantum-efficiency enhancement of CMOS photodiodes by deliberate violation of design rules," *Elsevier, Sesors and Actuators A: Physical,* vol. 171, pp. 109-117, 2011.

[6] K. Murari, R. Etienne-Cummings, N. Thakor and G. Cauwenberghs, "Which Photodiode to Use: A Comparison of CMOS-Compatible Structures," *IEEE Sensors Journal,* vol. 9, pp. 752-760, 2009.

[7] I. Brouk, Y. Nemirovsky, S. Lachowicz, E. A. Gluszak, S. Hinckley and K. Eshraghian, "Characterization of crosstalk between CMOS photodiodes," *Pergamon, Solid-State Electronics,* vol. 46, pp. 53-59, 2001.

[8] F. Ji, M. Juntunen and I. Hietanen, "Electrical crosstalk in front-illuminated photodiode array with different guard ring designs for medical CT applications," *Elsevier, Nuclear Instruments and Methods in Physics Research A,* vol. 607, pp. 150-153, 2009.

[9] S. M. Sze, Physics of Semiconductor Devices, John Wiley & Sons, 1981.

[10] B. V. Zeghbroeck, "Principles of Semiconductor Devices," 2011. [Online]. Available: http://ecee.colorado.edu/~bart/book/book/contents.htm.

[11] F. Thuselt, Physik der Halbleiterbauelemente, Berlin Heidelberg: Springer, 2005.

[12] J. Singh, Semiconductor Devices, Basic Principles, John Wiley, 2001.

[13] S. Wolf, Microchip Manufacturing, Lattice Press, 1943.

[14] D. A. Neamen, Semiconductor Physics and Devices - Basic Principles, New Mexico: McGraw-Hill, 2003.

[15] H. Zimmermann, Silicon Optoelectronic Integrated Circuits, Springer-Verlag, 2004.

[16] G. Q. Zhang and A. J. Roosmalen, More than Moore, Einhoven: Springer, 2009.

[17] "Wikipedia - The free Encyclopedia," Wikipedia Foundation, [Online]. Available: http://en.wikipedia.org/wiki/Half_power_point. [Accessed 11 December 2012].

[18] M. M. Blouke and E. Bodegom, "Diffusion dark current in CCDs and CMOS image sensors," *Sensors, Cameras, and Systems for Industrial/Scientific Applications,* 2008.

[19] A. Hoffman, M. Loose and V. Suntharalingam, "CMOS Detector Technology," in *Scientific Detectors for Astronomy*, Springer, 2006, pp. 377-402.

[20] A. J. Theuwissen, "CMOS image sensors: State-of-the-art," *elsevier, Solid-State Electronics,* vol. 52, pp. 1401-1406, 2008.

[21] V. Goiffon, C. Virmontios, P. Magnan, P. Cervantes, S. Place, M. Gaillardin, S. Girard, P. Paillet, M. Estribeau and P. Martin-Gonthier, "Identification of Radiation Induced Dark Current Sources in Pinned Photodiode CMOS Image Sensors," *IEEE Transactions on Nuclear Science,* pp. 918-926, 4 August 2012.

[22] A. E. D. GmbH, "A3PiCs Tunable Light Source - TLS2, Product Reference Manual," 2011.

[23] B. Ciftcioglu, L. Zhang, J. Zhang , J. R. Marciante, J. Zuegel, R. Sobolewski and H. Wu, "Integrated Silicon PIN Photodiodes Using Deep N-Well in a Standard 0.18-µm CMOS Technology," *Journal of Lightwave Technology,* vol. 27, pp. 3303-3313, 2009.

[24] A. Darmont, "Spectral Response of Silicon Image Sensors," Aphesa, 2009.

[25] J.-M. Park, "personal communication," 2012.

[26] R. Minixhofer, "Integrating Technology Simulation into the Semiconductor Manufacturing Environment," Phd Thesis, 2006.

[27] R. Minixhofer, "personal communication," 2012.

[28] N. V. Loukianova, H. O. Folkerts, J. P. Maas, D. W. Verbugt, A. J. Mierop, W.

Hoekstra and E. Roks, "Leakage Current Modeling of Test Structures for Characterization of Dark Current in CMOS Image Sensors," *IEEE Transactions on Electron Devices,* vol. 50, no. 1, pp. 77-83, 2003.

[29] F. Lau, L. Mader, C. Mazure, C. Werner and M. Orlowski, "A Model for Phosphorus Segregation at Silicon-Silicon Dioxide Interface," *Applied Physics A, Solids and Surfaces,* vol. 49, pp. 671-675, 1989.

[30] L. Pei, "Dopant Segregation at Silicon-Oxide Interfaces," Phd Thesis, 2006.

[31] J. Teva, I. Jonak-Auer, F. Schrank, J. Kraft, J. Siegert and E. Wachmann, "Gathering effect on Dark Current for CMOS fully integrated-, PIN-photodiodes," in *SPIE7605, Optoelectronic Integrated Circuits XII*, San Francisco, 2010.

[32] C.-C. Wang, "Phd Thesis: A study of CMOS TEchnologies for Image Sensor Applications," Massachusetts Institute of Technology, Massachussets, 2001.

[33] J. Teva, "personal communication," 2012.

[34] J. Teva, S. Jessenig, I. Jonak-Auer, F. Schrank and E. Wachmann, "Dark current study for CMOS fully integrated-PIN-photodiodes," in *Proc. SPIE 8073*, Prague, 2011.

[35] EMVA Standard 1288, "Standard for Characterization of Image Sensors and Cameras," EMVA Standard Compliant, 2010.

[36] F. Ji, M. Juntunen and I. Hietanen, "Evaluation of electrical crosstalk in high-density photodiode arrays for X-ray imaging applications," *Elsevier, Nuclear Instruments and Methods in Physics Research A,* vol. 610, pp. 28-30, 2009.

[37] M. J. I. H. Fan Ji, "Evaluation of electrical crosstalk in high-density photodiode arrays for x-ray imaging applications," *Nuclear Instruments and Methods in Physics research,* 2009.

[38] K. A. Kuhn, "University of Alabama at Birmingham," 3 September 2009. [Online]. Available: http://www.kennethkuhn.com/students/ee351/diode_characteristics.pdf. [Accessed 15 July 2012].

[39] N. Kavasoglu, S. A. Kavasoglu and S. Oktik, "A new method of diode ideality factor extraction from dark I-V curve," *Elsevier, Current Applied Physics,* vol. p, pp. 833-838, 2009.

[40] E. Kasper and D. J. Paul, "Optoelectronics," in *Silicon Quantum Integrated Circuits*, Spinger, 2006, pp. 281-309.

[41] C. Honsberg and S. Bowden, "Photovoltaic Eductation Network," [Online]. Available: http://www.pveducation.org/. [Accessed 6 October 2012].

[42] E. R. Fossum, "CMOS Image Sensors: Electronic Camera-On-A-Chip," *IEEE Transactions on Electron Devices,* vol. 44, 1997.

[43] S. Banerjee and W. A. Anderson, "Temperature dependence of shunt resistance in photovoltaic devices," *Applied Physics Letters,* vol. 49, pp. 38-40, 1986.